SYNCHROTRON RADIATION-BASED SPECTROSCOPIC INVESTIGATION OF THE ELECTRONIC AND GEOMETRIC STRUCTURES OF IRON-SULFUR CLUSTERS, PARTICLES, AND MINERALS

by

David Jeremiah Gardenghi

A dissertation submitted in partial fulfillment
of the requirements for the degree

of

Doctor of Philosophy

in

Chemistry

MONTANA STATE UNIVERSITY
Bozeman, Montana

April 2012

APPROVAL

of a dissertation submitted by

David Jeremiah Gardenghi

This dissertation has been read by each member of the dissertation committee and has been found to be satisfactory regarding content, English usage, format, citation, bibliographic style, and consistency and is ready for submission to The Graduate School.

Dr. Robert K. Szilagyi

Approved for the Department of Chemistry and Biochemistry

Dr. Bern Kohler

Approved for The Graduate School

Dr. Carl A. Fox

STATEMENT OF PERMISSION TO USE

In presenting this dissertation in partial fulfillment of the requirements for a doctoral degree at Montana State University, I agree that the Library shall make it available to borrowers under rules of the Library. I further agree that copying of this dissertation is allowable only for scholarly purposes, consistent with "fair use" as prescribed in the U.S. Copyright Law. Requests for extensive copying or reproduction of this dissertation should be referred to ProQuest Information and Learning, 300 North Zeeb Road, Ann Arbor, Michigan 48106, to whom I have granted "the exclusive right to reproduce and distribute my dissertation in and from microform along with the non-exclusive right to reproduce and distribute my abstract in any format in whole or in part."

David Jeremiah Gardenghi

April 2012

ACKNOWLEDGEMENTS

I would like to express my sincere thanks to my advisor, Professor Robert Szilagyi, for his guidance and continual support throughout my graduate studies. I came to Montana State University with the desire to learn computational chemistry with experimental support, and I found the experimental work so intriguing that I focused my dissertation on the experimental technique. I have immensely enjoyed learning about X-ray absorption spectroscopy and thank Robert for revealing to me the world of synchrotron-based spectroscopy.

I want to acknowledge my collaborators for their contribution to this work, Professor Trevor Douglas for providing the nanoparticles encapsulated in protein cages, Dr. David Mulder and Professor John Peters for providing the opportunity to work with them on [FeFe]-hydrogenase, Dr. Sunshine Silver and Professor Joan Broderick for providing the opportunity to study Spore Photoproduct lyase with them, Dr. Li Che and Professor Timothy Minton for providing the modified pyrite from their beam scattering experiments and the insights to the mechanism.

I would also like to thank the members of our research group for creating a fun and positive research environment. I especially would like to thank Logan Giles and Dr. Travis Harris for the many insightful conversations and advice while doing my research. Finally, I would like to thank my parents, Al and Angie Gardenghi, for their loving and continual support, my wife, Emi, for her never-ending encouragement and confidence in me to complete this degree, and God for His grace and faithfulness, without which I would not be here today.

TABLE OF CONTENTS

TABLE OF CONTENTS - CONTINUED

LIST OF TABLES

Table Page

LIST OF FIGURES

LIST OF TABLES – CONTINUED

Figure Page

LIST OF TABLES – CONTINUED

Figure Page

LIST OF TABLES – CONTINUED

Figure Page

LIST OF TABLES – CONTINUED

Figure Page

LIST OF TABLES – CONTINUED

Figure Page

ABSTRACT

Iron-sulfur systems are ubiquitous in biological and geological environments. They range from molecular scale [2Fe-2S] clusters to nanometer scale particles to micrometer scale minerals. Across the length scale, each system has unique structural and functional roles with respect to its environment, such as metalloproteins or hydrothermal vents. Therefore, it is of great interest to understand the electronic and geometric structural properties that give a wide range of reactivity. The main focus of this dissertation is to investigate the possible connections among the different size scales using a primary technique, X-ray absorption spectroscopy (XAS), by gaining an understanding into the relationship between the system size and properties. X-ray absorption spectroscopy is a powerful tool to probe geometric and electronic structures across the entire length scale. In this work, extend x-ray absorption fine structure (EXAFS) analysis method was applied to determine geometric structure of the protein bound, molecular iron-sulfur cluster of HydA. It was found to contain a preformed [4Fe-4S] cluster. This method combined with Fe/S K-edge XANES analysis was applied to spore photoproduct lyase metalloprotein to structurally characterize the [4Fe-4S] cluster and its interaction with SAM. The Fe K-edge EXAFS and Fe/S K-edge XANES provide evidence for a cluster distortion upon interacting with SAM as a new EXAFS feature, indicating the presence of longer Fe-Fe distances and this provides new insights into the structure of radical SAM enzymes. At the nanometer scale, mineral and protein encapsulated particles were investigated with a possible link between molecular and micrometer scale. A reference library of FeS systems was established to describe the variation in bonding and structure. Also, a considerable amount was learned about XAS detection methods, and this was applied to the micrometer scale systems. From EXAFS and XANES analysis, the modified surface of pyrite was revealed to have an intermediate layer of Fe(I)-S phase with a metallic iron surface, and a reaction scheme was proposed. These studies of the different size iron-sulfur systems provide insights into the change in the electronic and geometric structures, and a model was proposed to describe the effects of size on the electronic and geometric structure.

CHAPTER 1

INTRODUCTION

Iron Sulfur Systems

Iron-sulfur systems are found throughout the earth. These systems are important in environmental, geological, material, and biological sciences. In geology, pyrite (FeS_2) exhibits a profound effect on its environment[1-4]. Also, pyrite has been investigated as a relevant mineral surface for the activation of small molecules.[5] In environmental science, iron sulfur precipitates play an important role in sequestration and remobilization of heavy metal contaminates.[6, 7] In material science, the nanometer scale iron sulfides particles from structurally controlled synthesis is proposed to have potential as biological sensors, drug carriers and diagnostic agents.[8] In metalloenzymology, molecular iron-sulfur clusters[9] are ubiquitous.[10, 11] A wide-variety of metalloproteins and metalloenzymes contain iron-sulfur clusters. These are involved in a variety of biological processes, such as electron transfer,[12-14] small molecule activation,[15-18] atom abstraction,[19] DNA repair,[20] and signal transduction.[21]

An insightful way to investigate the chemical interactions within iron-sulfur systems is to consider how the size of iron-sulfur systems that cross more than 6 orders of magnitude (micro – nano – molecular) affect their electronic and geometric structures. This information is particularly relevant in electron-transfer and small molecule activation reactions. There has been much research in individual electronic and geometric

structures, but little is known about how the electronic and geometric structures of the iron-sulfur systems vary across length scales.

Molecular Scale

The molecular scale is the classical area of study with X-rays due to the comparable wavelength to the size of the system. The smallest iron-sulfur systems are molecular iron-sulfur clusters, which are found wide-spread in biology. These clusters vary in size from minimal [2Fe-2S] clusters such as those in ferredoxins[22] to the [Mo-7Fe-8S] cluster in nitrogenase,[23] with functionality varying as widely, as electron transfer, small molecule activation, catalysis, and sensing of iron and oxygen.[10] The variation in functionality can be associated with change in electronic and geometric structure due to size of cluster and its coordination environment. For example, in aconitase the site-differentiated cluster coordinated with only three cysteine ligands undergoes interconversion between the inactive $[3Fe\text{-}4S]^{1+}$ state and the active $[4Fe\text{-}4S]^{2+}$ catalytic state,[24] and other site-differentiated clusters as in SAM radical enzymes have a wide range of specific catalytic functions including DNA repair, sulfur insertion reactions, rearrangement reactions, and biosynthesis of complex cofactors and metal clusters.[25] Some cluster environments do not have standard cysteine-only coordination environment as in hydrogenase[26] and nitrogenase;[23] thus, due the varied ligand environment these clusters show catalytic activity instead of just electron transfer.

As an example of unique iron-sulfur metalloenzymes, [FeFe]-hydrogenase contains an unusual iron-sulfur cluster active site, termed the H-cluster, and is able to efficiently catalyze the reversible oxidation of molecular hydrogen ($\sim 10^4$ H_2 molecules

per second per molecule of enzyme).[27] The H-cluster exists as a 6Fe composed of a biologically unprecedented 2Fe-subcluster connected to [4Fe-4S] cluster via a single bridging cysteine. The 2Fe-subcluster consists of a five-member dithiolate ligand and cyanide and carbon monoxide ligands. The synthesis of the H-cluster requires the maturation enzymes, HydE, HydF, and HydG. The structural analysis of apo-hydrogenase expressed in the absence of the maturation enzymes indicated the presence of a pre-formed [4Fe-4S] cluster (see Chapter 2). Thus, the maturation enzymes are required for the assembly of the unique 2Fe-subcluster. It has been shown through the characterization of HydF with and without HydE and HydG that the 2Fe-subcluster is formed on HydF, and thus the radical SAM enzymes, HydE and HydG, are involved in the synthesis of the ligands. HydG functions in the synthesis of carbon monoxide and cyanide ligands through the catalyzed cleavage of tyrosine. Thus, HydE is believed to be involved in the synthesis of the dithiolate ligand, although, the substrate of HydE has not yet been identified.[28, 29]

In an effort to study the structure and properties of the protein bound iron-sulfur cluster active sites under controlled conditions, research turned to synthetic analogues of the iron-sulfur clusters. As a result of emerging crystallography data in the early 70's of metalloproteins containing iron-sulfur sites, a remarkably large number of biomimetic iron-sulfur clusters have been synthesized (see Figure 1.1). The various compositions of synthetic analogues of each type of active sites from rubredoxin to P-cluster allow for the investigation of the chemical properties of the active sites, such as reduction potential and electronic structure, in the absence of the protein environment.[4,6]

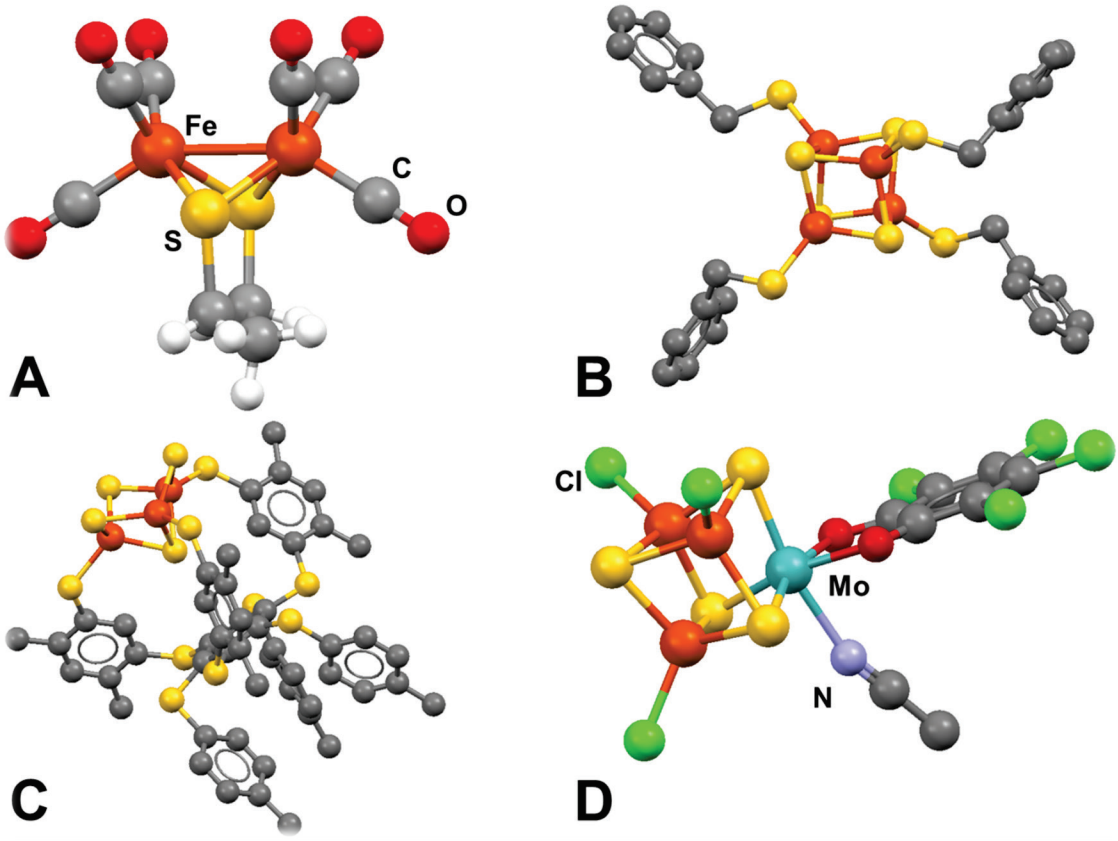

Figure 1.1. Examples for synthetic analogue of the (A) [2Fe] subcluster[30] of [FeFe]-hydrogenase, (B) [4Fe-4S] cluster[31] of the active site in *P. aercyenes*, (C) [3Fe-4S] cluster[32] in aconitase, and (D) [Mo-3Fe-4S] cluster[33] of the Mo subcubane of nitrogenase

Much research has gone into investigating the electronic properties of protein bound iron sulfur clusters and how the protein environment affects the cluster.[9, 34-36] One extensively studied area is the reduction potentials of protein bound [4Fe-4S] clusters *versus* their synthetic analogues.[9] Due to protein environment and structural effects that control the potentials, the coupled states $[4Fe\text{-}4S]^{3+/2+}$ and $[4Fe\text{-}4S]^{2+/+}$ do not traverse all three oxidation states in native protein conformations. In synthetic analogues, these steps are almost always reversible except in the terminal reduction and oxidation steps.[9, 37] A range of reduction potentials has been achieved through different thiolate (SR)

substitution where the R is varied (i.e. R = Me, Et, tBu, Ph etc.). Although tunable, the synthetic analogues still have a lower potential, such as $[Fe_4S_4(SPh)_4]^{2-}$ at −1.04 V, than the similar protein equivalents around −0.4 V.[9] Even among biological iron sulfur clusters with the same cluster composition, the reduction potential varies, such as with ferredoxins, about −400 to −200 mV.[38] Since the overall geometry is about the same for biomimetic and protein-bound clusters, this difference in reduction potential originates mainly from the solvent and protein environment, respectively. The solvent environment can be consider as isotropic and depends on the dielectric constant of the medium (ε = ~30–40). The protein environment generally has a lower dielectric constant (ε = ~10). Thus due to anisotropic nature of the protein environment, various factors affect iron-sulfur clusters including hydrogen-bonds,[39, 40] charged and polar residues,[36, 41-43] solvent accessibility,[40] and ligand conformation.[44] Clearly, the environment surrounding the iron sulfur cluster, which varies among proteins, has an important influence on its properties. Despite all these efforts, the electronic structure of protein bound iron-sulfur has not yet been fully understood beyond a few well-defined cases.[45]

Nanometer Scale

Nanometer scale iron-sulfur systems have become a focus of growing scientific interest due to their importance in hydrothermal vents,[46] pollution,[47] cancer treatments,[48] and catalytic applications.[49, 50] A simple, controlled synthesis of nanometer scale iron-sulfur systems has proven to be challenging. Thus, the structural and electronic properties of the nanometer scale iron-sulfur systems remain somewhat ill-defined. A variety of approaches have been employed to synthesize nanometer scale iron-sulfur particles such

as bacteria-assisted production,[51] carbon dioxide laser pyrolysis of iron complexes,[52] and polymer or dendrimer stabilized wet-chemical synthesis.[53] Another novel approach is the formation of iron sulfur particles within protein cage architectures including ferritin and ferritin-like proteins. The protein shell helps prevent aggregation of nanometer scale particles and can be modified to engineer the formation of application-oriented materials.[8]

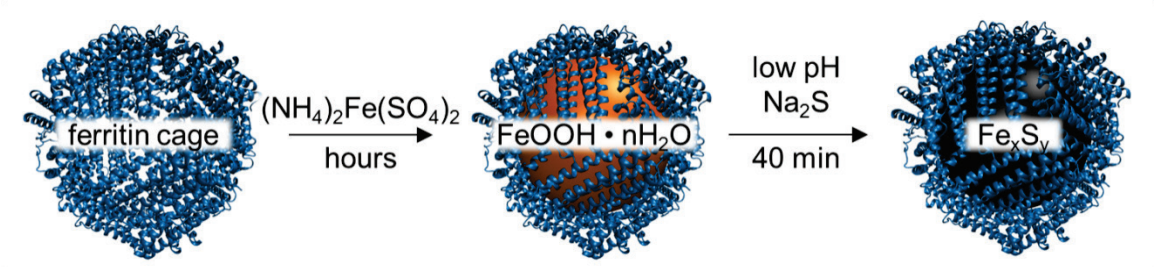

Figure 1.2. The formation of a complete iron sulfur core in ferritin through conversion of ferrihydrite core[8]

Research in this area can be considered to be in the early stages, but the Douglas group at Montana State University has already made considerable progress. They employ protein cages and viral capsids, as biomolecular architectures to control the synthesis of inorganic nanometer scale particles. The relevant work[8, 54-56] is focused on the use of iron storage protein ferritin and small heat shock proteins as the architectural cages. These cages come in a range of inner diameters that allow for control of the size of nanoparticles.[57] They have developed a protocol for loading the cages with iron sulfide through dissolution and precipitation reactions of the native mineral ferrihydrite inside the protein cage (Figure 1.2). Various parameters control iron-sulfide formation, such as temperature, pH, cage size, and Fe(II) loading ratio. It has already been shown that the

conversion of iron oxide to iron sulfide is controlled by pH and temperature.[8] This study also showed that these iron-sulfur cores contain mostly Fe centers in the +III oxidation state, which is unusual for minerals except with Fe centers in a mixed-oxidation states, such as greigite.[58]

Another relevant area of research is the modification of the protein cages,[56, 59-61] such as ferritin to mimic the protein environment of iron-sulfur cluster-containing metalloenzymes. As shown from studying synthetic analogues of iron-sulfur clusters,[9] the protein environment plays an important role in both structure and chemical properties of the iron-sulfur cluster. By using iron-sulfur cluster-containing active sites of metalloenzymes as templates, the mutation of the cage's inner surface compositions at the protein-mineral interface could provide insights into mineralization and structure, as well as the nanoparticle's catalytic properties. Functionalized nanometer scale particles have the potential to mimic the reactivity of protein bound iron-sulfur clusters with a good synthetic control of structure and function relative to mineral surfaces or protein bound clusters.

Micrometer Scale

At the micrometer scale and above, the relevant iron-sulfur systems are defined by mineral surfaces. Iron-sulfur minerals have been studied extensively, but most of the research focused on formation of minerals with limited focus on chemical reactivity. In the past ten years, there has been an increased interest in investigation of the reactivity of pyrite surface with small molecules. Not only is pyrite the most common sulfide in the Earth's surface, but the well-defined iron sulfide contains a reduced iron (Fe^{2+}) and

oxidized ligand (S_2^{2-}), thus a potential redox system. Even with considerable recent literature on this subject, the mechanisms and reactivity are still not understood. Most investigations have focused on understanding the surface of pyrite and related iron-sulfur minerals to define the reaction sites. The focus of reactivity has been on small molecules such as O_2, H_2O, H_2S, CH_4, CO/CO_2, and N_2.[62]

The oxidation of the pyrite surface has been studied extensively from many perspectives.[62] An important result from reactivity studies on pristine surfaces is that defect sites with Fe(III) play important roles in the electronic properties and reactivity of the surface. It is proposed that Fe(II) is oxidized by intramolecular electron-transfer due to the homolytic cleaving of surface persulfide bonds during preparation of the surface. Thus, the persulfide, S_2^{2-}, is cleaved to form S^{1-}, which relaxes by an intramolecular electron transfer to S^{2-}, hence oxidizing iron in the following redox reaction:

$$Fe^{2+}_{surface} - S^{2-}_{2\,surface} \rightarrow Fe^{2+}_{surface} - S^{1-}_{2\,surface} \rightarrow Fe^{3+}_{surface} - S^{2-}_{2\,surface} \quad (1.1)$$

In recent studies,[63-65] it has been shown that monosulfides exist on the surface, although their chemical environment has yet to be fully characterized. One interesting observation is that the concentration of monosulfides was decreased when the pyrite surface was annealed in an atmosphere of 10^{-7} Torr S_2(g) at 570 K.[63] The reduction of defect sites is presumably due to the conversion of monosulfide to disulfide by the exposure to S_2(g). In another study,[64] H_2S was shown to be adsorbed to a pyrite surface at low temperatures and desorbed at room temperature. However at elevated temperatures (500 K), the H_2S dissociated into surface bound H_2, S, and SH. These experiments suggested that S-fragments reacted with monosulfide sites to form sites resembling FeS_2.

Given the high temperature requirements of these reactions, the results described in Chapters 5 and 6 are quite remarkable.

In the entire range of iron-sulfur systems, the prevalent theme is their ability to accept, donate, polarize, and store electrons. There seems to be an inverse relationship between size and reactivity. The molecular scale iron-sulfur systems have the most versatile and extensive reactivity of all the iron-sulfur systems while the micrometer scale minerals must be subjected to a non-ambient condition in order to observe reactivity. This is not unexpected since minerals tend to be inert, and molecular clusters tend to be reactive. Here is where nanometer scale particles fill the gap in understanding the why and how of the differences in scale matters. As the size of the systems increase, the surface to volume ratio decreases, and the surface becomes more ordered. This change corresponds to more stability and could potentially be correlated with decrease in activity.

X-ray Absorption Spectroscopy

X-ray absorption spectroscopy (XAS) measures the absorption of Ångstrøm wavelength electromagnetic radiation as a function of energy. XAS spectra can be divided into two distinct regions: the edge or sharp rise in absorption or intensity, which is known as XANES (X-ray Absorption Near Edge Structure), and the oscillations following the edge, which are known as EXAFS (Extend X-ray Absorption Fine Structure). X-rays are capable of providing atomic scale information about both the geometric and electronic structures. Obtaining geometric information is well developed

for X-ray crystallography, where the ordered lattice gives diffraction patterns, and from scattering theory the exact positions of atoms can be determined. In the given series of studies, X-rays are applied to disordered, non-crystalline systems, for which the EXAFS analysis is employed to obtain geometric information. Furthermore, the development of tunable, high flux synchrotron radiation sources have made possible the multi-edge XAS or XANES approach to obtain a wealth of complementary electronic information.

X-rays are produced through the change in acceleration of a charged beam of particles, such as electrons. Synchrotron radiation is produced through the bending of the beam of close to relativistic electrons by magnetic fields. Due to the bending, the acceleration is perpendicular to the direction of travel, and thus, produces a collimated and plane-polarized high intensity beam of synchrotron radiation. In comparison to a uniform bending, wigglers and undulators allow higher brightness over the light produced. They accomplish it with periodic magnetic fields with no overall deflection of the beam, but the undulator generates artifactual oscillations in the beam intensity, which may interfere with EXAFS data analysis. Another important feature of synchrotron radiation is the tunability over a wide energy range of electromagnetic radiation that is achieved through double crystal or grading monochromators. The beam is conditioned using slits and focused with mirrors before and after the monochromator.[66, 67] Due to these qualities of synchrotron radiation, high resolution spectra over wide energy ranges have stimulated considerable research in fields of biology, chemistry, material science, and many other scientific fields.

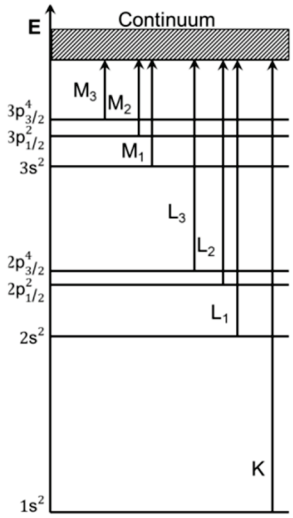

Figure 1.3 Schematic of X-ray absorption transitions (arrows represent the binding energy for variable transitions)

XANES

Since the edge transitions are a result of core hole excitations, absorptions below and at the absorption edge provide information about the electronic and atomic structures, respectively. The different absorption edges as result of different transitions (see Figure 1.3) provide different types of electronic structure information. The spectral features below the metal K-edge are due to the 1s $\rightarrow$ (n+1)p electric dipole allowed (Δl = ±1) transition with the pre-edge features due to 1s $\rightarrow$ nd transitions. With these features being only quadrupole allowed (Δl = ±2), any intense pre-edge features are due to metal (n+1)p mixing with the (nd) orbitals. This is only observed when center of symmetry is absent for the absorber. Thus, the pre-edge provides information about mixing of the p and d orbitals and furthermore about the geometry (i.e. octahedral and tetrahedral). Since the K-edge is a transition from the 1s orbital, the energy position of the edge is sensitive to the

absorber's effective nuclear charge (Z_{eff}), thus the absorber oxidation state can be seen as a shift in edge position.

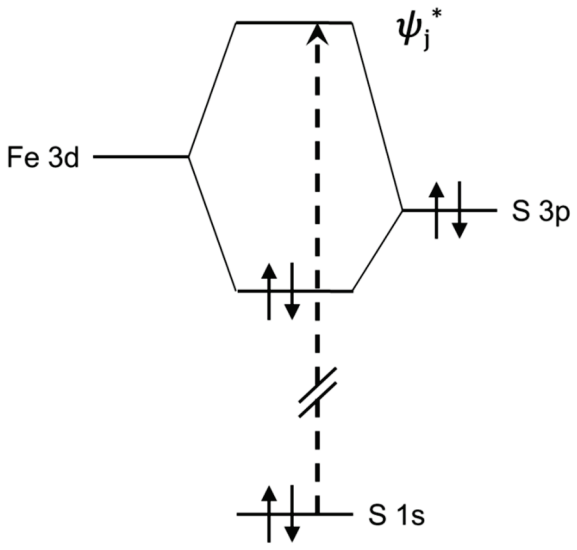

Figure 1.4. Simplified molecular orbital diagram for the excitation of S 1s to the Fe 3d-based molecular orbital that is mixed with S 3p making it electric dipole allowed

The spectral features of the ligand K-edge along the rising-edge are due to the 1s $\rightarrow$ (n+1)p, and the pre-edge intensity is due to the 1s $\rightarrow$ np electric dipole allowed transition. As with the metal K-edge, the edge energy position is directly related to the Z_{eff} of the absorber atom. Furthermore, the pre-edge transition can be related to an excitation of the core 1s electron into an unoccupied antibonding molecular orbital. In transition metals complexes, the ligand np orbital mixes with the metal unoccupied or partially occupied nd orbitals and thus, this transition directly probes the ligand-metal bond in the antibonding (ψ^*) orbital. Furthermore, using Fermi's Golden rule and the dipole approximation to describe the absorption, the area under a given feature for a transition is directly proportional to the probability of transition, given by

$$D \propto \left| \langle \psi_f | r | \psi_i \rangle \right|^2 \tag{1.2}$$

where D is the total area under the peak, ψ_f is the many electron final state associated with the single electron occupied metal-ligand antibonding orbital in the presence of a core hole, and ψ_i is the initial state associated with the ground electronic structure. Due to the 1s orbital being localized on the ligand, the many electron initial state is approximated to be the 1s orbital, and thus, the probability of transition is directly related to the amount of ligand *n*p character. Therefore, the intensity directly quantifies the amount of ligand *n*p character in the valance molecular *n*d orbitals. The total ligand character (α^2) can then be determined by the following equation:[68]

$$D = \frac{1}{3}\alpha^2 \langle r \rangle \tag{1.3}$$

where $\langle r \rangle$ is the dipole integral and D is the total area under the peak. The individual orbital coefficients (α_i^2) can be determined using the following equation:

$$D_0 = \frac{1}{3}\frac{h}{N}\sum_i \alpha_i^2 \langle r \rangle \tag{1.4}$$

where D_0 is the area under the peak normalized per electron hole with N absorbers and h holes. Thus, ligand K-edge X-ray absorption spectroscopy can be used to determine ligand character of the metal-ligand bond. Because of this mixing with the metal acceptor orbitals, the pre-edge energy position is also related to the effective nuclear charge (Z_{eff}) of the metal due to the change in overlap of the metal with the ligand orbitals as a function of metal orbital energy, which in turn is affected by the metal Z_{eff}. In addition, the overall shift in the edge position also affects the pre-edge energy position; therefore

both need to be taken into account when comparing XAS spectra of various compounds.[69]

The L-edge features are separated into three edges. Due to spin-orbit coupling, excitations of the 2p shell electrons split into two edges, L_{II} & L_{III}, where the total electron angular momentum (including both orbital and spin contributions) are J=1/2 and 3/2, respectively. The L_I-edge is from the 2s $\rightarrow$ (*n*+1)p transition, yet the absorption cross section of this transition is small, and thus the corresponding edge features are usually weak for Z<40.[70] For *n*d transition metals, the L_{II}- and L_{III}-edges are a result of the 2p $\rightarrow$ *n*d electric dipole allowed transition. While the normalized ligand K-edge spectra have white line intensity around 1.8-2.5 absorption units, the L-edge spectral features can be about 3-4 times more intense due to the use of electron yield vs. fluorescence emission detection, respectively. As in the ligand K-edge, the L_{II}- and L_{II}-edges directly probe the metal *n*d character in the ligand-metal bond. Thus, the corresponding change intensity of the L_{II}- and L_{II}-edge will be reflected in the ligand K-edge. Furthermore, it also contains information about the ligand field splitting, such as the loss of degeneracy of e_g and t_{2g} of octahedral complexes but is convoluted by multiplet contributions similar to those described by Tanabe-Sugano diagrams.[71-74] Thus, through complementary analysis of the different absorption edges, a total electronic structure of a system can be determined.

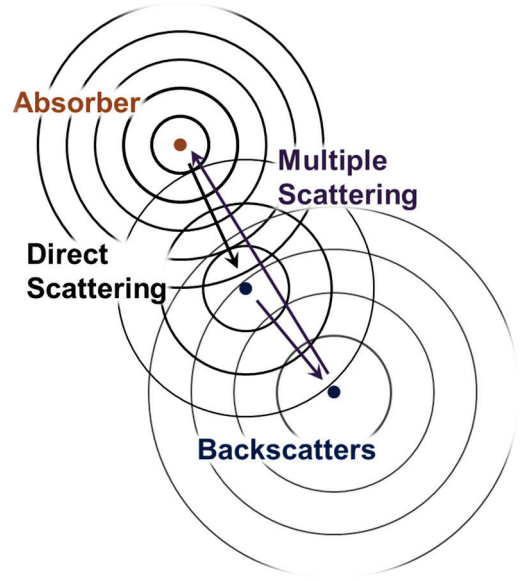

Figure 1.5. Schematic of EXAFS and the scattering paths

EXAFS

The EXAFS is interpreted as a quantum-interference phenomenon (Figure 1.5). Similarly to a rock dropped into a pond, spherical waves propagate outwards until hitting obstacles that in turn backscatter the waves towards the origin and interact destructively or constructively with the outgoing wave. The phenomenon occurring in atoms involves photoelectron waves that are backscattered by the electron density of neighboring atoms. Furthermore, the probability of X-ray photons being absorbed by an electron is dependent upon the initial and final states of the electron. The initial state corresponds to the absorption edge and the final state to the outgoing photoelectron wave. The final state is the sum of the photoionized electron and its backscattered waves. This gives rise to constructive and destructive interferences as a function of wavelength or energy. The results of these processes are the oscillations seen in the XAS spectrum above the edge jump. There are a number of important factors that affect this interference. The number

and types of neighboring atoms affect the amplitude of the backscattered wave. The finite lifetime of the photoelectron causes the wave to decay, and thus limits the range of EXAFS to at most 10 Å. The phase shift of the absorbing atom is important, since the photoelectron sees the potential of absorber atom twice and usually accounts for a few tenths of an Ångstrøm that can be corrected with a theoretical or experimental reference. The Debye-Waller factor accounts for the thermal vibrations and disorder in the atomic positions of absorbers and backscatterers. As temperature increases, the EXAFS tends to get washed out. From this quantum interference, interatomic distances can be determined accurately within 0.02-0.04 Å due to frequency not being affected by experimental noise. However, the resolution ($\Delta R = \pi/2\Delta k$) between different neighboring atoms of similar distances is dependent upon the range of the data in electron momentum space analyzed (Δk). Thus, for typical range of Δk = 12 Å^{-1}, similar distances can be separated only if they differ by more than ~0.1 Å.[66, 67, 75]

In data analysis of EXAFS, the XAS spectrum is first reduced to a χ function. The χ in energy space is defined by the following equation:

$$\chi(E) = \frac{\mu(E) - \mu_0(E)}{\mu_0(E)} \tag{1.5}$$

where μ is the measured absorption coefficient, μ_0 is the absorption coefficient in the central atom in the absence of the neighboring atoms. The latter cannot be measured experimentally and is estimated through fitting a smooth background, μ_b, to the post-edge. Thus, equation (1.5) becomes

$$\chi(E) = \frac{\mu(E) - \mu_b(E)}{\Delta\mu(E)} \tag{1.6}$$

where Δμ is an estimated value of the height of the edge step. Once the background has been subtracted the data is converted to momentum space.

$$k = \sqrt{\frac{2m}{\hbar^2}(E - E_0)} \tag{1.7}$$

where m is the mass of an electron and $\hbar$ is Planck's constant. The $\chi(k)$ spectrum or EXAFS consists of the sum of discrete, damped sine waves, where the frequency and amplitude correspond to the path length and atomic number of backscatterers. To give the EXAFS data a constant amplitude and amplify the high k range oscillations, the $\chi(k)$ data is weighted usually by k^3 due to the damping or decay of the oscillation is roughly $1/k^2$ at higher k and an additional $1/k$ factor from the EXAFS equation (see below). To help separate out the different scattering paths, the Fourier transform (FT) of the EXAFS signal is taken.

The FT is a mathematical operation, when applied to EXAFS it converts the momentum domain to frequency domain. Therefore, the FT of the EXAFS signal is the representation of the periodicity giving rise to the oscillations. Since the oscillations are primarily the result of the scattering path length between the absorber and backscatterer, the FT contains the information for the radial distribution of the backscatterers. Thus, the signal that is periodic in momentum space will have a single value in distance space. The FT of a δ function (localized) momentum space is an infinite sine wave (delocalized) in distance space (see Figure 1.6A). The FT of a step function in k-spaced is a damped sine wave in distance space (Figure 1.6B).

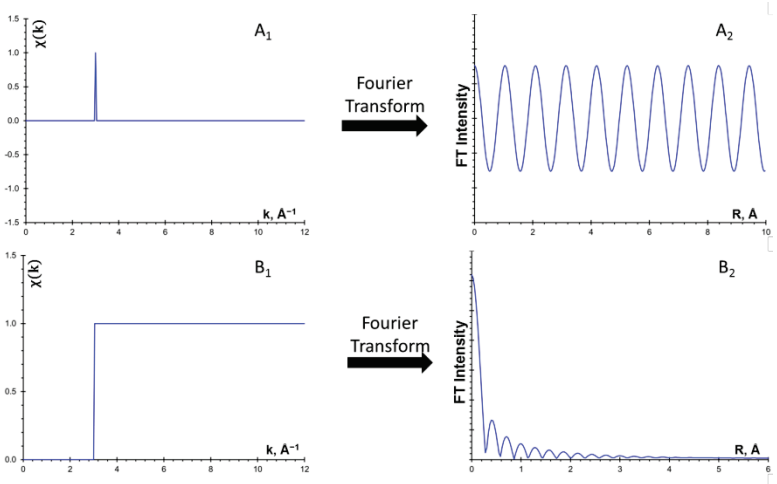

Figure 1.6. Examples of the Fourier transform of a delta function (A_1) in k-space to R-space (A_2) and a step function (B_1) in k-space to R-space (B_2)

Since $\chi(k)$ data is the sum of discrete sine waves, the FT of a discrete or truncated sine wave results in distorted peak instead of a well-defined delta function. This distortion is seen in the regularly spaced ripples or side lobes near the peak (Figure 1.7). The ripples are a result of the truncating or windowing of the infinite sine wave. These artifacts of the FT can be reduced by multiplying the weighted $\chi(k)$ signal with a FT windowing function. Depending upon the slope of the window edges, the ripples can be reduced although at the expense of broadening the peaks (Figure 1.7). Thus, the artifacts of the windowing should not be fitted during the analysis of the EXAFS. Also, the size of the FT windowing is important. If it is too small, the peaks will distort and possibly lose information about scatterers. Another important property of the FT is that it is composed real and imaginary parts along with their magnitude. The magnitude of the FT is not unique because different real and imaginary parts could have the same magnitude; thus information is being ignored when examining the magnitude of FT. These different

factors are important to be considered when looking at the Fourier transform of the EXAFS data.

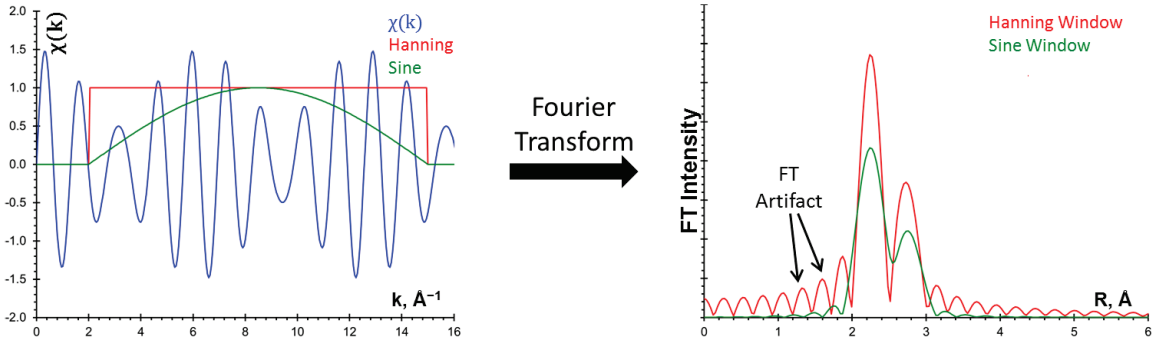

Figure 1.7. Examples of the Fourier transform using different windows (Hanning and Sine) which have different edge slopes.

In the past several decades, there has been much development of the EXAFS theory to describe the oscillations above the absorption edge. It is now considered generally well understood within the confines of acceptable approximations. The theoretical development has led to an EXAFS equation that quantitatively parameterizes the EXAFS data,

$$\chi(k) = \sum_R S_0^2 N_R \frac{|f(k)|}{kR^2} \sin(2kR + 2\delta_c + \Phi) e^{-2R/\lambda(k)} e^{-2\sigma^2 k^2} \tag{1.8}$$

where the parameters are described below. Through fitting EXAFS data with the scattering equation (1.8), the geometric information, such as radial distances and coordination numbers of neighboring atoms, of both crystalline and non-crystalline structures can be extracted.

Due to the complexity of the quantum interaction of EXAFS, fitting the EXAFS equation requires an understanding of each of its important parameters. The interatomic

distances, R, are distances between a pair of absorber and backscatter, and the sin($2kR$) term shows the dependence of the oscillations on the energy and distances from the absorber. N_R is the coordination number. The backscattering amplitude is given by $f(k) = |f(k)|e^{i\Phi(k)}$. This function depends on the type and number of backscattering atoms. The terms δ_c and Φ give the corrections to the phase. The former and greater of the two is the phase shift due to the absorbing atom seeing the photoelectron twice. The energy dependent mean free path, λ(k), can be considered as the lifetime of the photoelectron. The term $e^{-2R/\lambda(k)}$ captures the essence of the decay of the wave, and causes the short range of EXAFS in the order of a few tens of Ångstrøms. The Debye-Waller, σ^2, in the analytical form of $e^{-2\sigma^2 k^2}$ gives the temperature dependence or thermal disorder effects. Thus as temperature increases, the EXAFS tends to broaden and lose amplitude. Also, the Debye-Waller effect increases with shorter wavelength, and thus reduces the effectiveness of EXAFS on the order of 10 $Å^{-1}$. Yet, just as importantly, this means that it has almost no effect on XANES. The final term S_0^2 is the overall amplitude factor. This is a result of the many-body effect due to the relaxation of the system. This term is still not well understood, and quantitative theory has yet to be developed. Figure 1.8 has examples for the graphical solutions of the EXAFS equation showing the effect of these parameters on extracting the geometric information.

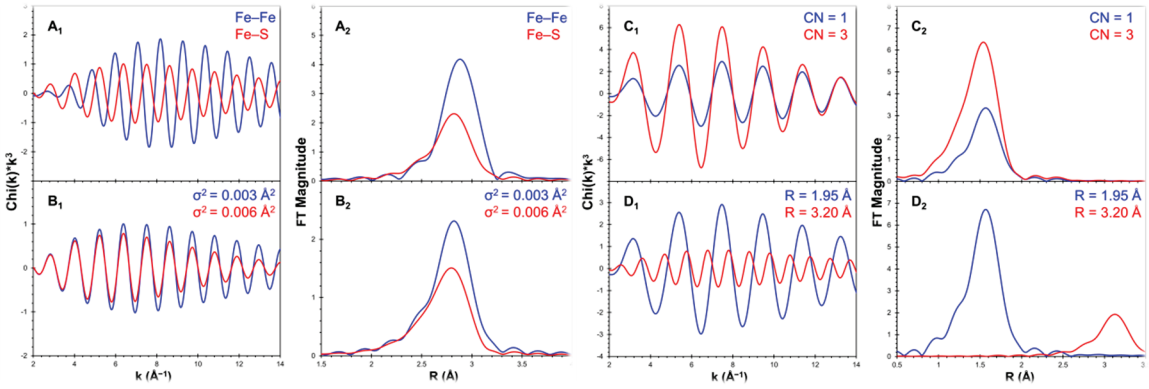

Figure 1.8. Graphical solutions to the EXAFS equation with FT for fitting parameters: (A) atomic number of scatter, (B) Debye-Waller factor (σ^2), (C) coordination number (N), and (D) interatomic distances (R)

Research Questions

Many insights into the electronic structure of iron-sulfur systems can be gained from examining the full-length scale of iron-sulfur systems from molecular (molecular clusters) to nanometer (particles) through micrometer (minerals) scale with the same technique. Multi-edge X-ray Absorption Spectroscopy (XAS) has the potential for probing the electronic and geometric structures for the full-length scale of iron-sulfur systems. Thus the research presented here applies this technique to specific iron-sulfur systems across the full-length scale, giving new insights into the electronic and geometric structures of iron-sulfur systems and providing rationalization and predictions for how these iron-sulfur systems can fill in various structural and/or catalytic roles.

Through collaborative work with research groups at MSU, the XANES and EXAFS analysis were applied to scientifically important biochemical problems, HydA (see Chapter 2) and SP lyase (see Chapter 3), providing the opportunity to learn and to become proficient in X-ray absorption analysis, in addition to contributing to obtaining

new scientific insights. Thus, determining the process of the assembly provides an important link in the understanding of active site of [FeFe]-hydrogenase. $HydA^{\Delta EFG}$ is the [FeFe]-hydrogenase structural protein expressed in the absence of the maturation machinery. At the time of the research, the roles of the maturation proteins were somewhat unknown with the possibility that they were directed at the synthesis of the entire 6Fe-containing H-cluster, the 2Fe subcluster, or only the unique ligands of the 2Fe subcluster. To determine the role of the maturation proteins, an EXAFS analysis was employed to determine the structure of the metal binding site of HydA, which is the structural scaffold protein to [FeFe]-hydrogenase. Furthermore, to further develop the methodology of EXAFS applied to non-crystalline materials of unknown or limited composition details. These methods developed in Chapter 2 were used to characterize Spore photoproduct lyase (SP lyase), a member of the radical SAM superfamily, along with Fe and S K-edge XANES to elicit the electronic change in the absence and presence of *S*-adenosyl-L-methionine (SAM).

In Chapter 4, we worked on extending the XAS analysis to mid-range of the nanometer scale. Due to the surprising complexity of particle chemistry, this is an unfinished study, and the results reported here are not yet ready for a peer-review publication. Although the work needs to be continued to fully understand the electronic and geometric structures of particles at the nanometer scale, we learned much about the XAS detection methods and possible connections between molecular and micrometer scale. We took advantage of this in the remaining chapters.

In Chapter 5 and 6, we used the tools of the previous chapters to advance our understanding of the micrometer scale. Since iron-sulfur minerals are found throughout the Earth's surface, there is a considerable amount of literature on iron-sulfur minerals; however, it is limited to specific electronic and structural information. Due to the catalytically active iron-sulfur clusters of small molecule metalloenzymes, iron-sulfur minerals could be candidates for developing novel catalytic materials. Here we investigated the modified surface of pyrite with multi-edge XAS, and employed a detection method-based description of layered structures that allowed us to create the model of the modified pyrite surface.

CHAPTER 2

IRON K-EDGE EXAFS STUDY OF HYDA

Introduction

The [NiFe]- and [FeFe]-hydrogenases are widely distributed in nature and efficiently catalyze the reversible oxidation of molecular hydrogen ($H_2 \leftrightarrow 2H^+ + 2e^-$). The [NiFe]-hydrogenases, present in archaea and bacteria, generally function to oxidize molecular H_2 and provide reducing equivalents for metabolic processes, while the [FeFe]-hydrogenases, present in bacteria and eukarya, function more broadly to catalyze both proton reduction and H_2 oxidation[26, 76]. Recently, there has been a growing interest in these metalloenzymes because of their inherent applicability in the development of renewable H_2-based energy technology. The active sites for both [NiFe]- and [FeFe]-hydrogenases have been determined by X-ray crystallography. The structure and spectroscopic techniques revealed the presence of π acceptor CO and CN^- ligands, which are un-common in biology. These diatomic ligands stabilize low-spin and low-valent oxidation states of the metal centers at the active sites. For the [NiFe]-hydrogenase, the active sites from a variety of different sulfate-reducing bacterial sources have been determined to consist of a Ni atom coordinated to an Fe atom via two thiolate ligands and a bridging oxygen species.[77] The Ni atom is further coordinated by two cysteine ligands from the protein, while the Fe atom is coordinated to two terminal CN^- ligands and one

---

This section contains text that has been coauthored by David W. Mulder, Danilo O. Ortillo, David J. Gardenghi, Anatoli V. Naumov, Shane S. Ruebush, Robert K. Szilagyi, BoiHanh Huynh, Joan B. Broderick, and John W. Peters (2009) *Biochemistry* 48, 6240-6248. Only the EXAFS analysis was done by David J. Gardenghi.

terminal CO ligand. In comparison, the [FeFe]-hydrogenase active site contains a 6Fe-containing complex cluster termed the H-cluster, as determined for *Clostridium pasteurianum* (CpI)[18, 78] and *Desulfovibrio desulfuricans*.[17, 79] The H-cluster consists of a [4Fe-4S] subcluster coordinated to a 2Fe subcluster via a cysteine thiolate ligand. The two Fe centers in the 2Fe subcluster are bridged via a five-atom dithiolate ligand and a CO ligand. The chemical composition of the dithiolate ligand has not yet been determined unambiguously and has been proposed to be dithiomethylether, propane dithiolate, or dithiomethylamine.[17, 78, 79] In addition, both Fe centers contain terminal CO and CN^- ligands. For the presumed oxidized state of CpI, a water molecule is present at the distal Fe center in the proximity of the [4Fe-4S] subcluster.

Biosynthesis and maturation of the [NiFe]-hydrogenases have been thoroughly studied, including identification of at least six gene products involved in formation of active [NiFe]-hydrogenases and the interactions between gene products during maturation. The metabolic source of diatomic CN^- ligands has been identified to be carbamoyl phosphate,[80] whereas the metabolic source for the CO ligand is still in question. In contrast, relatively little was known concerning the biosynthesis and maturation of [FeFe]-hydrogenases. By analysis of several mutant strains of *Chlamydomonas reinhardtii* that are unable to produce hydrogen, the genes *hydEF* and *hydG* were discovered to be required for maturation of [FeFe]-hydrogenases.[81] Subsequent expression studies revealed that formation of an active [FeFe]-hydrogenase was achieved only when HydA was heterologously expressed in a background of coexpressed gene products HydEF and HydG in *Escherichia coli.*[81] In most organisms,

hydEF exists as two separate genes, hydE and hydF,[81] and it has been shown that the coexpression in *E. coli* of HydE, HydF, and HydG from *Clostridium acetobutylicum* with the [FeFe]-hydrogenase structural gene product from various algal and bacterial sources is sufficient to effect expression of active [FeFe]-hydrogenase.[82] Deduced amino acid sequence analysis of HydE, HydF, and HydG gene products reveals HydE and HydG to be radical-SAM iron-sulfur enzymes as they both have the C-X3-C-X2-C radical-SAM signature motif and HydF to be a GTPase.[80, 81] Also, preliminary biochemical characterization of HydE and HydG has revealed associated SAM cleavage activity.[83] In addition, it has been shown that upon reconstitution HydF binds an iron-sulfur cluster and exhibits GTPase activity.[84]

The involvement of HydE, HydF, and HydG maturation enzymes in the biosynthesis of the H-cluster was further elaborated when it was shown that HydA, expressed in a genetic background devoid of HydE, HydF, and HydG ($HydA^{\Delta EFG}$), is a stable protein capable of being activated *in vitro* by the aforementioned proteins.[85] It was also determined that HydF behaves as a scaffold protein in which an H-cluster precursor is assembled and can be subsequently transferred to $HydA^{\Delta EFG}$, resulting in the formation of an active [FeFe]-hydrogenase.[86] Both *in vitro* activation studies imply that cluster biosynthesis does not take place on the structural protein ($HydA^{\Delta EFG}$) and that a chemical precursor to the H-cluster is synthesized in the absence of $HydA^{\Delta EFG}$ that upon transfer to $HydA^{\Delta EFG}$ results in its activation. Although no chemical precursors or intermediates to the H-cluster have yet been characterized or even identified, it can be hypothesized that HydE, HydF, and HydG are directed toward the synthesis of (1) the entire 6Fe-containing

H-cluster, (2) the 2Fe subcluster of the H-cluster, or (3) the biologically unique ligands of the 2Fe subcluster of the H-cluster. The characterization of $HydA^{\Delta EFG}$ provides a critical link in our understanding of this fascinating process by defining the substrate for the HydA maturation proteins.

HydA from the eukaryotic green algae *C. reinhardtii* contains only the H-cluster binding domains and represents the simplest [FeFe]-hydrogenase known. Unlike [FeFe]-hydrogenases from *Cl. pasteurianum* and *D. desulfuricans*, the [FeFe]-hydrogenases from eukaryotic green algae do not contain additional accessory Fe-S clusters with plant-type ferredoxin domains that would complicate spectroscopic characterization of the Fe-S clusters present at the active site.[87-89] The Peters lab has been able to anaerobically purify a stable $HydA^{\Delta EFG}$ that is capable of being activated *in vitro* by extracted HydE, HydF, and HydG enzymes. Specific activities of the six separate $HydA^{\Delta EFG}$ protein purifications after *in vitro* activation with HydE, HydF, and HydG enzymes ranged from 10 to 38 μmol of H_2 min^{-1} mg^{-1} $HydA^{\Delta EFG}$. For in vivo coexpression of HydA from *C. reinhardtii* with the maturation genes from *Cl. acetobutylicum* in *E. coli*, H_2 evolution activity was previously reported to be 150 μmol of H_2 min^{-1} mg^{-1}.[82] The difference in activity between *in vitro* and in vivo expression systems is likely attributed to the low occupancy of H-cluster activating precursors assembled by HydE, HydF, and HydG, as well as the heterogeneity of the maturation system.[86] The iron and sulfur analyses following purification of $HydA^{\Delta EFG}$ suggested the formation of incomplete Fe-S clusters. It is important to note that the amount of Fe and S^{2-} bound per $HydA^{\Delta EFG}$ varied slightly between the different purifications, suggesting that the Fe-S cluster present may be

slightly labile during purification. Also, low-temperature X-band EPR spectrum of reduced $HydA^{\Delta EFG}$ contains S=1/2 signal and characteristic g values that can be assigned to a reduced $[4Fe\text{-}4S]^{+}$ cluster[90].

It was previously reported that $HydA^{\Delta EFG}$ can be activated by cell extracts containing the maturation enzymes HydE, HydF, and HydG[85]. This observation, coupled with the evidence described above for a [4Fe-4S] cluster in $HydA^{\Delta EFG}$, suggested that the [4Fe-4S] form of $HydA^{\Delta EFG}$ is the substrate for assembly of the H-cluster by HydE, HydF, and HydG and further that the [4Fe-4S] cluster present in $HydA^{\Delta EFG}$ becomes part of the H-cluster upon activation. To further explore the requirement for a preformed [4Fe-4S] cluster in $HydA^{\Delta EFG}$ during activation, $HydA^{\Delta EFG}$ was chemically reconstituted with $FeCl_3$ and Na_2S. Iron analysis of the reconstituted $HydA^{\Delta EFG}$ suggested an increase in cluster formation per protein, and the EPR spectrum of reconstituted reduced $HydA^{\Delta EFG}$ was essentially identical to that of the as-isolated enzyme indicating the presence of a [4Fe-4S] cluster. The *in vitro* activation of the reconstituted $HydA^{\Delta EFG}$ with maturation proteins showed hydrogenase activity approximately 2-fold greater than that of the as-isolated $HydA^{\Delta EFG}$ activated with HydE, HydF, and HydG. These observations suggested that the [4Fe-4S] form of HydA is the substrate for H-cluster assembly by HydE, HydF, and HydG, as increasing the [4Fe-4S] content improves the ability to activate $HydA^{\Delta EFG}$.

To further explore the hypothesis that the [4Fe-4S] cluster present in $HydA^{\Delta EFG}$ is required for *in vitro* activation with HydE, HydF, and HydG, the apo-$HydA^{\Delta EFG}$ was prepared and then subsequently reconstituted, and both apo and reconstituted samples

were subjected to *in vitro* activation by HydE, HydF, and HydG. The apo-HydA$^{\Delta EFG}$ was found to contain zero Fe atoms per HydA$^{\Delta EFG}$, and exhibited no hydrogenase activity. Following chemical reconstitution, the apo-HydA$^{\Delta EFG}$ contained four iron atoms per protein and had an EPR spectrum essentially identical to that of the as-isolated enzyme. The following *in vitro* activation of the reconstituted enzyme with HydE, HydF, and HydG produced hydrogenase activity at a level of 90% of that of as-isolated HydA$^{\Delta EFG}$.

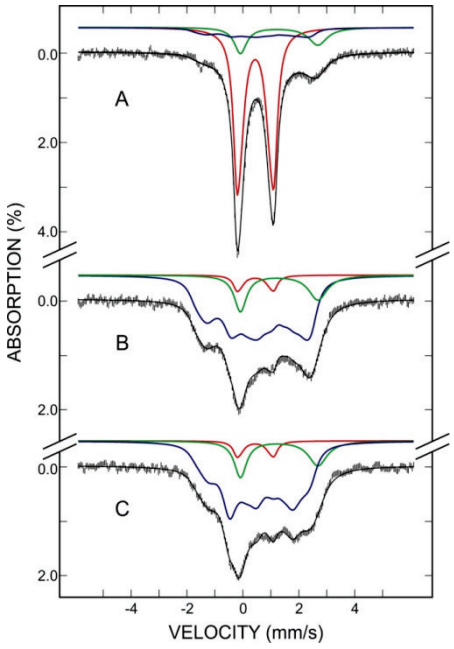

Figure 2.1. Mössbauer spectra from the Huynh lab of the as-purified (A) and dithionite-reduced (B and C) HydA$^{\Delta EFG}$. The spectra (hatched marks) were recorded at 4.2 K in a magnetic field of 50 mT applied parallel (A and B) and perpendicular (C) to the γ radiation. The solid lines plotted above the data are simulated spectra for the [4Fe-4S]$^{2+}$ cluster (red), [4Fe-4S]$^{1+}$ cluster (blue) and Fe^{II} impurities (green), normalized to the following percent absorptions: (A) 70% [4Fe-4S]$^{2+}$, 15% [4Fe-4S]$^{1+}$ and 15% Fe^{II}, (B and C): 6% [4Fe-4S]$^{2+}$, 76% [4Fe-4S]$^{1+}$ and 18% Fe^{II}. The black lines overlaid with the experimental spectra are composite spectra

Figure 2.1 shows the Mössbauer spectra from the Huynh lab at Emory University of the ^{57}Fe-enriched HydA in its as-purified (A) and dithionite-reduced (B and C) forms.

Their analysis of the data indicated that all three spectra are composed of three sub spectral components: a central quadrupole doublet (solid red lines in Figure 2.1), a magnetically split spectrum (blue lines), and an outer quadrupole doublet with broad and asymmetric absorption lines (green lines). The central quadrupole doublet is attributed to a $[4Fe\text{-}4S]^{2+}$ cluster and can be simulated as a superposition of two unresolved equal-intensity quadrupole doublets representing the two mixed-valence Fe^{II}-Fe^{III} pairs within the cluster. The two unresolved doublets are typical for $[4Fe\text{-}4S]^{2+}$ clusters.[91, 92] As reported above, reduced HydA displays an S = 1/2 EPR signal that can be assigned to a $[4Fe\text{-}4S]^{+}$ cluster. The magnetic Mössbauer spectral component is therefore attributed to this S = 1/2 Fe cluster. Consistent with the $[4Fe\text{-}4S]^{+}$ assignment, initial analysis of this spectral component indicated that it may be simulated as a superposition of two spectral components arising from the $Fe^{II}Fe^{II}$ and $Fe^{II}Fe^{III}$ pairs of a $[4Fe\text{-}4S]^{+}$ cluster.[91, 92] The outer quadrupole doublet is attributed to non-cysteine-coordinated extraneous Fe(II) impurities, which may be generated via cluster degradation.

Decomposition of the Mössbauer spectra into the above-described spectral components shows that in the as-purified $HydA^{\Delta EFG}$ sample (see Figure 2.1A) the majority (70%) of the Fe is present in the oxidized $[4Fe\text{-}4S]^{2+}$ form while a small percentage (15%) is in the reduced $[4Fe\text{-}4S]^{+}$ form. The remaining Fe (15%) is present as Fe(II) impurities. Upon reduction (see Figure 2.1B,C), a substantial amount of the $[4Fe\text{-}4S]^{2+}$ clusters are reduced to $[4Fe\text{-}4S]^{+}$ clusters, resulting in a decrease in the Mössbauer absorption of the $[4Fe\text{-}4S]^{2+}$ cluster from 70 to 6% and an increase in the $[4Fe\text{-}4S]^{+}$ absorption to 76%. The Fe(II) impurities also increase slightly to 18%, suggesting that

the [4Fe-4S] cluster in HydA$^{\Delta EFG}$ is slightly unstable under dithionite reducing conditions. Thus, the Mössbauer data unambiguously show that the as-purified HydA$^{\Delta EFG}$ contains predominantly [4Fe-4S] clusters. Taking into consideration the Fe and protein content determined for the as-purified ^{57}Fe-enriched HydA$^{\Delta EFG}$ and the total percent absorption of the [4Fe-4S] cluster detected by the Mössbauer measurement (85%), the as-purified HydA$^{\Delta EFG}$ had a stoichiometry of 0.4 [4Fe-4S] cluster/HydA$^{\Delta EFG}$

In this study, we present X-ray Absorption spectroscopic characterizations of HydA$^{\Delta EFG}$ from *C. reinhardtii* to provide insights into the [FeFe]-hydrogenase maturation and H-cluster biosynthesis. We start with X-ray absorption data and fit the EXAFS with various models of Fe-S cluster. The models were then constrained based on Mössbauer data obtain previously. For each model, we evaluated the overall performance of the fitting through the examination of the R-factor and parameters' chemical and physical relevance.

Method and Materials

Fe K-Edge X-ray Absorption Spectroscopy

HydA$^{\Delta EFG}$ samples (1.9 mM) were prepared from the HydA$^{\Delta EFG}$ protein isolated as described in collaborative work[93]. The EXAFS cells (Delrin) sealed with thin Fe-free Kapton tape were loaded with ~100 μL of sample. Fe K-edge X-ray absorption spectroscopic (XAS) measurements were conducted at beamline 7-3 (BL7-3) of the Stanford Synchrotron Radiation Lightsource (SSRL) under storage ring (SPEAR3) conditions with an energy of 3 GeV and a current of 100-80 mA on two different

occasions. BL7-3 is a 20-pole, 2 T Wiggler beamline equipped with a Si(220) downward reflecting, double-crystal monochromator. Data were collected in the energy range from 6785 eV to k = 17 $Å^{-1}$ above the Fe K-edge using an unfocused beam. The frozen solution samples were mounted under liquid nitrogen and measured in a liquid He cryostat at ~11 K. The beamline parameters were optimized at 8000 eV. The Fe Kα fluorescence signal was collected using a 30-element Ge array detector and with a Soller slit and Z−1 (Mn) filter. The energy windowing of the detector was carefully done to minimize the fluorescence signal due to scattering and other non-Fe Kα emission sources. The data were calibrated to the first rising-edge inflection point of the XAS spectra that was assigned to 7111.2 eV of an iron foil. ATHENA[94], a graphical-user interface to IFEFFIT[95], was used for averaging and background subtraction. The data are averages of at least five scans before normalization or background subtraction. ATHENA[94] and AUTOBK[96] were used to fit a spline to the post-edge region and to obtain the EXAFS, where the spline fitting parameter, R_{bkg}, was set to one. ARTEMIS[94] and FEFF[97, 98] were used to model and fit the data and calculate Fe…Fe and Fe-S scattering paths, respectively. The structural models used in scattering calculations were derived from combination of average Fe…Fe and Fe-S distances of reduced[99] and oxidized[100] [4Fe-4S] model compounds.

Results and Analysis

EXAFS can provide useful geometric information on non-crystalline compounds such as protein active sites. The drawback is that both chemical and structural insights are

needed to properly model the EXAFS. As with any non-crystalline compound, this could severely limit the information that EXAFS could provide reliably. This issue can be seen in first modeling the as-isolated HydA sample with an [2Fe-2S] cluster (see Figure 2.2). Although not a perfect fit, it shows the flexibility of the EXAFS equation and that a using an incorrect model with reasonably good fitting could lead to incorrect results. Even with variation of coordination numbers and other parameters, the fits are reasonable both in the R-factor and chemically acceptable parameters. This can be attributed to two main factors. The first factor is the actually composition of sample. The sample purification does not guarantee that all proteins will have completely formed active sites. There could be no or only partial formed clusters in the purified proteins. The second factor is the theoretical estimates of chemically reasonable parameters. The phase and amplitude functions of the EXAFS equation are calculated using estimated path length and scatters, and these might not be accurate with the actual system in question. Both the number of absorbers and Debye Waller factor affect the amplitude, and since the latter does not yet have good *ab inito* approach, the determination of the former is less accurate. The phase information is directly related to the scattering atom and can be calculated with a good degree of accuracy. The issue arises in distinguishing neighboring scattering atoms. Elements next to each other on the periodic table have similar potentials, and thus, the scattering characteristics of the photoelectron are difficult to distinguish. Due to the uncertainty of the parameters and range of possible models, fitting an ill-defined iron-sulfur system results in a range of iron-sulfur clusters combinations from [2Fe-2S] to [4F-4S] clusters. Thus, without prior knowledge about the system, the appropriateness of the

initial model and the adequacy of the EXAFS analysis are questionable. Therefore, in this study, Mössbauer speciation information was used to constrain the fits.

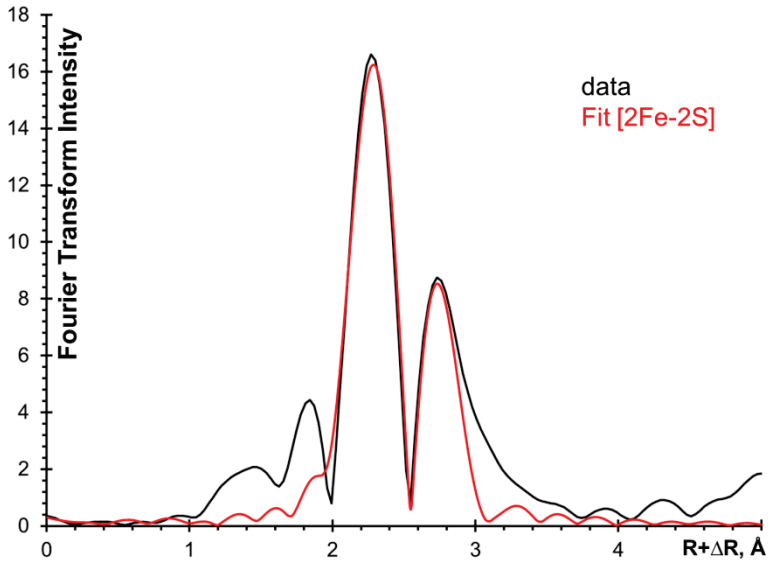

Figure 2.2. FT-EXAFS plot for as-isolated HydA$^{\Delta EFG}$ sample with a representative fit of [2Fe-2S] cluster

Using Mössbauer speciation information, a stepwise fitting process was developed to analyze protein bound iron-sulfur clusters. The first step in processing XAS data is to perform the smooth pre-edge background to get rid of any instrumental background and absorption from other edges, and then normalize the edge jump to one to represent one absorber. The next step is to obtain the EXAFS, $\chi(k)$, in momentum space, k. This is done by subtracting a smooth post-edge background that approximates the absorption of one absorber from post-edge. The AUTOBK algorithm is recommended for obtaining $\chi(k)$ due to its stability and reproducibility. To reduce the high-frequency noise and the small residual background, the windowing of the Fourier transform of $\chi(k)$ weighted by k^3 to amplify the oscillations at higher k is selected based upon quality of

data usually between $k = 2 – 14$ Å^{-1}. The next step is to build a model of your system. Due to the uncertainty of the structure of the system and the multiple absorber environments, crystal structure models tend to underestimate the amplitude function. Thus, the amplitude and phase functions were calculated using FEFF 8.4 base on single scattering paths. Since we are dealing with iron-sulfur clusters, these single scattering paths were from the Fe…Fe, Fe–S^{t}(thiolate), and Fe–S^{s}(sulfide) paths. Three main parameters affect the scattering paths: interatomic distances, R, Debye-Waller factor,σ^2, and coordination number, N. The overall amplitude factor, S_0^2, and the absorption edge energy, E_0, are linked for all scattering paths. To begin nonlinear least-squared fitting of $\chi(k)$ weighted by k^3, all parameters are constrained, and fitting is done stepwise such that only one or two parameters are unconstrained during a fit. Constraints can be applied to each parameter such as linking or defining a mathematical relationship between parameters. Thus, Mössbauer speciation information was used to constrain the amplitude and interatomic distance for each scattering path for the initial parameters. Therefore, this allows the user to control the deviations from the model and to minimize large and unreasonable deviations. In the subsequent fit, new and previous parameters were unconstrained and constrained, respectively, and the fit started with the previous fitted parameter values. This process is then done iteratively to obtain the most reasonable fit.

Fe K-Edge X-ray Absorption
Spectroscopic Characterization of HydA$^{\Delta EFG}$

The Fourier transforms of EXAFS (FT-EXAFS) for the as-isolated HydA sample (black trace) and with a representative fit (red trace) are shown in Figure 2.3. The fitting

parameters are summarized in Table 2.1. Among numerous reasonable fits, Table 2.1 and Figure 2.3 report the one that was obtained using the Mössbauer results (see above) as constraints for the amount and distribution of various Fe sites. The initial parameters of the fit were set to represent the 70% oxidized and 15% reduced protein-embedded [4Fe-4S] cluster content, and the overall amplitude factor was set to one. The average Fe…Fe, Fe–S^t, and Fe–S^s distances in synthetic [4Fe-4S] complexes are 2.74 ± 0.01, 2.25 ± 0.01, and 2.27 ± 0.03 Å, respectively[9]. The protein-bound counterparts of Fe-S distances tend to be ~0.02 Å longer due to dipole and hydrogen bonding interactions involving the sulfides and thiolate sulfurs, which reduces the nucleophilicity of the sulfur atoms and thus the covalency of the sulfur-iron bonds.

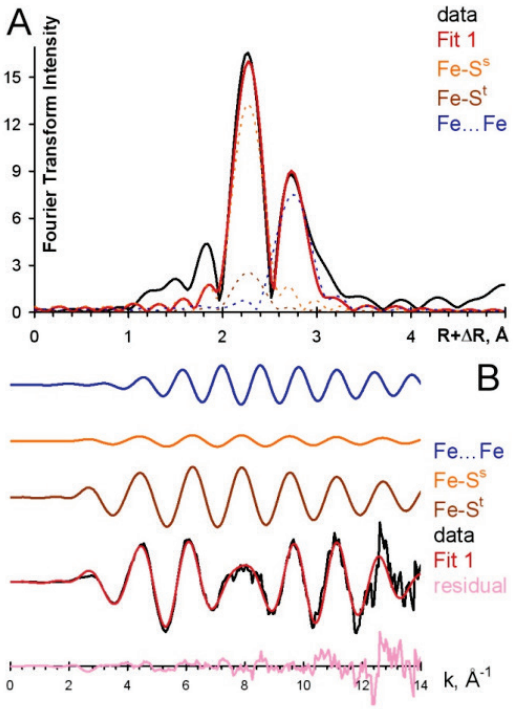

Figure 2.3. FT-EXAFS plot (A) and individual EXAFS contributions (B) for as-isolated $HydA^{\Delta EFG}$ sample with a representative fit containing Fe…Fe, Fe-S(sulfide), Fe-S(thiolate) scattering paths

Table 2.1. Representative fitting parameters for the as-isolated $HydA^{\Delta EFG}$ sample using Fe-S composition from Mössbauer measurements

scatters	parameters[a]	fitted value
Fe-S^s	r, Å	2.27
	N, –	3
	A, –	0.80
	σ^2, $Å^2$	0.003
Fe-S^t	r, Å	2.27
	N, –	1
	A, –	0.46
	σ^2, $Å^2$	0.003
Fe…Fe	r, Å	2.72
	N, –	3
	A, –	0.44
	σ^2, $Å^2$	0.003
	R (fit)	$7.65 \cdot 10^{-4}$
	E_0, eV	0.790

[a] r: scattering path, N: coordination number, A: scattering path amplitude, σ^2 Debye-Waller factor as a measure of thermal displacement and disorder;
k^3-weighted data fit in the k-range of 1-14 $Å^{-1}$; FT-EXAFS window range fitted 1.5-3.3 Å

These differences between the synthetic model and protein-bound Fe-S clusters can be observed by EXAFS as demonstrated by a series of FT-EXAFS analyses of Fe-S clusters.[101-103] Using the initial distances with standard deviations as initial Debye-Waller factors of 2.74 ± 0.005, 2.24 ± 0.003, and 2.28 ± 0.003 Å for Fe…Fe, Fe–S^t, and Fe–S^s scattering paths, respectively, we obtained a reasonable fit that is shown in Figure 2.3. To prevent negative Debye-Waller factors (σ^2) and large deviations of the edge positions (E_0), we obtained the final fit by linking all the σ^2 and E_0 values while allowing the individual path lengths and their amplitudes to vary. The parameters in Table 2.1 fit the most of experimental data (black trace) acceptably well, but a poor fit was found at the shorter distances. The residual FT-EXAFS intensity at these distances is consistent with the presence of ~15% free iron that is likely partially solvated and/or coordinated with low-Z atoms, such as O and N from protein residues as suggested by Mössbauer results. The peak at around 1.9 ± 0.1 Å reasonably can be fitted with a Fe center surrounded by

six low-Z (O and N) scatterers in 15% abundance. The relatively short Fe-O distance of 1.9 Å is indicative of the presence of negatively charged O or N ligands for the Fe(II) impurities (see above). The fit components and parameters for the latter are given in Figure 2.4 and Table 2.2. For both FT-EXAFS fits, the resulting Fe…Fe (2.71–2.72 Å) and Fe–S (2.27 Å) distances are highly similar to those observed for the oxidized and reduced [4Fe-4S] cluster in Av2 (2.72 and 2.73 Å, and 2.27 and 2.29 Å, respectively)[102] and thus further support the presence of the [4Fe-4S] cluster in HydA$^{\Delta EFG}$.

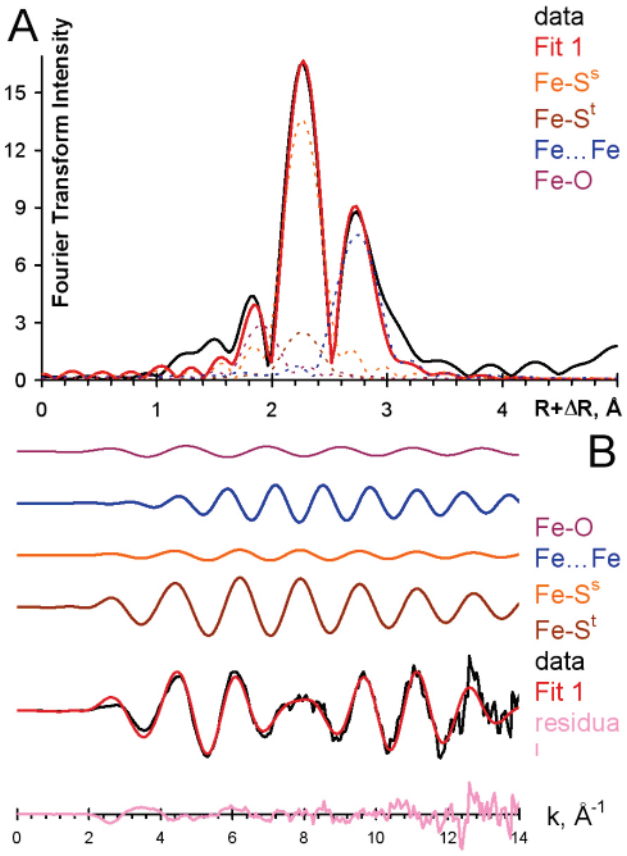

Figure 2.4. FT-EXAFS plot (A) and individual EXAFS contributions (B) for as-isolated HydA$^{\Delta EFG}$ sample with a representative fit containing Fe…Fe, Fe-S(sulfide), Fe-S(thiolate), Fe- low Z(O/N) scattering paths

Table 2.2. Representative fitting parameters for the as-isolated HydA$^{\Delta EFG}$ sample using Fe-S composition from Mössbauer measurements including the free iron(II) content

scatterers	parameters[a]	fitted value
Fe-S^{s}	r, Å	2.27
	N, –	3
	A, –	0.88
	σ^2, Å^2	0.004
Fe-S^{t}	r, Å	2.27
	N, –	1
	A, –	0.48
	σ^2, Å^2	0.004
Fe…Fe	r, Å	2.71
	N, –	3
	A, –	0.48
	σ^2, Å^2	0.004
	E_0, eV	-0.436
Fe-O	r, Å	1.87
	N, –	1
	A, –	0.55
	σ^2, Å^2	0.002
	E_0, eV	4.609
	R (fit)	$3.89 \cdot 10^{-4}$
	E_0, eV	-0.436

[a] r: scattering path, N: coordination number, A: scattering path amplitude, σ^2 Debye-Waller factor as a measure of thermal displacement and disorder;
k^3-weighted data fit in the k-range of 1-14 Å^{-1}; FT-EXAFS window range fitted 1.5-3.3 Å

Conclusion

This EXAFS characterization of HydA$^{\Delta EFG}$ from *C. reinhardtii* indicated that a [4Fe-4S] cluster is present in HydA$^{\Delta EFG}$. From the biochemical studies,[93] the presence of the iron-sulfur cluster was indicated by chemical analysis for iron and acid-labile sulfide. The Mössbauer and EPR techniques that together with XAS confirmed this to be a [4Fe-4S]$^{2+/+}$ cluster, with an incomplete loading of ~40%, in the as-isolated enzyme. Furthermore, this [4Fe-4S] cluster-containing enzyme is capable of undergoing activation by HydE, HydF, and HydG to produce an active hydrogenase. Apo-HydA$^{\Delta EFG}$, in contrast, did not produce an active hydrogenase upon incubation with HydE, HydF, and HydG under activation conditions. These results suggested that the [4Fe-4S] cluster

present in the as-isolated enzyme is required to be present on $HydA^{\Delta EFG}$ prior to activation by HydE, HydF, and HydG. Further support for this conclusion was provided by the observation that apo-$HydA^{\Delta EFG}$ reconstituted to contain a [4Fe-4S] cluster could subsequently be converted to an active hydrogenase by HydE, HydF, and HydG. Together, our results provide important new insights into the process by which HydA is matured into an active enzyme *in vivo*.

EXAFS analysis is a powerful tool in determining geometric structures of protein bound iron-sulfur clusters, and combined with Mössbauer analysis, the ambiguity of the model based data interpretation can be reduced.

CHAPTER 3

COMBINED MÖSSBAUER AND MULTI-EDGE X-RAY ABSORPTION SPECTROSCOPIC STUDY OF THE IRON-SULFUR CLUSTER IN SPORE PHOTOPRODUCT LYASE

Contributions of Authors and Co-Authors

Manuscript in Chapter 3

Author: Sunshine C. Silver

Contributions: Prepared SP lyase samples for Mössbauer, Fe and S K-edge X-ray absorption spectroscopy and wrote the manuscript.

Co-author: David J. Gardenghi

Contributions: Performed data collection, analysis of the Fe and S K-edge XAS samples, and generated XAS figures. Assisted in writing the manuscript.

Co-author: Eric Shephard

Contributions: Assisted in computational analysis.

Co-author: BoiHanh Huynh and Sunil G. Naik

Contributions: Collected and analyzed data for Mössbauer spectroscopy.

Co-author: Robert K. Szilagyi

Contributions: Assisted in data collection, analysis of XAS samples and computational analysis. Provided critical discussions of results, implications for research, and feedback on manuscript at all stages of writing.

Co-author: Joan B. Broderick

Contributions: Provided direction and overview of the sample preparation, interpretation of all spectroscopic results and preparation of the manuscript.

Manuscript Information Page

Sunshine C. Silver, David J. Gardenghi, Eric M. Shepard, Sunil G. Naik, BoiHanh Huynh, Robert K. Szilagyi, and Joan B. Broderick

Journal: Biochemistry

Status of the manuscript:
_X_ Prepared for submission to a peer-reviewed journal
____ Officially submitted to a peer-reviewed journal
____ Accepted by a peer-reviewed journal
____ Published in a peer-reviewed journal

Abstract

Spore photoproduct lyase (SP lyase) is a member of the radical SAM superfamily and catalyzes the direct reversal of the spore photoproduct (SP, 5-thyminyl-5,6-dihydrothymine), a thymine dimer specific to bacterial spores, to two thymines. SP lyase requires *S*-adenosyl-L-methionine (SAM) and a redox active [4Fe-4S] cluster for catalysis. Mössbauer analysis of anaerobically purified SP lyase defined the presence of a mixture of cluster states with the majority (40%) as $[2Fe\text{-}2S]^{2+}$ clusters and a smaller amount (15%) as $[4Fe\text{-}4S]^{2+}$ clusters. Upon reduction, the clusters are converted primarily (60%) to $[4Fe\text{-}4S]^{1+}$ cluster. This information allowed us to quantitatively analyze iron and sulfur K-edge X-ray absorption spectroscopic measurements to further characterize the electronic and geometric structures of the [4Fe-4S] cluster, and the interaction between the cluster and SAM. The Fe K-edge EXAFS provides evidence for a slight distortion of the cluster upon introduction of SAM, based on the appearance of a new Fe...Fe scatterer at around 3.0 Å. Upon reduction, the Fe K-edge XANES shows a shift to lower energy relative to the spectrum of the as-purified protein. The XANES spectra of reduced SP lyase in the absence and presence of SAM overlay, indicating that SAM is not undergoing reductive cleavage in the presence of reduced SP lyase. Using biochemical and Mössbauer data, we were able to separate out spectral contributions from [2Fe-2S] and [4Fe-4S] cluster states at the S K-edge that revealed electronic structural changes in the metal-ligand bonding as a function of the presence of SAM cofactor. The spectroscopic findings were further corroborated by density functional theory calculations.

Introduction

Members of the radical SAM superfamily utilize *S*-adenosyl-L-methionine (SAM) and a redox active [4Fe-4S] cluster to carry out diverse radical reactions including rearrangements, sulfur-insertions and oxidations. They also function in biosynthesis pathways of DNA precursor, vitamin, cofactor, and antibiotics, as well as the assembly of complex metallocofactors.[25, 104, 105] Enzymes in this superfamily typically contain a conserved CX_3CX_2C sequence that coordinates three of the iron atoms of the [4Fe-4S] cluster. Electron-nuclear double resonance and X-ray crystallography of several members of the superfamily have shown that the fourth iron is coordinated by the amino and carboxylate moieties of SAM.[19, 106-115] Mechanistic studies of these enzymes suggest that an inner-sphere electron transfer from a reduced $[4Fe\text{-}4S]^+$ cluster to the sulfonium of SAM leads to homolytic S-C(5') bond cleavage to generate a 5'-deoxyadenosyl radical (dAdo•) intermediate, which abstracts a hydrogen atom from substrate to initiate a radical-based transformation.[106-108, 116, 117]

Spore photoproduct lyase (SP lyase) is a member of the radical SAM superfamily that catalyzes the direct reversal of a specific DNA photoproduct, 5-thyminyl-5,6-dihydrothymine (spore photoproduct or SP), back to two thymines (Figure 3.1).[118-121] The methylene-bridged thymine dimer SP is the primary photoproduct when bacterial spores are subjected to UV radiation, and is rapidly repaired upon spore germination.[119, 120, 122, 123] The Broderick lab previously demonstrated that SP repair is initiated by abstraction of an H atom from C6 of SP.[121, 124] The resulting substrate radical is thought to promote a radical-mediated β-scission of the C-C bond linking the two thymines; the resulting

product radical then abstracts an H atom from 5'-deoxyadenosine to generate dAdo•, which ultimately re-forms SAM.[121, 124, 125] More recent work has demonstrated that only the 5*R* diastereomer of SP is repaired by SP lyase,[126-128] despite earlier reports pointing to the opposite stereospecificity.[129, 130]

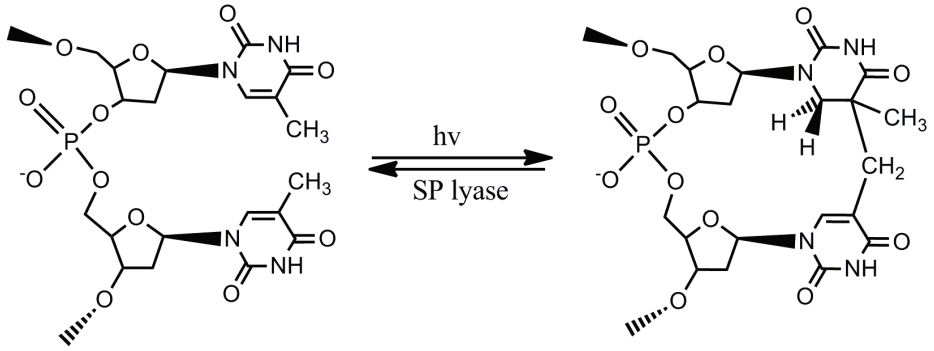

Figure 3.1. Formation and repair of spore photoproduct (thymine dimer) by the metalloenzyme Spore Photoproduct lyase

Previous spectroscopic studies of SP lyase have demonstrated the presence of a single iron-sulfur cluster,[118] which appears as a mixture of cluster states when the enzyme is purified *in vitro.*[124, 127, 130, 131] The UV-visible absorbance spectrum of purified SP lyase shows a broad shoulder with a maximum of 413 nm, similar to other members of the radical SAM superfamily,[127, 132, 133] with an additional broad feature around 600 nm that may indicate some [2Fe-2S] cluster content in the enzyme.[134] Upon reduction in the presence of dithiothreitol and 5-deazariboflavin, the UV-visible spectral features decrease in intensity, resulting in a single broad peak at ~410 nm. The UV-visible spectral absorbance changes indicate a redox-active Fe-S cluster, but do not address in detail the types and concentrations of the clusters that may be present. As-purified SP lyase exhibits a nearly isotropic EPR signal centered at g = 1.99 that is characteristic of a $[3Fe\text{-}4S]^{1+}$

cluster, but this form accounts for only 3 – 4% of the total iron.[127] Reduction of the enzyme results in a nearly axial signal with g values of 2.03, 1.93 and 1.92, and is consistent with a $[4Fe\text{-}4S]^{1+}$ cluster; this signal accounts for 32 – 45% of the total iron, indicating either incomplete reduction (leaving some in an EPR-silent state) and/or substoichiometric iron-sulfur cluster in the purified protein. Addition of SAM to the reduced enzyme causes some change in line shape (g-values of 2.03, 1.92 and 1.82) and significantly lower intensity; these spectral changes are specific for the interaction of SAM with the cluster as similar molecules (5'-deoxyadenosine, methionine and *S*-adenosyl-L-homocysteine) do not yield equivalent EPR signals when added to reduced SP lyase.[127] Evidence for direct coordination of SAM to the cluster of SP lyase, in a manner similar to other radical SAM enzymes, has been provided by hyperfine sub-level Correlation (HYSCORE), a two-dimensional pulsed EPR technique.[131]

In this study, we address quantitatively the nature of cluster types present in the as-purified and reduced forms of SP lyase and whether these cluster states change in the presence of SAM. Furthermore we compare and contrast how the SAM interacts with the cluster relative to other members of the radical SAM superfamily. We also probe whether the sulfonium sulfur of SAM can interact with the [4Fe-4S] cluster in SP lyase. In order to overcome the limitations of a single spectroscopic technique, we pursued a combined multi-edge XAS and Mössbauer study. Mössbauer studies were performed to identify and quantify the various cluster types that are present in the as-purified enzyme and reduced enzyme both in the absence and presence of SAM. These speciation results were essential in fitting and deconvoluting the XANES and EXAFS features at the Fe and S K-edges to

further characterize the cluster states and the interaction of SAM with the [4Fe-4S] cluster. The experimental geometric and electronic information were further substantiated by density functional theory-based (DFT) modeling.

The BoiHanh Huynh lab's analysis of the Mössbauer spectra of ^{57}Fe-enriched SP lyase in four different states of the enzyme (anaerobically purified SP lyase, purified enzyme plus SAM, photo-reduced enzyme, and reduced enzyme plus SAM) indicated that all four states of the enzymes contain multiple Fe species. The spectra of the purified enzyme in the absence and presence of SAM were very similar, comprising a central quadrupole doublet, accounting for 55% of the total Fe absorption, and an ill-defined broad magnetic spectrum. The central quadrupole doublet can be further decomposed into two unresolved doublets. The major doublet, accounting for 40% of the Fe absorption, is indicative of a $[2Fe\text{-}2S]^{2+}$ cluster.[135] The minor doublet, accounting for 15% of the Fe absorption, is typical for $[4Fe\text{-}4S]^{2+}$ cluster.[135] As the Fe absorption percentages for the $[2Fe\text{-}2S]^{2+}$ and $[4Fe\text{-}4S]^{2+}$ clusters remained the same after addition of SAM, it appeared then that the co-substrate SAM has no detectable effects on the composition and oxidation states of the Fe-S clusters in the purified enzyme. The broad magnetic spectrum is attributed to high-spin ferric complexes, representing likely adventitious Fe bound to the N-terminal His_6 tag on SP lyase that is utilized for purification.

The spectra of the reduced enzyme in the absence and presence of SAM were also quite similar. Their analysis of these spectra indicated the presence of at least four sub spectral components. The results of the decomposition of the spectra into four identifiable components are (1) $[4Fe\text{-}4S]^{1+}$ cluster with a spin $S = 1/2$ (60% of total Fe absorption in

Table 3.1. Percent absorption of the Fe species present in the various states of SP lyase determined by Mössbauer spectroscopy

State of SP lyase	$[2Fe\text{-}2S]^{2+}$	$[4Fe\text{-}4S]^{2+}$	$[4Fe\text{-}4S]^{1+}$	$Fe^{2+}S_4$	$N/O\text{-}Fe^{2+}$	Fe^{3+}
As-purified	40%	15%				45%
As-purified + SAM	40%	15%				45%
Photo-Reduced			60%	10%	15%	15%
Reduced + SAM			45%	13%	12%	25%

the absence and 45% in the presence of SAM), (2) nitrogenous/oxygenous-coordinated Fe^{2+} species (10% in absence and 13% in presence of SAM), (3) tetrahedral sulfur-coordinated Fe^{2+} species (15% in absence and 12% in presence of SAM), and (4) a fast relaxing Fe^{3+} species (15% in absence and 25% in presence of SAM). The S=1/2 $[4Fe\text{-}4S]^{1+}$ cluster was simulated using the parameters obtained for the four-iron ferredoxin from *Bacillus stearothermophilus*.[91] The simulation of the tetrahedral-sulfur coordinated Fe^{2+} component used the parameters that are typical for the $FeS(Cys)_4$ center in rubredoxin.[135]

The Broderick lab found that the anaerobically purified SP lyase to contain iron (between 2.3 and 3.1 ± 0.2 per monomer) and acid-labile sulfide (between 2.4 and 3.6 ± 0.2 per monomer) with content dependent upon preparation. Since SP lyase requires a [4Fe-4S] cluster for catalysis, the iron and sulfide contents indicate the presence of incompletely assembled [4Fe-4S] clusters. Further, the Mössbauer data presented above demonstrated a mixture of cluster states in the anaerobically prepared SP lyase (Table 3.1). The incomplete cluster content and distribution of cluster states observed in SP lyase are likely artifacts of the *in vitro* purification procedure; such observations are not unusual for radical SAM enzymes. It is important to note, however, that upon

photoreduction the only cluster species present in SP lyase is the catalytically active $[4Fe\text{-}4S]^{+}$ state.

Materials and Methods

Preparation of XAS Samples

Iron K-edge XAS samples were prepared in two different ways by the Broderick laboratory. The samples were first prepared using SP lyase protein (0.59 mM) expressed in Tuner(DE3)pLysS *E. coli* cells as described above. As-purified samples were prepared from the anaerobically purified/dialyzed enzyme in the absence and presence of SAM (3 mM). Reduced samples were prepared, and SAM (3 mM) was added to the photoreduced enzyme as a final step in preparation. A second set of samples were prepared for both Fe K-edge and S K-edge XAS measurements for two different synchrotron data collection trips using SeMet labeled SP lyase (0.49 or 0.67 mM) and reduced by the addition of methyl viologen (3 mM), and SAM (3 mM) was added to appropriate samples. After each sample was prepared, ~100 μL was loaded into a XAS Delrin pinhole cell sealed with thin (~5 μm) iron- and sulfur-free Kapton tape (Certispec) and frozen in liquid N_2.

X-ray Absorption Spectroscopy

The X-ray absorption measurements were collected at Stanford Synchrotron Radiation Lightsource (SSRL) under storage ring (SPEAR3) condition of 3 GeV and current of 80-200 mA. The iron K-edge XANES and EXAFS were collected on the 20-pole, 2 T Wiggler beamline 7-3 (BL7-3) equipped with a Si(220) downward reflecting, double-crystal monochromator. A 30-element Ge solid-state detector windowed at the Fe

K_α emission line was used to collect data as fluorescence excitation spectra. The energy was calibrated using the first peak of the first derivative of an iron foil assigned to 7111.2 eV. During the measurement, the sample was placed in a liquid helium cryostat and maintained at a constant temperature of ~10 K. The beamline parameters were optimized at 8000 eV.

The sulfur K-edge XAS data was collected on BL6-2. The measurements utilized the 54-pole wiggler beamline 6-2 operating in high field mode of 10 kG with a Ni-coated harmonic rejection mirror and a fully tuned, liquid nitrogen-cooled Si(111) crystal monochromator. XAS measurements were collected in the energy range of 2450–2740 eV using an unfocused beam in a He-purged beam path with a multi-element Lytle fluorescence. Samples were mounted on a sample paddle at 45º to the incident beam and Lytle fluorescence detector and placed in a liquid helium flow, maintaining a constant sample temperature of approximately 100 K. The beamline parameters were optimized at 2740 eV. The incident photon energy was calibrated to the spectra of $Na_2S_2O_3 \cdot 5H_2O$ with a maximum pre-edge feature at 2472.02 eV.

The data is the average of at least five scans before background subtraction and normalization. Background correction and normalization of Fe and S K-edge XANES was performed using ADRP (Automated Data Reduction Protocol).[136] The background removal for EXAFS was performed using AUTOBK algorithm,[96] implemented with ATHENA[94] as the graphical interface. IFEFFIT[95] and FEFF 8.4,[97, 98] implemented with ARTEMIS,[94] were used to refine and model the EXAFS, respectively. Due to data collection issues, the XANES region of the reduced SP lyase samples in the presence of

SAM cofactor had to be reconstructed as an average of all available spectra. This procedure introduced a less than 5% intensity variation along the rising edge and had a negligible small effect for the EXAFS in the k = 0-3 $Å^{-1}$ region. The structural model used in calculation of amplitude and phase information was derived from a combination of average Fe…Fe and Fe-S distances of reduced and oxidized [4Fe-4S] model compounds[9]. A non-linear least-squares minimization is used to vary the model and optimize the calculated fit to the observed EXAFS.[137] Due to the presence of $Fe(SR)_4$, [2Fe-2S], and [4Fe-4S] species in the samples that can readily lead to various acceptable fits with R(fit) < 15%, the fits were strictly constrained to speciation information from Mössbauer data.

The quantitative analysis of the sulfur K-edge pre-edge features was accomplished by considering the concentration of sulfur atoms in various speciations. A normalized spline function fit to the post-edge region at 2480 eV was renormalized by taking into account the sum of the number of sulfide ions per protein subunit (as determined by the sulfide assay), the number of cysteine residues per protein unit in the background of selenomethionine, protein concentrations, and the amount of SAM added. These all contribute to the height of the edge jump; however, the pre-edge intensities will only be affected by the Fe-bound sulfur ligands. The pre-edge intensities have to then be further corrected with the total number of Fe centers present in the S-bound form, which was taken from the Mössbauer analysis.

Computational Modeling

The 2.77 Å resolution crystal structure of the pyruvate formate-lyase activating enzyme (PFL-AE) in complex with SAM and a peptide substrate[115] was used to generate the initial computational model for the evaluation of the relationship between the SAM interaction with the [4Fe-4S] cluster and the Fe…Fe distances within the cluster. While the crystal structure resolution is modest, the orientation of the three cysteine residues anchoring the Fe-S clusters can be accepted to be chemically reasonable. The electronic structured of the computational model were carefully considered by evaluating all possible combinations of ferro- and antiferromagnetically coupled [2Fe-2S] rhombs with formally $Fe^{2.5+}$ ions using the GIFA approach.[138] Regardless of the initial electronic structure and the optimization state or even the presence and nature of a ligand at the unique Fe site, the lowest energy spin coupling scheme was obtained when the Fe1 and Fe2 centers were coupled ferromagnetically, giving a $M_S = +9/2$ spin state, and this [2Fe-2S] rhomb was antiferromagnetically coupled with the ferromagnetically coupled Fe3 and Fe4 centers with $M_S = -9/2$. The Fe1 is the unique iron, and the Fe2, Fe3, Fe4 centers are connected to the protein matrix via Cys29, Cys33, and Cys36, respectively. For a representative orientation, the rhomb formed by the Cys29, Fe2, and the unique iron site Fe1 can be considered to be on top of the other rhomb formed by Cys33, Fe3 and Fe4, Cys36. The Cys residues were truncated to ethylthiolate, and the two carbon atoms were kept fixed as an approximation for the upper limit of protein constraint. All other atoms, including the model SAM ligand, where the nucleotide moiety was truncated to an H atom, were optimized at the BP86/TZVP level.[139-141] The electrostatic environment of the

protein matrix was approximated using a water-based polarizable continuum model[142-144] with a reduced ($\varepsilon = 10$) dielectric constant.

Results and Discussion

Fe K-edge X-ray Absorption Spectroscopic

Samples of SP lyase (0.59 mM) were prepared as described above with photoreduction carried out to generate the reduced SP lyase. A second set of samples were prepared utilizing SP lyase (0.67 mM) in which methionine residues were replaced by SeMet; in these samples, reduced methyl viologen was utilized as the reductant. The SeMet-SP lyase samples were utilized in parallel Fe and S K-edge XAS experiments. The substitution of Met with SeMet eliminated the contribution of protein methionines to the S K-edge spectra, thereby enhancing the S K-edge signal from the cluster as will be discussed below. The K-edge spectra were reproducible for independently prepared protein samples and for data collected during different trips to the beamline.

The results of EXAFS analysis for the Fe K-edge spectra of four states (as isolated with and without SAM and reduced with and without SAM) of the anaerobically purified SP lyase are presented in Figure 3.2. Each Fourier transform (FT) of Fe EXAFS data (Figure 3.2B) shows two major peaks in the range of 1.5-3.2 Å, suggesting at least two different Fe-backscatter shells. The major peak at 2.25 Å corresponds to the Fe-S scattering path, where the S originates from both the sulfide and Cys thiolate ligands. The momentum (k) space sampling of up to 15 $Å^{-1}$ and the loss of data quality at around 12.5 $Å^{-1}$ limit the resolution of the two different scattering paths in addition to the Fe-S cluster

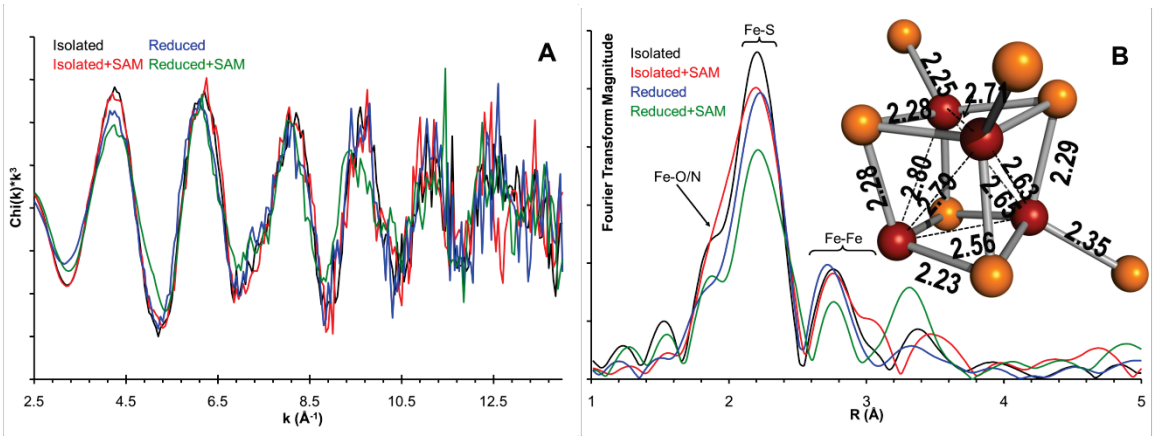

Figure 3.2. Fe K-edge EXAFS of as-purified (black), as-purified in the presence of SAM (red), reduced SP lyase (blue), and reduced SP lyase sample in the presence of SAM (green). (B) FT of the EXAFS spectra shown in (A). (B) Inset: The [4Fe-4S] cluster of HydE (PDB code: 3IIZ) with Fe-S distances at 1.6 Å resolution

inhomogeneity. The as-purified and reduced samples each show a major peak with a maximum intensity at 2.7 Å corresponding to a Fe…Fe scattering path. The as-purified and reduced SP lyase in the presence of SAM has a slightly longer Fe…Fe distance of ~2.74 Å. Furthermore, as-purified SP lyase shows an additional shoulder on the Fe...Fe scattering peak at ~3.0 Å, and the reduced SP lyase shows an additional scattering peak at ~3.3 Å. These features are observed only when SAM is present and only for the more concentrated samples. Modeling of the latter feature of as-purified SP lyase in presence of SAM (Figure 3.3B) suggests that it arises from a longer Fe…Fe scattering path, based on the phase and amplitude comparison of the back-transformed FTIR window as indicated in the lower inset in Figure 3.3A. The alternative back-scatterer assignments (sulfonium S, Se, or C/N/O) did not reproduce the phase information. A similar analysis was performed on reduced SP lyase in the presence of SAM, and indicated the feature arises from a longer Fe…Fe scatter. Fitting results indicated the feature arose from the combination of two Fe…Fe scatters at ~3.0 and ~3.18 Å. Computational modeling (see

below) suggests that the longer Fe…Fe scattering path results from speciation problem with SAM likely binding to two mononuclear Fe sites.

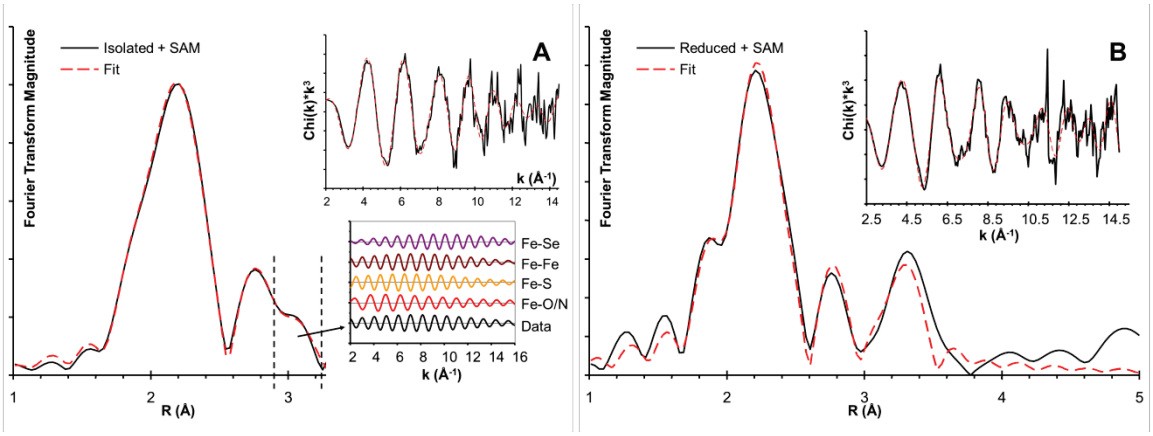

Figure 3.3. Fourier Transform of Fe K-edge EXAFS of as-purified (A) and reduced (B) SP lyase in the presence of SAM with the EXAFS spectra shown as upper insets. The data is shown in black and the fits are in red. The lower inset in (A) shows the backtransformation of R range of 2.9-3.3 Å with models of scattering paths

The other features of the Fe K-edge data are consistent with the results of Mössbauer spectroscopic studies of SP lyase described above. The N/O coordinated Fe^{2+} observed in the Mössbauer spectrum, as well as the peak assigned to Fe…O/N scatterers at around 2.0 Å, is likely due to exogenous iron likely coordinated by the histidine tag of the SP lyase sample. The < 25% contribution from rubredoxin type Fe coordination observed by Mössbauer spectroscopy would show up under the main scattering feature at around 2.25 Å in Figures 2 and 3 and cannot be resolved from iron-sulfur cluster signals in the Fe K-edge data. However, as discussed below, the sulfur K-edge XANES analysis can give complementary information about Fe-S(thiolate) bonding.

The Fe K-edge XANES for as-purified and reduced SP lyase in the absence and presence of SAM are presented in Figure 3.4. The XANES spectra for $FeCl_2$, $FeCl_3$, FeF_2

and FeF_3 are compiled as a reference for the shift in energy position of the rising-edge as a function of effective Fe oxidation states or the iron effective nuclear charge seen by the Fe core 1s electrons.

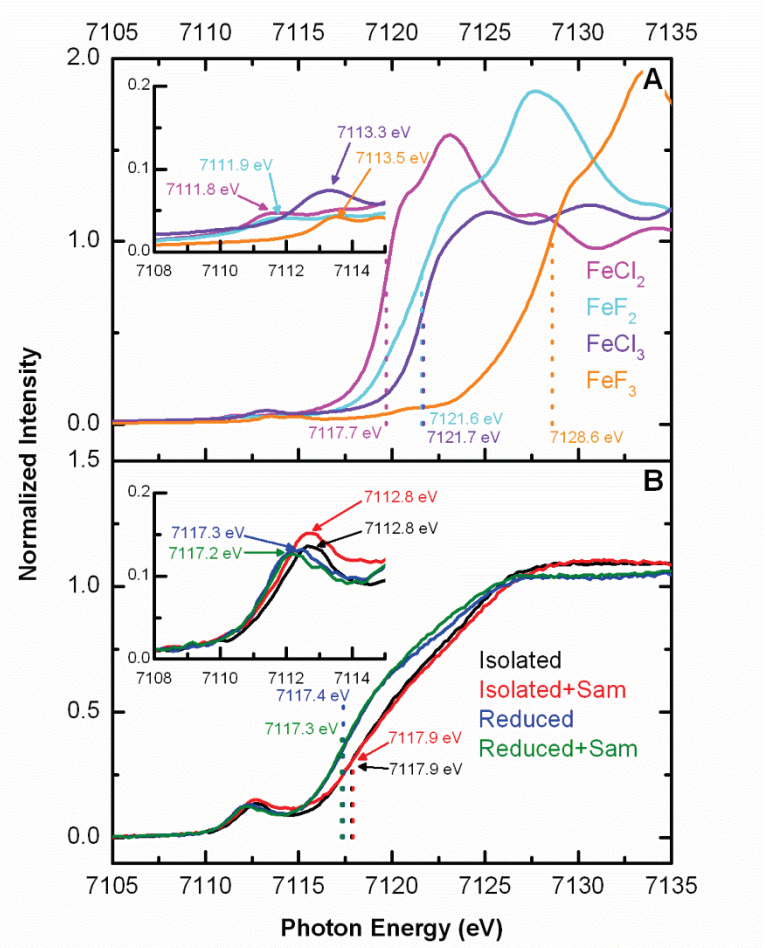

Figure 3.4. Normalized Fe K-edge XANES of $FeCl_2$, $FeCl_3$, FeF_2 and FeF_3 (A) and as-purified and reduced SP lyase in the absence and presence of SAM (B). Samples were prepared using 0.59 mM C.a. SP lyase. SAM was added to a final concentration of 3 mM (Inset: Pre-edge region of Fe K-edge XANES)

The K-edge features are the result of the core 1s → valence np transitions, and therefore are very sensitive to changes in the effective nuclear charge (Z_{eff}). As the redox state and ligand environment of the iron ion changes, the energy position of the edge

shifts due to the change in Z_{eff} of the iron centers. This is well demonstrated by the spectral changes in Figure 3.4A for a series of iron fluoride and chloride compounds. As the oxidation state goes from a formally +2 to +3, the edge positions shift ~3 eV and ~5 eV higher for the chloride and fluoride minerals, respectively. Thus, as the formal oxidation state of the iron increases, the increased ionization energy of the core electron causes a shift of the edge to a higher energy position. Changes in ligand environment can be also observed. Going from chloride to fluoride ligands, the energy position shifts ~2 eV and ~4 eV higher, indicating a change in electron donation for the formally Fe(II) and Fe(III), respectively. Applying the same concepts to the protein samples (Figure 3.4B), the reduction of SP lyase from the $[4Fe\text{-}4S]^{2+}$ to $[4Fe\text{-}4S]^{1+}$ cluster state is accompanied by a shift of ~0.6 eV to lower energy. The energy shift is smaller than in the reference compounds because in the clusters, the change in oxidation state is delocalized over four irons and the sulfur ligands are also involved in the redox process. The slight spectral variations among the oxidized and separately among the reduced SP lyase samples are essentially within the resolution limit of Fe K-edge XAS data. The change in spectral features of the pre-edge is indicative of electronic structure perturbation upon SAM binding that are discussed in more details at the S K-edge XANES analysis.

The pre-edge features are a result of the 1s → 3d quadrupole allowed transitions that gain intensity upon 3d-4p mixing due to the non-centrosymmetric coordination environment.[145, 146] The reference compounds have ligand field splitting that are all close to octahedral coordination geometry with only limited 3d-4p mixing. Thus, the pre-edge intensity is due only to the weak 1s → 3d quadrupole allowed transitions.[145] The higher

intensity pre-edge features of SP lyase are a result of increased 3d-4p mixing of both formally t_2 sets in the tetrahedral environment of the iron centers. The change in the redox state of the iron centers is also well represented by the energy position of the pre-edge features. It is remarkable that upon SAM binding, the pre-edge feature intensities increase slightly (more for the as-purified form). This may be interpreted as resulting from the presence of an overall less symmetric Fe coordination, which is consistent with the presence of a 3:1 site-differentiated cluster.

S K-edge X-ray Absorption Spectroscopic

The sulfur XANES of free ligands are presented in Figure 3.5. The sulfur K-edge spectra of reference inorganic salts Na_2S, NaSH, and $NaSCH_2CH_3$ are shown in Figure 3.5A. The rising-edge region shows a shift in the edge position to higher energies in the order of sodium sulfide, sodium hydrosulfide, and thiolate. As discussed earlier,[147] the positive energy shift is due to increased energy differences between the sulfur 1s and 4p orbitals, which directly indicates an increase in the sulfur effective nuclear charge, $Z_{eff}(S)$, in the same order.

The sulfur K-edge spectra of relevant organic compounds of thiolate, cysteine, and methionine are compared in Figure 3.5B. Cysteine and methionine show similar spectral features as well as similar rising edge energies. Both cysteine and methionine indicate higher $Z_{eff}(S)$ as compared to thiolate, with cysteine demonstrating a slightly higher $Z_{eff}(S)$ than methionine. This energy change is in agreement with the expected inductive effects of an alkyl group. The positively charged SAM displays a characteristic high intensity spectrum due to the presence of three unoccupied C→S σ* orbitals and the

shift in the binding energy of the core 1s electron in comparison to the neutral sulfhydryl group of cysteine (Figure 3.5C). Due to the limited stability of SAM, we have included in Figure 3.5C both the freshly synthesized crystalline solid SAM and its solution spectra. The lower energy feature at around 2472 eV in the solution sample is due to the decomposition of SAM by acid hydrolysis.[106] It is remarkable that the S K-edge XANES provide a close to 5 eV energy range for spectral features of various sulfur ligands (S^{2-}, RS^{-}, RSH/RSR and R_3S^{+}), which all have implications in coordination chemistry of SAM radical enzymes.

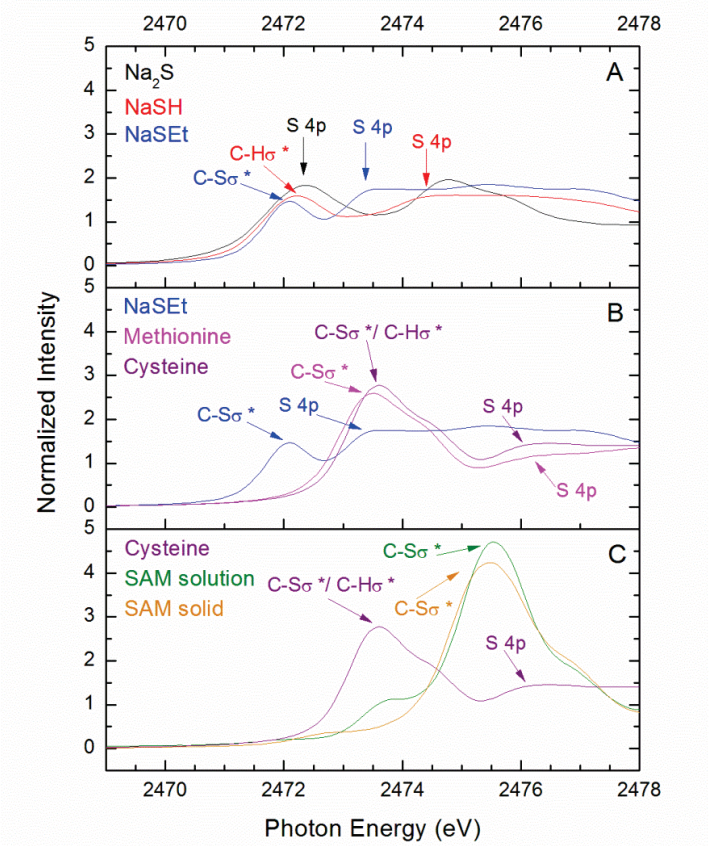

Figure 3.5. S K-edge XANES of free S-ligands (A) Na_2S, NaSH, NaSEt; (B) NaSEt, methionine, cysteine; (C) cysteine, solid and solution SAM(*l*)

The sulfur K-edge XANES for as-purified and reduced SP lyase in the absence and presence of SAM are presented in Figure 3.6. All SP lyase samples were carefully prepared by removing all exogenous sulfur atoms by purifying and dialyzing the SP lyase samples in buffers lacking sulfur atoms and preparing the reduced samples in the absence of dithiothreitol and dithionite. In addition, SP lyase was prepared by overexpressing SP lyase in B834(DE3)pLysS *E. coli* cells growing in SeMet media to remove the contribution of 11 methionine sulfurs that would contribute to the edge-jump and thus reduce the intensity of the pre-edge features of the sulfur K-edge spectra. SP lyase contains four Cys residues, three of which are coordinated to the [4Fe-4S] cluster.

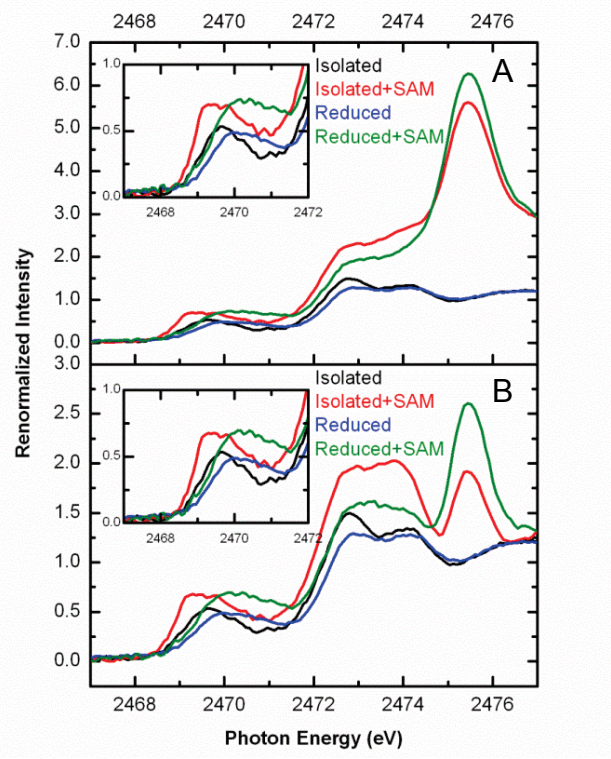

Figure 3.6. Renormalized S K-edge XANES of as-purified and reduced SP lyase in the absence and presence of SAM (A). The renormalized spectra with SAM(solid) subtracted (B). Samples were prepared using 0.49 mM C.a. SP lyase and SAM was added to a final concentration of 3 mM

The total intensity of the pre-edge feature at the ligand K-edge arises from transitions from the ligand 1s core level to the unoccupied metal d-orbitals that are covalently mixed with the ligand p-orbitals. Contributing to this intensity for the samples of SP lyase are transitions from the three thiolates and the four sulfides. SP lyase utilized for these experiments was determined to contain 2.3 (± 0.2) Fe and 2.4 (± 0.2) labile S^{2-} per protein. Due to the mixed cluster states found in SP lyase, pre-edge peaks for sulfide and thiolate contributions are not well resolved. Instead, these features are observed as broad envelopes between 2468 and 2472 eV. Despite the low resolution, we can carry out reasonable fits to the spectra (Figure 3.7) using previously well documented energy positions and fits to the pre-edge features of [2Fe-2S] and [4Fe-4S][148] model complexes.[69, 149]

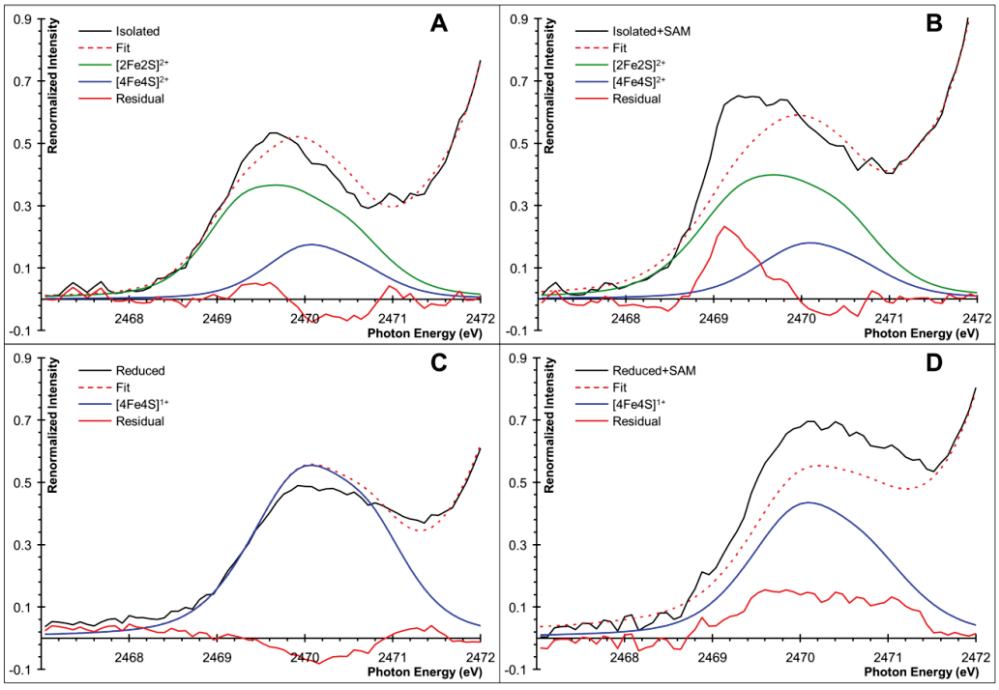

Figure 3.7. Representative fits of the total sulfide and thiolate sulfur contributions to the pre-edge regions for oxidized (A) and reduced (C) SP lyase samples with SAM bound (B and D, respectively)

The oxidized and the reduced forms of the [Fe-S] clusters in SP lyase in the absence of SAM were fit using the S K-edge pre-edge features of structurally well-defined, [2Fe-2S] and [4Fe-4S] model complexes by strictly following the cluster speciation from Mössbauer measurements, similar to the EXAFS analysis of the Fe K-edge spectra. The peak linewidths and positions were allowed to vary within ± 0.3 eV and ± 0.1 eV, respectively. Figures 7A and C show the residuals (red traces) that can be related to the difference of the ligand bonding in the protein bound Fe-S clusters relative to the model complexes. The protein bound Fe-S cluster in the as-purified form shows a slightly increased sulfide character (~2469.5 eV) at the expense of the thiolate character (~2470.5 eV), which can be rationalized by, for example, increased hydrogen bonding interactions involving the thiolates vs. the sulfide ligands. Furthermore, the quantitative comparison of pre-edge intensities of the models and protein bound complex reveals further reduction of the covalency in both the sulfide and thiolate characters of the experimentally probed frontier orbitals. The considerably larger changes for the [2Fe-2S] component are understandable, since the cluster-binding pocket of SP lyase will be incomplete in the case of the [2Fe-2S] cluster and thus allow for solvent molecules to interact with the partially assembled cluster with vacant coordination sites (see computational studies below).

Interestingly in the reduced form, this trend is somewhat reversed as the residual function will be negative more around the sulfide features, indicating that the additional electron added to the cluster will mainly affect the Fe-S(sulfide) bonding. Also it is expected that the more reduced state of the cluster will strengthen the hydrogen bonding

interactions around the cluster. This is further supported by the enhanced reduction between the sulfide and thiolate characters of the reduced synthetic model and the protein bound $[4Fe\text{-}4S]^{+}$ cluster (Table 3.2). Notably the reduced slope of the higher energy side of the pre-edge feature in Figure 3.7C is also consistent with the presence of a rubredoxin type Fe^{2+} coordination environment, since the corresponding pre-edge feature is expected to show up along the rising edge as a shoulder, which would add intensity to the spectrum at around 2471.5 eV.

Addition of SAM to both the as-purified and reduced forms of SP lyase greatly affects the lineshape and intensities of the S K-edge pre-edge features (Figures 7B and D). The more intense pre-edge feature and the lower energy shift of the sulfide features indicate a drastic change relative to the purified form in the absence of SAM. Since most of the spectral intensity for the as-purified samples originates from the [2Fe-2S] cluster, we attribute the spectral change to a change in the coordination environment of the iron sites within this rhomb. As discussed below for computational modeling, it is likely that the SAM can coordinate to one of the Fe sites (Fe2 with Cys29 in the model) of a [2Fe-2S] cluster that is only coordinated with one cysteine. For example, displacement of a cysteine with a less covalent amine or carboxyl ligand can enhance the electron donation from the sulfide to Fe and thus result in an energetically shifted and more intense sulfide feature. The presence of a strongly perturbed coordination environment in the protein bound cluster relative to its synthetic model is also represented by the increased reduction in the sulfide and thiolate spectral features (Table 3.2) relative to the as-purified form without SAM present.

Mössbauer data suggest that the addition of SAM reduces the amount of [4Fe-4S] cluster present in the reduced form of the SP lyase by about 15%. This is expected to give a lower pre-edge intensity (Figure 3.7D) relative to the reduced form in the absence of SAM (Figure 3.7C). The increased amount of rubredoxin-like Fe coordination may explain the intensity increase at around 2471 and 2472 eV for the oxidized and reduced enzyme, but the sulfide feature at around 2470 eV should be lower or at least comparable intensity as in Figure 3.7C. These inconsistencies may be resolved by considering again SAM coordination to incompletely assembled Fe-S clusters or mononuclear Fe sites with thiolate coordination as illustrated below with computational modeling.

Table 3.2. Quantitative break-down of Fe-S composition and sulfide and thiolate covalencies in the SP lyase samples (the percent reduction in area are given relative to the model complexes)

	$[2Fe\text{-}2S]^{2+}$				**$[4Fe\text{-}4S]^{2+}$**			
	Area, eV		**Reduction %**		**Area, eV**		**Reduction %**	
	Sulfide	**Thiolate**	**Sulfide**	**Thiolate**	**Sulfide**	**Thiolate**	**Sulfide**	**Thiolate**
purified	0.57	0.24	38%	41%	0.22	0.07	13%	12%
purified+SAM	0.68	0.31	47%	48%	0.25	0.09	14%	16%
reduced					0.84	0.35	56%	60%
reduced+SAM					0.63	0.31	42%	53%

Potential Energy Surface Mapping of
SAM Interaction with [4Fe-4S] Cluster

In order to obtain additional insights about the generality of the observed elongated Fe…Fe distance within a [4Fe-4S] cluster upon binding SAM, we carried out a density functional theory-based, relaxed potential energy surface mapping study. The unique iron (Fe1)- and shortest sulfide (S)-sulfonium (S^+) distance was systematically varied as graphically summarized in Figure 3.8.

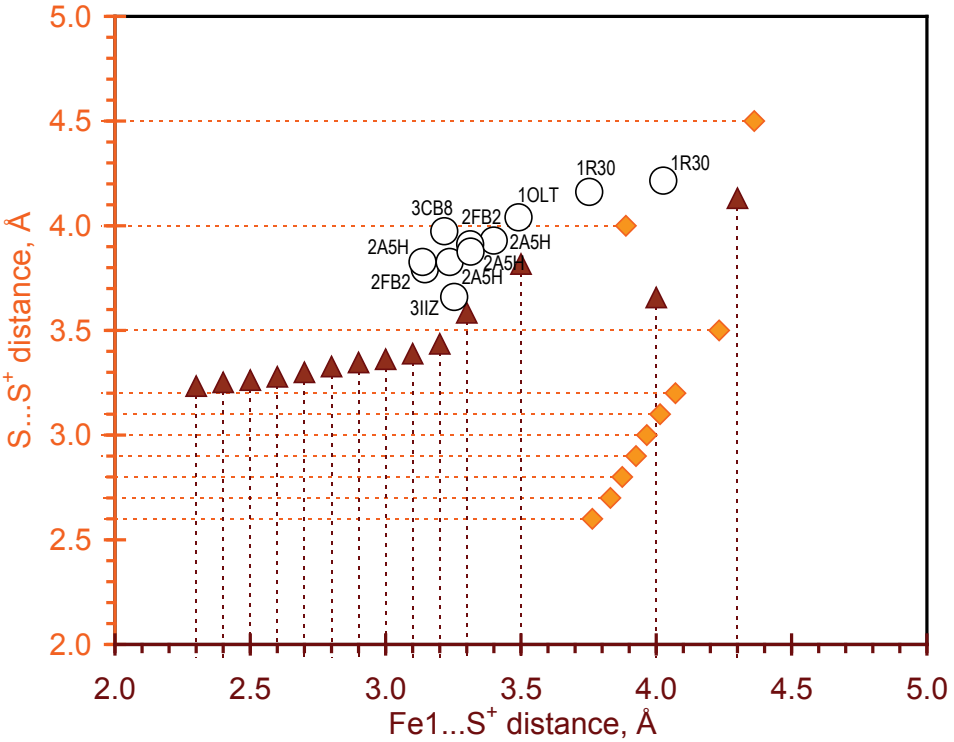

Figure 3.8. Calculated and experimental correlation between Fe1-S^+ and S-S^+ distances as geometric structural descriptors for SAM and [4Fe-4S] interaction (orange diamonds and brown triangles represent corresponding distances when S…S^+ and Fe1…S^+ distances were kept fixed; hollow circles represent experimental data with PDB codes (1OLT[109]; 1R30[19]; 2ASH[113]; 2FB2[111, 112]; 3CB8[115]; 3IIZ[117])

When the Fe1…S^+ distances were driven to greater values (represented by brown triangles), the S…S^+ distance follows a nearly linear trend up to about 3.5 Å, where the constrained longer Fe1…S^+ distances start detaching the SAM ligand from the unique Fe site of the [4Fe-4S] cluster. A similar discontinuity is observed at about the same ~3.5 Å distance when the S…S^+ distance is driven to greater values and everything else is allowed to fully relax. Interestingly, the corresponding distances from experimental structures differ slightly from the optimized structures, indicating the presence of varying magnitudes of protein strain. While the resolution of the crystal structures differs from

3.4 Å (1R30) to 1.62 Å (3IIZ), the overall trend is not expected to be affected by specific resolution limit. Another contribution to the deviation between experimental and calculated data can also be the accuracy of the level of theory and the completeness of the computational model. The BP86/VTZ level of theory has already been shown to give acceptable molecular structures,[138] and the incorporation of a low dielectric environment captures considerable electrostatic effects of the protein environment. The α- and β-carbons were kept fixed in the calculations corresponding to a maximal steric strain imposed by the protein environment to the orientation of the cysteine ligands of the [4Fe-4S] cluster. Thus, the differences between the optimized and experimental distances can be regarded as a first order approximation of how protein environmental effects that were not considered in the computational model may tune the interaction between the [4Fe-4S] cluster and the SAM ligand.

The potential energy diagrams for the constrained Fe1…S^+ and S…S^+ distances are shown in Figure 3.9. As expected from Figure 3.8, the experimental distances of ~3.5 Å fall within the plateau region of a considerably wide range between 3.2 Å and 4.2 Å. This indicates that both Fe1…S^+ and S…S^+ distances can vary within about 1 Å without considerable energy change. It is important to consider with respect to the SAM cleavage mechanism that even the shortest distance of 3.2 Å is too long for a direct orbital overlap-based electron transfer from a reduced [4Fe-4S] cluster into the S^+-C bond. Due to lack of a direct covalent delocalization pathway through the methionine or a direct overlap between the sulfonium S and the [4Fe-4S] cluster at longer than 3.2 Å distances, we propose that the protein environment will likely have a key role in creating an efficient

coupling between the donor and acceptor sites for S-C bond cleavage as well as a gating mechanism to control electron backflow for a catalytic vs. stoichiometric SAM activation and cleavage. Since the potential energy diagrams rise sharply under 3.0 Å distances, the desirable structural modification will require considerable energy for allowing direct orbital overlap and thus efficient electron transfer from the reduced [4Fe-4S] cluster into the specific C-S σ* orbital of the sulfonium moiety.

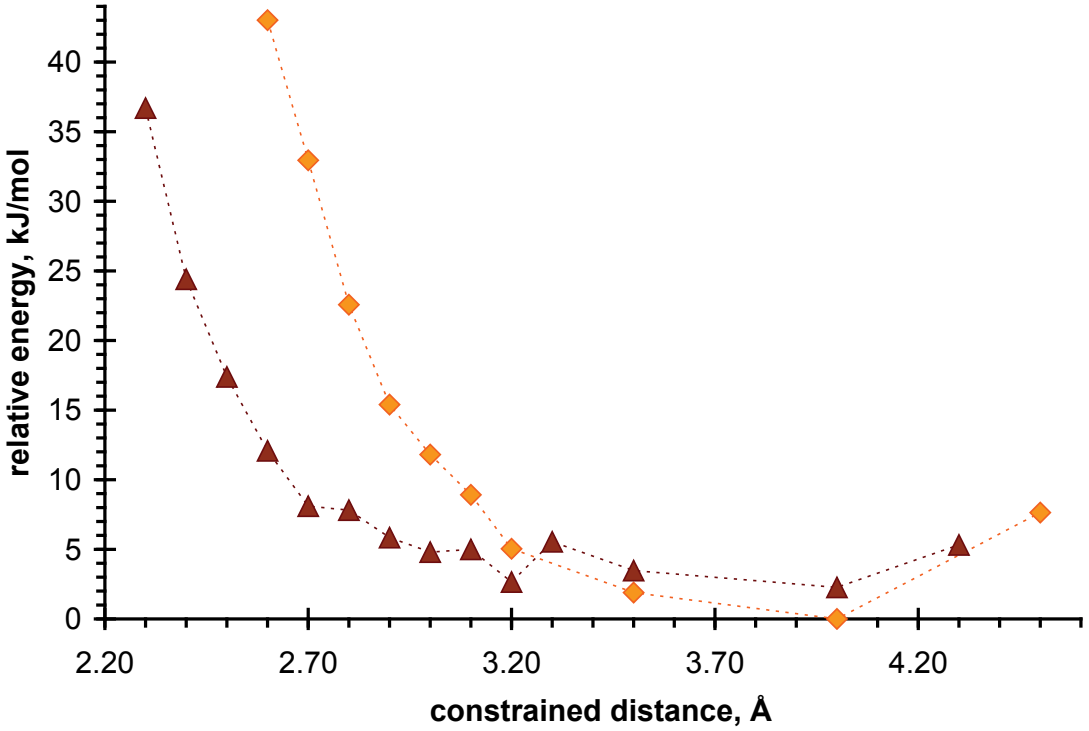

Figure 3.9. Potential energy curves for constrained Fe1…S^+ (brown triangles) and S…S^+ (orange diamonds)

Relevant to the interpretation of our EXAFS data, we evaluated the difference between the Fe…Fe distances along these coordinates. We compared and contrasted the deviations between Fe…Fe distances within the ferromagnetically coupled and between

the antiferromagnetically coupled [2Fe-2S] rhombs (see inset in Figure 3.10). In order to obtain the ground state electronic structure for the [4Fe-4S] cluster, a systematic analysis of all possible magnetic coupling schemes was carried out. It was determined that the top M_s = +9/2 [Fe1Fe5-2S] rhomb prefers to be antiferromagnetically coupled to the bottom M_s = −9/2 [Fe6Fe7-2S] rhomb, regardless of the nature of the ligand at the site differentiated Fe site (Fe1). Figure 3.10 indicates that there is more than 0.05 Å difference between the Fe…Fe distances within and close to 0.1 Å difference between the two ferromagnetically coupled [2Fe-2S] rhombs. These differences in Fe…Fe distances are large enough to be experimentally detectable through EXAFS analysis even when the mixture of composition in Fe-S cluster states are taken into account. Remarkably, as the SAM ligand approaches the [4Fe-4S] cluster, the magnitude of distortion in the Fe…Fe distances of the rhombs increases exponentially.

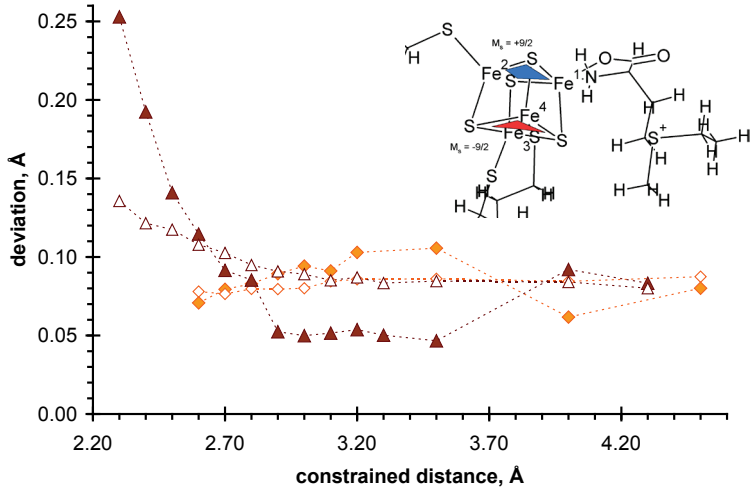

Figure 3.10. Deviation between Fe…Fe distances within ferromagnetically (solid symbols) and between antiferromagnetically (hollow symbols) coupled [2Fe-2S] rhombs as a function of constrained Fe1…S^+ (brown triangles) and S…S^+ (orange diamonds) distances

Computational Modeling of SAM Interactions
with Fe-S Cluster as a Function Speciation

In order to gain further insights into the interpretation of the EXAFS spectra and the chemical adequacy of the fits, we carried out additional computational modeling by considering the oxidized and reduced states of the [4Fe-4S] and [2Fe-2S] clusters in the presence and absence of SAM as a ligand. The comprehensive summary of the EXAFS fits and the corresponding calculated structural parameters are shown in Table 3.3.

All experimental data shown in the first rows for each sample in Table 3.3 were obtained using the speciation information from the interpretation of Mössbauer data. The composition of the as-purified form of the SP lyase samples was identified to be dominantly [2Fe-2S] cluster (45%, Table 3.1) and [4Fe-4S] with about a 3:1 ratio. The mononuclear Fe content was comparable to the amount of the [2Fe-2S] cluster. Thus, the observed spectral features both in the Fe K-edge EXAFS and the S K-edge XANES will dominantly originate from either the mononuclear Fe site or the binuclear Fe cluster. The average Fe…Fe distance from EXAFS analysis appears to be about 0.08 Å longer than the calculated distance, while the Fe-S^s and Fe-S^t distances are remarkably close to their experimental values. The Fe-O/N distance shows an even a larger deviation between experiment and theory, indicating that the computational models do not capture this bonding acceptably well. Coordination of mononuclear Fe (up to 40%, Table 3.1) likely to the histidine tag may be a better explanation for the short distance relative to the calculated values.

As discussed above, addition of SAM to the as-purified SP lyase sample does not change the speciation significantly; however, a new feature appears at around 3 Å for the

Table 3.3. Summary of experimental and calculated Fe-S and Fe-O/N distances from EXAFS analysis (see above) and DFT calculations (average distances are given in Å, and n refers to coordination number or redundancy parameter in EXAFS fits; all calculations were completed with protein constraints on the Cys ligands from the pyruvate formate lyase crystal structure 3CF8) [150]

sample		Fe…Fe	n	Fe-S^s	n	Fe…S^s	n	Fe-S^t	n	Fe…S^t	n	Fe-O/N	n
as-purified	EXAFS	2.72	1.0	2.19	1.5			2.30	1.5			1.92	0.5
	2 Fe(III)	5.07	1.0					2.31	1.5	4.39	1.0	2.00	2.5
										6.03	0.5		
	$[2Fe\text{-}2S]^{2+}$	2.64	1.0	2.22	2.0			2.30	1.5	4.47	1.5	2.17	0.5
	$[4Fe\text{-}4S]^{2+}$	2.65	3.0	2.22	1.0	3.87	1.0	2.25	0.75	4.68	2.3	2.08	0.5
		max:2.70		2.32	2.0								
as-purified with SAM	EXAFS	2.75	0.5	2.20	2.0			2.25	1.5			1.93	0.5
		3.01	0.5										
	2 Fe(III)	3.59	0.5					2.31	1.5	3.82	1.0	2.06	3.0
										5.77	0.5		
	$[2Fe\text{-}2S^{(S,N)}]^{2+}$	2.69	0.5	2.23	2.0			2.31	1.5	4.53	1.5	2.17	0.5
	$[2Fe\text{-}2S^{(S,N,O)}]^{2+}$	2.71	0.5	2.27	2.0			2.32	1.5	4.47	1.5	2.23	0.5
	$[2Fe\text{-}2S^{(N,O)}]^{2+}$	2.47	0.5	2.28	2.0			2.35	1.5	4.69	0.5	2.12	0.5
	$[4Fe\text{-}4S]^{2+}$	2.72	3.0	2.23	1.0	3.90	1.0	2.27	0.75	4.72	2.3	2.19	0.5
		max:2.79		2.33	2.0								
reduced	EXAFS	2.72	2.0	2.23	2.5			2.29	1.0			1.94	0.75
	Fe(II) + Fe(III)	4.65	0.5					2.31	1.5	4.43	1.0	2.02	2.5
										5.50	0.5		
	2 Fe(II)	4.32	0.5					2.36	1.5	4.53	1.0	2.05	2.5
										4.86	0.5		
	$[4Fe\text{-}4S]^{1+}$	2.64	3.0	2.26	1.0	3.88	1.0	2.28	0.75	4.70	2.3	2.17	0.25
		max:2.70		2.33	2.0								
reduced with SAM	EXAFS	2.78	1.0	2.25	3.0			2.24	0.75			1.91	0.5
		3.00	1.0										
		3.18	1.0										
	Fe(II) + Fe(III)	3.62	0.5					2.35	1.5	4.02	1.0	2.09	3.0
										5.64	0.5		
	2 Fe(II)	3.10	0.5					2.25	1.5	3.70	1.0	2.08	3.0
										5.02	0.5		
	$[4Fe\text{-}4S]^{1+}$	2.71	3.0	2.27	1.0	3.92	1.0	2.29	0.75	4.75	2.3	2.25	0.5
		max:2.76		2.34	2.0								

Fe…Fe scatterers that is absent for the sample without SAM. We evaluated the structural possibility of SAM coordination to a partially assembled [2Fe-2S] cluster bound in the [4Fe-4S] active site pocket. The calculation clearly indicates that the elongated Fe…Fe distance cannot be due to the [2Fe-2S] cluster since the longest Fe…Fe distance was observed for the [2Fe-2S] cluster with bidentate SAM coordination at an Fe site with a single Cys ligand ($[2Fe\text{-}2S^{(S,N,O)}]^{2+}$ row in Table 3.3). The longest Fe…Fe scatterer in the bidentate coordinated SAM at the unique Fe site of an oxidized [4Fe-4S] cluster approximates within 0.2 Å of the experimental 3 Å. As discussed above, an increased protein strain effect that packs the SAM closer to the [4Fe-4S] cluster than what we were able to model from the structure of the model pyruvate formate lyase enzyme's SAM binding site could account for the elongation. Similar to the as-purified form of SP lyase without SAM, the calculated and experimental Fe-S distances are in good agreement, while the Fe-O/N distance was calculated to be too long relative to the average EXAFS value. We have also evaluated the possibility of some of the spectral features originating from mononuclear Fe sites within the SAM cluster binding pocket where one of the sites were coordinated with Cys and three water molecules and the other with two Cys and two water molecules. The constraints on the Cys residue positions were maintained as in all other calculations. These define a very tight binding cavity and additional water ligands would have been pushed into the first solvation shell and thus not considered. The considerable reduction of the Fe…Fe distance by 1.5 Å is due to the bridging carboxyl oxygen (O^x) of the SAM, which brings the two Fe sites together, while the amine group of SAM makes the coordination environment of the two Fe sites approximately similar

([ONSSO^{x}] vs. [O^{x}OOSS]). The 3.59 Å is now too long to be considered as a plausible source of the longer Fe…Fe scatterer, especially keeping in mind that most of the simulated Fe…Fe scatterer distances were too short relative to their EXAFS values.

The speciation problem for the reduced SP lyase samples is less convoluted due to the absence of additional Fe-S clusters other than the expected [4Fe-4S]. However, we had to also consider the presence of mononuclear Fe sites due to their considerable concentration (40%) in the sample without SAM that increased by about 15% if SAM was present. The EXAFS data interpretation and the calculated geometric data for the sample without SAM follows the same trends as discussed above for the oxidized form. Interestingly, addition of SAM not only alters the speciation by converting about 15% of the [4Fe-4S] cluster to mononuclear Fe sites (Table 3.1), but also results in the appearance another Fe…Fe scatterer at much longer distance (3.18 Å). By looking at the computational results (Table 3.3), we can actually reasonably well assign this to originate from two mononuclear Fe sites in the SAM cluster binding pocket that are bridged with a SAM (3.18 Å experimental and 3.10 Å calculated) in addition to the elongated Fe…Fe distance of the [4Fe-4S] cluster.

Conclusion

X-ray absorption spectroscopy is a powerful tool to investigate the geometric and electronic structure of the bound [Fe-S] clusters. When combined with Mössbauer spectroscopy, giving the speciation cluster states especially for those states that are inaccessible by EPR spectroscopy, more complete information can be obtained from the

Fe and S K-edge XAS regarding the geometric and electronic structure of the bound [Fe-S] cluster. We described here the use of these complementary approaches to provide the first structural description of the nature of the iron-sulfur cluster of SP lyase and its interaction with SAM.

Ideally SP lyase should contain 4 irons and 4 sulfides per monomer. The observation that SP lyase purifies with less than four iron and sulfide ions per monomer indicates substoichiometric incorporation of the [4Fe-4S] cluster. Therefore, when studied by spectroscopy, the presence of additional iron-sulfur clusters and even cysteine coordinated, mononuclear iron centers need to be considered at the SAM cluster binding pocket.

Mössbauer analysis has provided a quantitative picture of the mixture of cluster states present in the as-purified SP lyase, and the conversion of these to primarily [4Fe-4S] clusters upon reduction. Reductive cluster conversions from $[3Fe\text{-}4S]^{1+}$ and $[2Fe\text{-}2S]^{1+}$ states to $[4Fe\text{-}4S]^{2+/1+}$ have previously been reported for several radical SAM enzymes including biotin synthase,[151-153] lipoyl synthase,[154, 155] lysine 2,3-aminomutase, [156, 157] and the activating enzymes of pyruvate formate lyase,[158-161] and anaerobic ribonucleotide reductase,[162] although the physiological relevance of these cluster conversions remain unknown. As-purified SP lyase was found to contain 40% $[2Fe\text{-}2S]^{2+}$ clusters and 15% $[4Fe\text{-}4S]^{2+}$ clusters. The remaining 45% of iron was attributed to adventitiously bound ferric species. The addition of the cofactor SAM did not appear to have an effect on the cluster states of the as-purified enzyme as revealed in the Mössbauer data. Due to the considerable amount of mononuclear Fe, and [2Fe-2S] cluster

content, in our XAS analysis, we had to consider the physiologically non-relevant but chemically plausible SAM coordination to these sites. Reduced SP lyase was estimated to contain 60% $[4Fe\text{-}4S]^{1+}$ clusters as well as contributions from high-spin Fe^{2+} species (10% N/O coordinated Fe^{2+} and 15% FeS_4 species) and fast relaxing Fe^{3+} (15%). Upon adding SAM to the reduced SP lyase, it appears there may be some non-productive SAM cleavage as a 15% loss of the $[4Fe\text{-}4S]^{1+}$ state is observed as compared to the reduced spectrum. Due to the about 5-fold excess of SAM, here we also considered the chemically plausible coordination of SAM to mononuclear Fe sites at the SAM cluster binding pocket. According to the Mössbauer analysis, the [4Fe-4S] cluster is mostly converted to the fast relaxing ferric species, although 5% of this spectrum could not be identified. This appears to be a more complex change than conversion to a $[4Fe\text{-}4S]^{2+}$ state, as expected if SAM cleavage was occurring under physiological conditions.

Previous spectroscopic studies on radical SAM enzymes have provided a wealth of information regarding the requirement of SAM in radical catalysis. Mössbauer studies on pyruvate formate-lyase activating enzyme (PFL-AE) presented evidence for the interaction of SAM with the unique iron in the [4Fe-4S] cluster of the enzyme.[159] Electron nuclear double resonance (ENDOR) spectroscopy of PFL-AE then revealed the direct ligation of SAM to the unique iron of the cluster via the carboxyl and amino groups of the methionine moiety of SAM.[106, 107] Resonance Raman, Mössbauer and EPR spectroscopic studies also provided evidence for the interaction of SAM with the unique iron of the $[4Fe\text{-}4S]^{2+}$ cluster of biotin synthase (BioB).[163]

Conversely, a Se XAS study of lysine 2,3-aminomutase (LAM) proposed an interaction between the sulfonium ion and an Fe atom of the [4Fe-4S] cluster.[164] This interaction was deduced from EXAFS analysis of a feature at 2.7 Å, which was attributed to the interaction of the Se of SeMet (a cleavage product of Se-SAM) with a cluster Fe atom when $[4Fe\text{-}4S]^{2+}$ LAM was incubated with Se-SAM, dithionite, and the substrate analog *trans*-3,4-dihydrolysine.[164] However, this feature was not observed when Se XAS studies were performed with Se-SAM and PFL-AE or BioB.[165] This led to the suggestion that this interaction may be specific to the enzymes that utilize SAM as a cofactor rather than as a substrate, since it is not a general property of radical SAM enzymes. Our computational analysis of the potential energy surface of SAM interaction with the [4Fe-4S] cluster revealed a critical range of 2.7-3.2 Å for the distance between the unique iron site and the sulfonium sulfur that indirectly correlate with the above hypothesis. Because these enzymes reform SAM during catalysis, the cleavage products of SAM must remain in the active site and therefore may result in a different binding mode of SAM to the enzyme. It is important to mention that a recent study by Nicolet et al.[117] suggests the role of SAM is determined by the relative affinity of the enzyme for [dAdo + Met] and SAM and not by the cleavage mechanism itself. Consequently, one of the interests of this work was to investigate the interaction of SAM with the cluster of SP lyase.

Our EXAFS results demonstrate the emergence of a new feature at ~3.0 Å as a shoulder on the Fe...Fe scattering feature when SAM is added to both the as-purified as well as the reduced enzyme. This feature is only observed when SAM is present and stays present if the windowing, k-range parameters of EXAFS data analysis are varied. This

shoulder feature fits well with an elongated Fe...Fe scatterer of 3.0 Å relative to the expected average Fe…Fe distance (2.72 Å) for a classical [4Fe-4S] cluster with tetrathiolate coordination. This observation indicates a longer Fe...Fe distance upon SAM binding to the cluster, and the intensity suggests this feature is due to around two of the Fe…Fe distances becoming elongated in the cluster. It appears the [4Fe-4S] cluster becomes distorted upon SAM ligating the unique iron of the cluster with some Fe...Fe bond distances lengthening due to this interaction. Our computational potential energy surface mapping study also indicated the distortion of the [4Fe-4S] cluster as a function of SAM…[4Fe-4S] cluster distance. It is important to emphasize that this structural distortion deviates from the changes expected from the stoichiometric 3:1 site differentiation. Upon SAM coordination, the Fe…Fe distance within the ferromagnetically coupled, M_s = +9/2 [2Fe-2S] rhomb containing the site-differentiated Fe site that is not coordinated by a Cys residue becomes considerably longer relative to the other M_s = −9/2 rhomb by about 0.1 Å at 2.7 Å of SAM…[4Fe-4S] cluster separation. This increases up to 0.2 Å at around 2.4 Å separation, and drops to 0.05 Å above 3 Å. Parallel, the two other Fe…Fe distances involving the unique Fe site also being elongated relative to the other Fe…Fe distances by about the same magnitude (0.12-0.09 Å) along the antiferromagnetic interaction between the two ferromagnetically coupled rhombs. Thus, the SAM coordinated cluster structurally is better described as a 2:2 site-differentiated cluster.

To determine if this observation is shared by other members of the radical SAM superfamily, we compared and contrasted the Fe...Fe bond distances of the [4Fe-4S]

radical cluster in the crystal structures solved for members of this superfamily. Of the handful of structures solved for this superfamily [Reference back to the list as in Figure 3.8], only one (MoaA, resolution 2.8 Å) does not have SAM (or a cleavage product of SAM) bound to the radical [4Fe-4S] cluster, making it difficult to determine the geometry of the cluster of the other radical SAM enzymes when the unique Fe atom is not coordinated. However, from all of the available radical SAM crystal structures containing a [4Fe-4S] cluster (resolution range of 1.25 to 2.8 Å), it is apparent that the average Fe...Fe bond lengths are longer (~ 0.07 – 0.25 Å) for the unique Fe when ligated by SAM than for the other cysteine bound Fe atoms in the cluster, resulting in a slightly distorted cluster structure. The difference between the average bond lengths for the unique Fe atom and the protein bound Fe atoms in LAM[113] (resolution 2.1 Å) are less at 0.007 Å, while HemN[109] (resolution 2.07 Å) is the only structure to not follow this general observation. Interestingly, both of these structures contain [4Fe-4S] clusters with significantly shorter (0.14 – 0.32 Å) Fe...Fe distances as compared to the other structures.

MoaA is the only radical SAM enzyme that has structures solved for both the SAM-bound and unbound forms of the enzyme in 2.2 and 2.8 Å resolution, respectively. While the coordinatively unsaturated, unique Fe atom has slightly longer average Fe...Fe distances than the average protein bound Fe atoms (by 0.03 – 0.05 Å), this distance is increased upon SAM ligation (0.07 – 0.22 Å). The distortion of the [4Fe-4S] cluster upon SAM binding observed in MoaA suggests that the elongated Fe…Fe distances are attributable to SAM ligating the unique Fe of the cluster. Specifically, the Fe3…Fe4 distance increases by 0.16 Å and 0.22 Å for the two clusters in the protein dimer. The

Fe2…Fe4 distance also increases for each cluster of the dimer by 0.09 Å and 0.07 Å (for clusters A and B, respectively). The changes in the clusters upon SAM binding MoaA are presented in Table 3.4. The observation that two of the Fe...Fe distances become elongated upon SAM binding agrees with our EXAFS. The Fe3…Fe4 distance of the SAM-bound PFL-AE structure is also elongated at 2.88 Å as compared to the other distances in the structure,[115] while the HydE SAM-bound structure appears to have 3 elongated Fe…Fe distances for the unique Fe[117] (Table 3.4).

Table 3.4. Variation of Fe…Fe distances in MoaA (1TV7 at resolution 2.8 Å) upon SAM binding (1TV8 at resolution 2.2 Å). Distances are given in Å. Cluster numbering as in PDB code 3CIW with the unique Fe being Fe4

Enzyme	MoaA	MoaA+SAM	Difference	MoaA	MoaA+SAM	Difference
Cluster	A	A		B	B	
Fe1…Fe2	2.71	2.71	0.00	2.72	2.80	0.08
Fe2…Fe3	2.63	2.63	0.00	2.66	2.47	-0.19
Fe3…Fe4	2.56	2.72	0.16	2.62	2.84	0.22
Fe4…Fe1	2.80	2.74	-0.06	2.76	2.82	0.06
Fe1…Fe3	2.65	2.69	0.04	2.66	2.50	-0.16
Fe2…Fe4	2.79	2.88	0.09	2.76	2.83	0.07

A similar observation was made for aconitase when the unique Fe atom in the [4Fe-4S] cluster is ligated by citrate.[166] In the coordinatively unsaturated form, the average Fe...Fe distances for the unique Fe atom are ~ 0.01 Å shorter than the protein bound Fe atoms.[167] However, upon ligation by citrate, the average Fe...Fe distances for the unique Fe atom are 0.2 Å longer than the average Fe...Fe distances for the protein bound Fe atoms, suggesting a slight distortion of the [4Fe-4S] cluster. Several of the Fe...Fe distances increase in the S642A aconitase crystal structure in the presence of the citrate substrate. The Fe1…Fe2 distance increases by 0.17 Å, Fe3…Fe4 increases by 0.18

Å, the Fe4…Fe1 distance increases by 0.23 Å and the Fe2…Fe4 distance increases by a remarkable 0.38 Å.

The Fe K-edge XANES in Figure 3.4 shows two oxidation states for the as-purified and reduced samples as clearly observed from the different rising edge energy positions. The higher intensity of the pre-edge feature for as-purified in the presence of SAM may also indicate the distortion of the [4Fe-4S] cluster upon interacting with SAM as pre-edge features gain intensity when the symmetry is reduced, and thus Fe 4p orbitals are allowed to mix with Fe 3d orbitals. A noteworthy observation of the spectra is the small differences in the spectral features between the reduced sample and the reduced sample in the presence of SAM. EPR spectroscopy of the reduced enzyme in the presence of SAM shows a broadened $[4Fe\text{-}4S]^{1+}$ signal with a striking decrease in intensity.[124, 127] Previous studies have suggested that the decreased EPR intensity is due to non-productive SAM cleavage, indicating that SAM is reductively cleaved by the $[4Fe\text{-}4S]^{1+}$ cluster to produce methionine, 5'deoxyadenosine and a $[4Fe\text{-}4S]^{2+}$ cluster without turnover of substrate to product occurring.[118] However, a recent study demonstrated little dAdo production in the absence of dithionite and substrate, as is the case in these samples.[127] The spectra presented in Figure 3.4 support that there is no apparent oxidation of the cluster upon the addition of SAM to the reduced enzyme. In fact, the addition of SAM shifts the features of the rising edge to slightly lower energy, away from the oxidized spectra of the as-purified SP lyase samples. This parallels our previous observations that the interaction of SAM with the $[4Fe\text{-}4S]^{1+}$ cluster of SP lyase does not immediately trigger SAM cleavage and the accompanied oxidation of the cluster.[127]

The sulfur K-edge spectra of free ligands (Figure 3.5) demonstrate a shift in energy of the edge position to higher energies, directly indicating an increase in the sulfur effective nuclear charge (Z_{eff}). The Na_2S, NaSH and NaSEt compounds show shifts in the rising-edge region to lower energy values due to lower Z_{eff} as compared to methionine and cysteine. Methionine and cysteine display similar spectral features as well as similar rising edge energies. SAM displays a high intensity feature ~ 2475.5 eV due to 3 C-S σ* interactions as well as a large shift of the rising edge feature to higher energy due to the higher Z_{eff} of the S 1s of the sulfonium ion. The lower energy shoulder just below 2474 eV in the SAM spectrum is due to a partially decomposed state due to acid catalyzed hydrolysis giving 5'methylthioadenosine (MTA).

A straightforward evaluation of the S K-edge XAS spectra for anaerobically purified SP lyase (Figure 3.6) was limited by the presence of a mixture of cluster states as quantified from Mössbauer spectroscopy. However, combining the biochemical and analytical measurements on iron and sulfide loading, protein concentrations, and known amount of SAM excess allowed us to extract electronic structural information from the data. Using reference spectroscopic data from the literature of structurally well-defined iron-sulfur biomimetic compounds and speciation information from Mössbauer measurements, we obtained an initial estimate for the reduction of Fe-S bond covalencies for the protein bound iron-sulfur clusters. On the basis of fitting the spectral features due to the presence of Fe-S^{s-} and Fe-S^{t}(Cys) bonds, we see on average about 40% reduction of sulfur electron donation in the [2Fe-2S] clusters, considerably smaller (~15%) in the [4Fe-4S] clusters, and remarkably larger (50-60%) when the reduced forms of SP lyase

are considered. These changes are chemically reasonable since a reduced form of the cluster is expected to show stronger hydrogen bonding interactions due to the increased overall electron density. Also, the partially assembled [2Fe-2S] cluster in the SAM cluster binding pocket will likely have considerable solvent interaction and potentially small molecule/ion binding due to the lack of at least an additional two Fe ions and two S ions. Even the about ~15% reduction of Fe-S bond covalency can be related to a considerable number of hydrogen bonds or dipole interactions involving both the sulfides and the thiolate sulfurs. Upon SAM binding, the spectral features change drastically, indicating the formation of a rather different Fe coordination environment than in the as-purified or reduced forms of the [Fe-S] clusters without SAM present. The most striking spectral difference was observed for the SAM binding to the as-purified or oxidized form, where both the Fe-sulfide and thiolate bond covalencies increase. We were able to rationalize this by considering the large structural changes for a [2Fe-2S] cluster when SAM coordinates. While this is physiologically non-relevant, it is a remarkable perturbation that we were able to detect experimentally. The coordination of the SAM to the oxidized form of the [4Fe-4S] clusters appear to have minimal effect; however, we see a reversed trend for the reduced [4Fe-4S] cluster upon SAM coordination as both the sulfide and the thiolate bond covalencies decrease. The considerably large change in the sulfide may be rationalized by the reorganization of the enzyme's SAM cluster binding pocket; as the large and bulky SAM cofactor binds to the Fe site, the pocket becomes more crowded and considerable protein strain may be induced as seen indirectly from the

distortion of the [4Fe-4S] cluster geometry. This in turn may packs the cluster closer to nearby dipoles or shorten H-bonds, thus resulting in reduced Fe-S donation.

Overall the combined spectroscopic analysis of anaerobically purified SP lyase indicates that the specific interaction of the Fe-S cluster of SP lyase with its cofactor SAM as observed by EPR is not due to non-productive SAM cleavage and formation of a $[4Fe\text{-}4S]^{2+}$ cluster. The interaction between the cluster and SAM appears to produce a slight distortion of the cluster with some of the Fe...Fe distances increasing. This observation may extend to other members of the radical SAM superfamily and can be critical for reducing the cluster or initiating radical catalysis. Complementary computational studies indicate the role of the protein environment in tuning the relative position of the redox active cluster and the SAM substrate. An increased protein strain pushing the SAM closer to the [4Fe-4S] cluster would facilitate a rapid electron transfer from the cluster into the sulfonium-C bond, which upon cleavage may eliminate this strain and practically provide a gating mechanism to prevent the electron back-transfer. The preservation of protein strain would allow for stabilization of the radical/oxidized [4Fe-4S] pair relative to the sulfonium/reduced [4Fe-4S] reaction partners and thus allow for catalytic processes to take place.

CHAPTER 4

NANOPARTICLES

Introduction

Nanometer scale materials have been the focus of extensive studies in the past decade. Due to their unique optical, electronic, magnetic, and chemical properties respective to the analogues bulk counterparts, a wide range of research has been done in the area of environmental and biological application such as biosensor,[168] diagnostics,[169] catalysis,[170, 171] and pollution.[47] These properties strongly depend on size, shape, structure, and composition.[172] As a result, part of the past research has focused on controlling the synthesis of nanometer scale materials.

Nanometer scale iron-sulfur systems have become a center of growing scientific interest due to importance in hydrothermal vents,[46] pollution,[47] cancer treatments,[48] and catalytic applications.[49, 50] A simple, controlled synthesis of nanometer scale iron-sulfur systems has proven to be challenging. Thus, the structural and electronic properties of the nanometer scale iron-sulfur systems are still ill-defined. A variety of approaches have been employed to synthesize nanometer scale iron-sulfur particles.[51-53] Another novel approach is with protein cage architectures including ferritin and ferritin-like proteins. This allows for various size-constrained reaction environments to control particle growth. In addition to size, temperature, pH, and Fe^{II} loading ratio can be used to control the iron-sulfur particle formation.[8]

In this study, we investigated the iron-sulfur particle synthesized in ferritin to determine oxidation state with respect to bulk and synthesized minerals using X-ray absorption spectroscopy. An earlier study[8] indicated that the nanometer scale iron-sulfur particles can be described as Fe(III) sulfide with local structure similar to protein bond iron-sulfur clusters. In order to inquire into how minerals and molecular iron-sulfur clusters relate to nanometer scale particles, we begin to investigate an ambitiously large parameter space with respect to chemical synthesis, composition, size, structure, as well as experimental detection method, beamline, and absorption edge. The current XAS data set is somewhat limited, and spectra are still missing to complete the work for scientific publication. Therefore, this chapter is written more as a progress report than a finished technical paper. Although this study is still a work in progress, it taught us important aspects about the aging of the precipitates and also of data collection and analysis that prepared us for two more complete stories described in Chapter 5 and 6.

Materials and Methods

The ferric sulfides prepared for this study were formed by the reaction of stoichiometric quantities of $FeCl_3$ and Na_2S in degassed, anaerobic aqueous solutions at room temperature under an atmosphere of N_2. The black precipitate was rinsed with degassed, anaerobic water until there was no detectable chloride by reacting the filtrate with silver nitrate. The sample was dried under vacuum. The ferrous sulfide was formed similarly to the ferric sulfide except with the $FeCl_2$ as the iron source. The nanometer

scale particles grown in ferritin protein cages were supplied by the Douglas lab, and details of the synthesis have been previously published.[8, 59, 173, 174]

The X-ray absorption measurements were collected at Stanford Synchrotron Radiation Lightsource (SSRL) under storage ring (SPEAR3) condition of 3 GeV and current of 80-200 mA. The iron K-edge XANES were collected on the 20-pole, 2 T Wiggler beamline 7-3 (BL7-3) and 1.3 T bend magnet beamline 2-3 (BL2-3), both equipped with a Si(220) downward reflecting, double-crystal monochromator. Data was collected in transmission mode with an ionization chamber before and after the sample. The energy was calibrated using the first peak of the first derivative of an iron foil assigned to 7111.2 eV. During the measurement, the sample was placed in a liquid helium cryostat and maintained at a constant temperature of ~10 K. The beamline parameters were optimized at 8000 eV.

The sulfur K-edge XANES was collected on a 56-pole, 0.9 T Wiggler beamline 6-2 (BL6-2) and a 20-pole, 2.0 T Wiggler beamline 4-3 (BL4-3), both equipped with a liquid nitrogen-cooled, Si(111) double-crystal monochromator. XAS measurements were collected in the energy range of 2450–2740 eV using an unfocused beam in a He-purged beam path at room temperature with a multi-element Lytle fluorescence. Samples were mounted on a sample paddle at 45º to the incident beam and Lytle fluorescence detector solids, which were prepared in a glove box, were diluted with boron nitride and ground together to minimize self-absorption and then mounted onto a sulfur-free kapton tape. These samples, while not extremely air sensitive, were protected from oxidation and moisture during sample mounting by a thin polypropylene window. The beamline

parameters were optimized at 2740 eV. The incident photon energy was calibrated to the spectra of $Na_2S_2O_3 \cdot 5H_2O$ with a maximum pre-edge feature at 2472.02 eV.

The iron L-edge XANES was collected on a 30-pole, 1.45 T Wiggler beamline 10-1 (BL10-1) and a bend magnet beamline 8-2 (BL8-2) both equipped with a 6 m spherical grating monochromator set to 1000 lines/mm. Spectra were collected in the energy range of 660–800 eV using an unfocused beam in ultrahigh vacuum (UHV). The beamline was optimized at 715 eV. Fe_2O_3 was used as a calibrant with a two point calibration on the second feature of the L_{III} edge and the first feature of the L_{II} edge of 708.5 and 720.1 eV, respectively. The data was collected in the surface sensitive electron yield mode by using a channeltron with 1800 V high voltage and 3000 V collector potentials at about an inch from the sample paddle.

All measurements were collected 2-3 times and averaged. The data normalization, including calibration and background subtraction, was carried out using our Automated Data Reduction Protocol (ADRP)[136] for XANES.

Results and Discussion

Iron Sulfur Minerals

The Fe K-edge spectral features are the result of the Fe 1s core electrons being excited into unoccupied Fe 3d and 4p orbital-based states that correspond to weak electric quadrupole allowed pre-edge and strong electric dipole allowed rising-edge transitions, respectively. Therefore, the rising edge position directly reflects the effective nuclear charge (Z_{eff}) of the iron center. Due to being a result of a weak quadrupole allowed

transition, the pre-edge gains intensity when the Fe 4p mixes with the Fe 3d orbitals, thus allowing for the stronger electric dipole transition. In Figure 4.1, two sets of common iron sulfur minerals are shown: the ferrous sulfides, troilite (FeS) and pyrrhotite (Fe_7S_8) (Figure 4.1A), and the ferrous persulfides (FeS_2), pyrite and marcasite (Figure 4.1B) with crystal structure insets. In the ferrous sulfides, the shift to higher energy of the pyrrhotite is likely due to iron-to-sulfur ratio less than one. From the pyrrhotite crystal structure (Fe_7S_8), it is clear that the iron deficiency results in both five and six coordinate S atoms. Furthermore, the iron deficiency would mean that the formal charge of the iron centers would be greater than two, and thus, corresponds to the rising-edge shifting to higher energy. Both troilite and pyrrhotite have weak pre-edge features that indicate a slightly distorted octahedral environment, which is seen in the crystal structure (inset Figure 4.1A). In the ferrous persulfides, the rising-edge energy position of the marcasite is shifted to slightly higher energy compared to the pyrite. From the crystal structures (inset Figure 4.1B), the pyrite is more symmetric than marcasite; thus, the persulfide will have

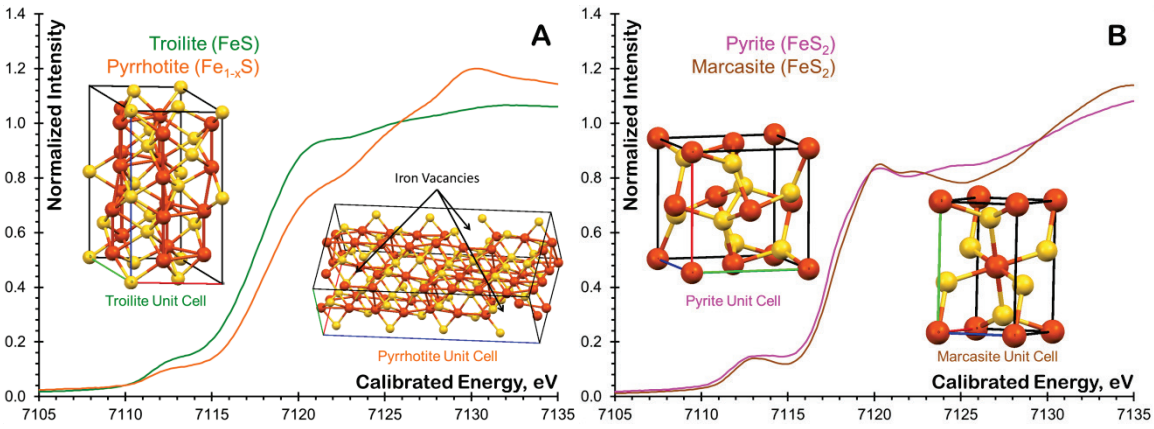

Figure 4.1. The Fe K-edge X-ray absorption near-edge spectra of two ferrous sulfides, troilite and pyrrhotite, (A) and two ferrous persulfides, pyrite and marcasite (B) with inset of their crystal structures

better overlap and donate more electron density to the iron center, resulting in a centrosymmetric. The increase in the pre-edge intensity of the marcasite suggests more Fe 4p character in the metal-ligand bond.

The S K-edge complements the Fe K-edge and provides direct information about the ligand. The S K-edge spectral features are the result of S 1s core electrons being excited to S 3p and 4p based states corresponding to the pre-edge and rising-edge features, respectively. As in the Fe K-edge, the energy position of the rising-edge is directly related to the S effective nuclear charge, $Z_{eff}(S)$. Unlike the Fe K-edge, the pre-edge of the S K-edge is the result of the electric dipole allowed transition to the S 3p base state; since the S 3p is involved in bonding with the iron, the intensity of the pre-edge feature directly corresponds to the S 3p character in the metal-ligand bond. In Figure 4.2A, the rising-edge position of the pyrrhotite is shifted ~1 eV higher energy, corresponding with a more positive sulfur. This indicates that the sulfurs donate more electron density towards the iron centers, due to the higher oxidation state of the iron

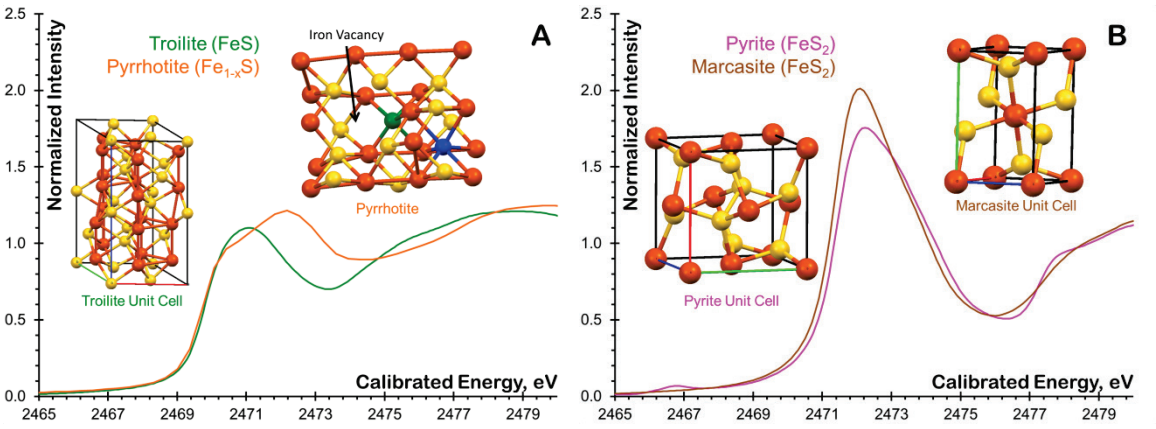

Figure 4.2. The S K-edge X-ray absorption near-edge spectra of two ferrous sulfides, troilite and pyrrhotite, (A) and two ferrous persulfides, pyrite and marcasite (B) with inset of their crystal structures

centers from the Fe-edge. The two pre-edge features of pyrrhotite are due to the different sulfur environments (inset Figure 4.2B) being five (green) *versus* six (blue) coordinate. The first feature is likely the result of the six coordinate sulfurs similar to the troilite, but shift to lower energy with respect to the shift in the rising-edge, indicating more oxidized irons as seen in the Fe K-edge. The second feature is more intense and shifts approximately 0.5 eV higher in energy, likely the result of the five coordinate sulfurs. In Figure 4.2B, there is no resolvable difference in the rising-edge energy positions of the pyrite and marcasite. But from the iron K-edge, we would expect the marcasite to be shifted slightly lower in energy. The pre-edge provides more conclusive information. The pre-edge energy position of marcasite shifts about ~0.2 eV lower in energy, indicating a more oxidized iron center that complements the iron K-edge. The more intense pre-edge of the marcasite is a combination of a shift in the S-S σ* anti-bond and different bonding environment.

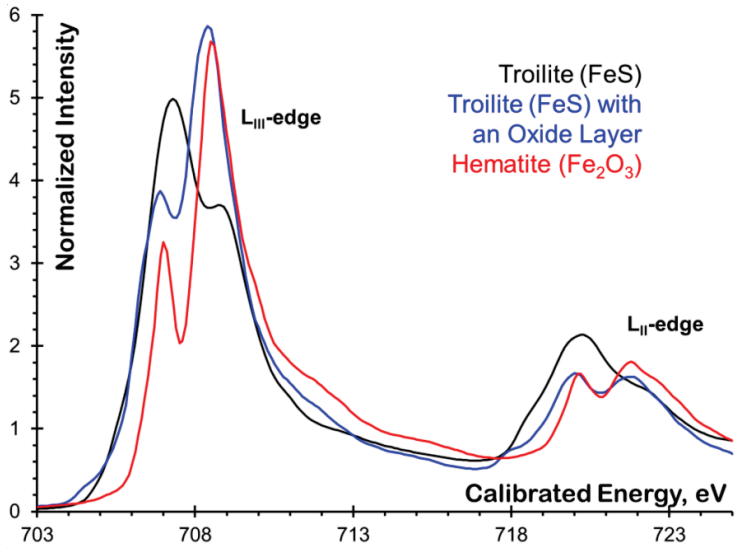

Figure 4.3. The Fe L-edge X-ray absorption near-edge spectra of clean troilite (black), troilite with oxide layer (blue), and hematite (red)

The Fe L-edge provides a unique challenge in both data collection and data reduction. Total electron yield detection is used due to the low fluorescence yield; thus, measurements are sensitive to surface composition. In the case of iron-sulfur systems, this can cause problems if samples are not prepared anaerobically. Therefore, the surface sensitive XAS measurement may result in an iron-oxide-like spectrum as shown in Figure 4.3. Note that the iron oxide is shifted slightly higher in energy, indicating that the iron sulfide surface is not completely oxidized. Furthermore, different experimental setups and variation in beamline optics cause variation in the background and even relative intensities. This presents a problem for data reduction and comparing spectra from different beamlines. Overcoming these issues can be challenging and contributed to an incomplete data set for the L-edge in comparison to the K-edge data.

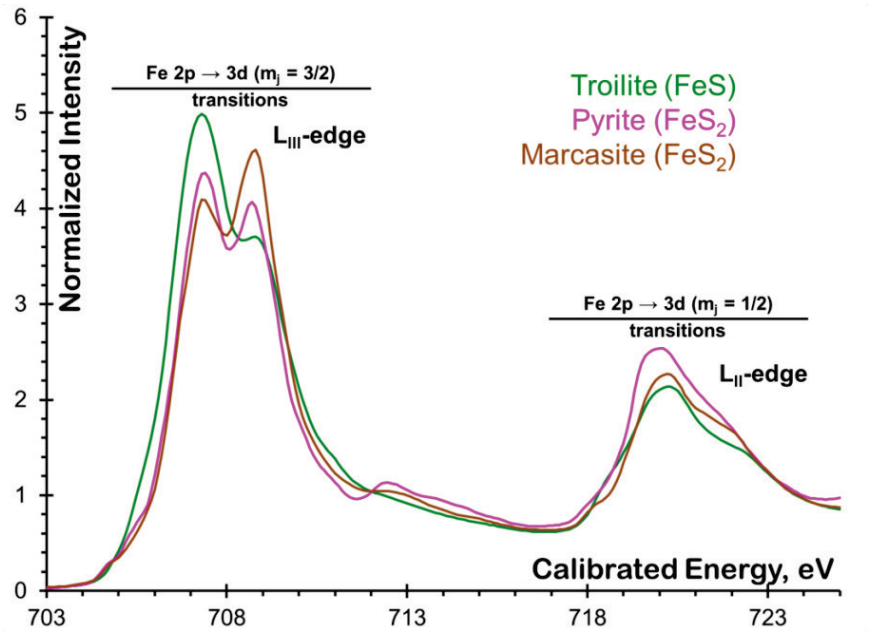

Figure 4.4. The Fe L-edge X-ray absorption near-edge spectra of iron-sulfur minerals, troilite, pyrite, and marcasite

Figure 4.4 contains the Fe L_{III}- and L_{II}-edge XANES for troilite, pyrite, and marcasite. The L-edge originates from the transition of 2p core orbitals. Due to spin-orbit coupling, excitations of the 2p shell electrons split into two edges, where the total electron angular momentum (including both orbital and spin contributions) is J=1/2 (L_{II}) and 3/2 (L_{III}), respectively. Since L-edges arise from electric dipole allowed Fe 2p → 3d transition, the spectral intensities of pre-edge features are directly related to the 3d character in the metal-ligand bond. Furthermore, the shape of the features provides insights into the ligand field splitting if not too convoluted by multiplet effects. In Figure 4.4, the splitting of the L_{III}-edge features corresponds to the different ligand environments around the Fe centers. Troilite has a much smaller splitting than either pyrite or marcasite, indicating a more octahedral environment as seen from the Fe K-edge and confirmed by the crystal structure.

Synthetic Iron Sulfur Particles

Figure 4.5 summarizes the Fe and S K-edge XANES of freshly precipitated ferrous sulfide and two preparations of ferric sulfide, fresh and aged, where fresh $Fe(III)_2S_3$ was made freshly before data collection and aged $Fe(III)_2S_3$ sat for approximately a week before collection. The shift from ferrous sulfide to the ferric sulfides is as expected; however, for the fresh $Fe(III)_2S_3$, the rising edge position falls between the Fe(II)S and the aged $Fe(III)_2S_3$. The pre-edge features also show remarkable differences. The fresh $Fe(III)_2S_3$ pre-edge is intense, indicating that the structure lacks centrosymmetry. The aged $Fe(III)_2S_3$ has a less intense pre-edge feature, indicating a more centrosymmetric iron center, and the broader pre-edge peak could be a result of the

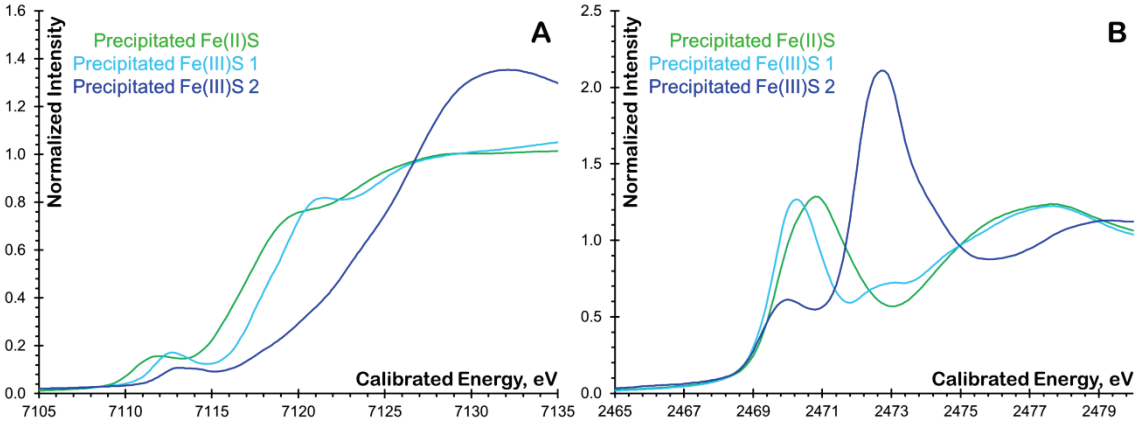

Figure 4.5. The (A) Fe and (B) S K-edge X-ray absorption near-edge spectra of freshly precipitated ferrous sulfide and two ferric sulfides

splitting d orbitals. Thus, the different preparations contain a varied amount of Fe(II) and Fe(III) with aged $Fe(III)_2S_3$ having the most Fe(III). A theoretical study[175] suggests that Fe_2S_3 cannot exist separately from pyrrhotite, but must be a metastable phase of pyrrhotite. In contrast, an earlier study[176, 177] has shown a stable form at low temperatures using Mössbauer spectroscopy. So even if the Fe_2S_3 decomposes slowly at room temperature, it is likely that the metastable phase of Fe_2S_3 is form in the pyrrhotite phase during synthesis that slowly decomposes to the more stable iron-sulfur phase over time. The S K-edge seems to support this analysis. Figure 4.5B shows dramatic differences between the synthesized iron sulfides. Freshly precipitated ferrous sulfide rising-edge position is slightly lower than fresh $Fe(III)_2S_3$, indicating a more reduced sulfur center, and thus less donation to the iron center. Comparing the two $Fe(III)_2S_3$ compounds, the rising-edge energy position shifts to higher energy, going from fresh to aged $Fe(III)_2S_3$, and indicates a more oxidized sulfur center. This follows the trend from the Fe K-edge; the more oxidized the iron center, the more donation of the sulfur center to the iron

center. Comparing the differences of the pre-edge, the ferrous sulfide (Figure 4.5B) pre-edge is at a slightly higher energy position than fresh $Fe(III)_2S_3$, corresponding to sulfides coordinated to a less oxidized iron center. The pre-edge feature is also asymmetric with a shoulder at approximately the energy position of fresh $Fe(III)_2S_3$ pre-edge position. The lower energy peak could arise from a sulfur absorber close to a slightly more oxidized iron center. More dramatic differences were observed by looking at the differences between the ferric sulfide precipitations. The aged $Fe(III)_2S_3$ clearly shows two pre-edge features and a higher rising edge position. The first feature energy position is approximately the same as fresh $Fe(III)_2S_3$ pre-edge feature and the shoulder on the ferrous sulfide. Due to the similarity with the synthesized and mineral ferrous sulfides pre-edge features, the lower energy pre-edge feature could be a result of a sulfide near a Fe(II)-like center. Furthermore, this feature may be an indicator of the pyrrhotite-like phase. The second pre-edge feature is the result of a more oxidized sulfur. The higher energy rising-edge suggests a more oxidized sulfur, and therefore, the peak is shifted to higher energy due to the rising-edge shift. The higher intensity is partially a result of the mixture of sulfur environments, and thus, the rising-edge of the more reduced sulfide increases the intensity. Thus, this supports the conclusion of a mixture of iron sulfur phases. Interestingly, the fresh $Fe(III)_2S_3$ also has a smaller pre-edge feature (~2472 eV) at approximately the same energy position of aged $Fe(III)_2S_3$, suggesting that it also has sulfurs near a more oxidized metal center.

The analysis of the Fe and S K-edge show that the synthesis of iron sulfide results in different iron sulfur phases. Not even the more stable ferrous sulfide produced a

stoichiometric phase. Also, the decomposition of ferric sulfide over time resulted in a mixture of iron-sulfur phases. Furthermore, the detection methods could be providing a more fascinating picture. The Fe K-edge XAS was collected in transmission mode which probes the bulk, and the S K-edge was collected using fluorescence yield detection which probes the interface layer between the surface and the bulk.[70] Thus, the interface layer of the ferric sulfide provides insights into the transition of the phases between the surface and the bulk for ferrous sulfide, and the bulk ferric sulfide.

Biomineralized Iron Sulfur Particles

Figure 4.6 summarizes the Fe (Figure 4.6A) and S (Figure 4.6B) K-edge XANES of the bio-mineralized ferrihydrate and iron sulfide cores in ferritin cages (see Materials and Methods). In Figure 4.5A, the rising-edge energy position of the ferrihydrate core shifts to a lower energy position when converted to a iron sulfide core as expected due to the more reducing nature of sulfur. The pre-edge feature of the iron sulfide core is intense compared to the ferrihydrate core, indicating a distorted octahedral environment.

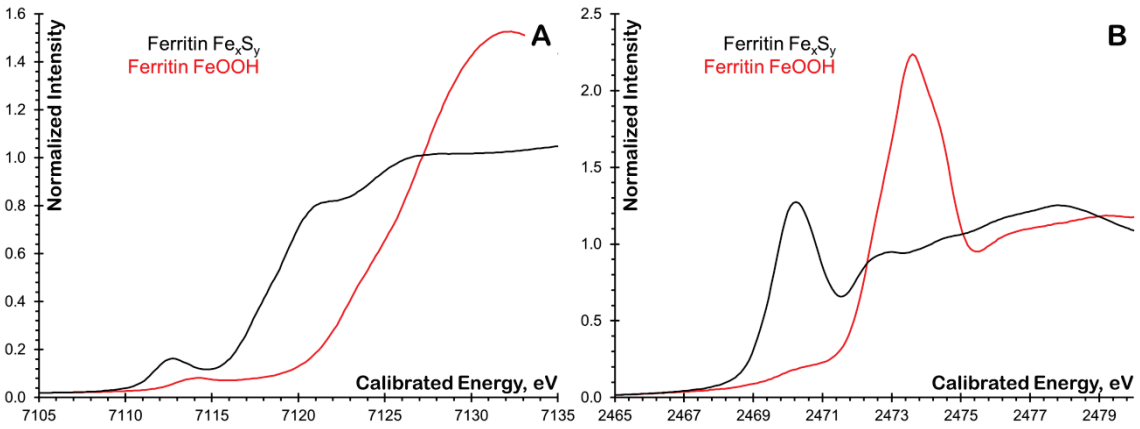

Figure 4.6. The (A) Fe and (B) S K-edge X-ray absorption near-edge spectra of bio-mineralized ferrihydrate and iron sulfide cores in ferritin cages

In Figure 4.6B, the iron oxide core has an intense pre-edge feature around ~2474 eV, corresponding to the cysteines in the protein structure. The small pre-edge feature at ~2471 eV indicates iron bound to the ferritin cage. This means that Fe K-edge EXAFS analysis could possibly show the structure of the iron oxide at the core and protein interface. The iron sulfide core has a pre-edge feature around ~2470 eV similar to the precipitated ferrous sulfide and the ferric sulfides, indicating that at least some of the sulfurs are in a similar environment. There is also a small pre-edge feature around ~2473 eV similar to the pre-edge features of ferric sulfide in Figure 4.5B. This would imply that some of the sulfurs are near iron centers with greater oxidation states. The Fe K-edge also supports this conclusion since the rising-edge position of the iron sulfide core is about ~2 eV higher than the precipitate ferrous sulfide (see Figure 4.5A).

As stated previously, the Fe K-edge XAS was collected in transmission mode, which probes the bulk, and the S K-edge was collected using fluorescence yield detection, which probes the interface layer between the surface and the bulk.[70] Due to the size of the ferritin cage (inner and outer diameter of 8 and 12 nm, respectively), the S K-edge probes the bulk as in the Fe K-edge. Thus, we can exclude the possibility of a ferrihydrate core covered by iron sulfide. The Fe K-edge only shows one edge position, indicating the presence of only one iron oxidation or more likely irons with very similar oxidation states.

Conclusion

From multi-edge X-ray absorption spectroscopic experiments, we have demonstrated the power of this technique to draw conclusions about the electronic structure of ill-defined synthetic iron sulfur particles. Although there is still much work to be done in defining the different features and missing sample sets to compare, there is clearly potential for uncovering new insights about their structure, the interaction of the Fe-S particle and the biomacromolecules. The understanding of their structure at the atomic level may have implications to tailor their properties and to define new methods for synthesizing these nanometer scale particles. Through the analysis of XAS, the electronic and structural changes can be observed for modified bio-mineralized nanometer scale particles. We have shown the possibility to follow the decomposition and conversion process of oxidized iron sulfide particle due to its inherent redox instability.

In order to complete this study, we would need to collect the full Fe L-edge data set for all samples. Due to sample collection at the Fe L-edge (surface detection), most of the Fe L-edge data collected contains an iron oxide surface layer obscuring the electronic structure of iron sulfur (exceptions are shown above). This did not affect the other edge because of the depth of different detection methods probing either bulk or interface layers. Due to the difference in the sample preparations, the ferric sulfide particles need to be re-synthesized and collected to confirm the spectral differences. Given the recent installation of the variable field, variable temperature Mössbauer instrument, we are now in an ideal position to follow changes in oxidation and spin states at MSU and only

collect structural data for an optimized set of samples at the remote synchrotron beamlines. With only one set of data for the bio-mineralized iron sulfur particles in ferritin, we do not have enough data to tell how changing the size of the protein cage will affect the mineralization. A series of protein cage sizes would greatly benefit this study in determining the electronic structural change as size of the particle changes. Furthermore, the same series of protein cages with variation in cage modification would show if control over the mineralization electronic and geometric structures could be obtained. From this unique controlled bio-mineralization of iron sulfur particles, new insights into the effects of size and structure have on linking clusters to minerals.

CHAPTER 5

INVESTIGATION OF EXPOSED PYRITE SURFACE TO ATOMIC HYDROGEN BEAM: PART 1. IRON K-EDGE

Introduction

Biological iron-sulfur clusters[178] provide well defined examples of highly evolved catalytic systems that are capable of carrying out kinetically challenging small molecule activation reactions, such as nitrogen reduction to ammonia or reversible hydrogen uptake and evolution in nitrogenases[179-181] and hydrogenases,[26, 182-184] respectively. The promise of developing novel catalytic systems that mimic the reactivity of metalloenzymatic active sites which are composed of abundant Fe and S components has already fueled intense synthetic,[9, 185] spectroscopic,[11] and structural research.[186] In addition to their technological potential,[187-189] iron-sulfur systems, including particles and minerals,[62] have also been implicated as the catalytic component in the chemical evolution of the building blocks of life.[190-193]

As a first step in the investigation of mineral surface defects as functionally analogous and structurally related biomimetic systems, in collaboration with Minton Lab, we explored the surface modifications created by molecular beams of hydrogen atoms (in their deuterated form) on the (100) surface of pyrite (FeS_2). Formally, pyrite is composed of low spin ferrous iron (Fe(II)) and persulfide (S_2^{2-}) ions. The Fe(II) and S_2^{2-} ions can be

---

This section contains text coauthor by Li Che, David J. Gardenghi, Robert K. Szilagyi, and Timothy K. Minton (2011) *Langmuir* 27, 6814–6821.

considered as a reduced form of the ferric (Fe(III)) ion and the oxidized form of two sulfide ions, respectively. The latter are the common biological forms of iron and sulfur ions. The reduced metal and oxidized ligand is a remarkable chemical pairing that has potential in promoting redox reactions. These ions are organized in a simple cubic structure with slightly distorted octahedral coordination at almost 5 degrees (average deviation ideal S-Fe-S angles) for the Fe(II) ions. Contrary, there is a tetrahedral coordination around each of the S atoms of the persulfide ions. The lattice parameter of the crystal is 5.42 Å, with Fe-S and S-S bonds of 2.26 Å and 2.14 Å, respectively.[194] Although Fe in pyrite is typically more reduced than Fe in the biological systems, atomic hydrogen has the potential to reduce the Fe sites further and thus to create surface sites that mimic the catalytically active form of Fe in metalloenzymes, such as FeFe-hydrogenases.[195] The use of molecular beam techniques allows for energetically controlled and systematic creation and probing of surface defects. Such techniques provide the ability to bombard a surface with atoms or molecules of known composition, directionality, and kinetic energy. Products that scatter from a temperature-controlled surface may be detected as a function of their mass, velocity, and scattering angle. The observed scattering behavior may be used to infer details about gas-surface energy transfer and reactions, as well as chemical and physical transformations on the surface.

Beam-surface scattering experiments were carried out in Minton's laboratory by collaborator Dr. Li Che with the use of a molecular beam/surface scattering apparatus (see Figure 5.1).[196-198] An effusive beam containing D atoms and a supersonic beam containing N_2 molecules were directed at pyrite surfaces, which were mounted at the

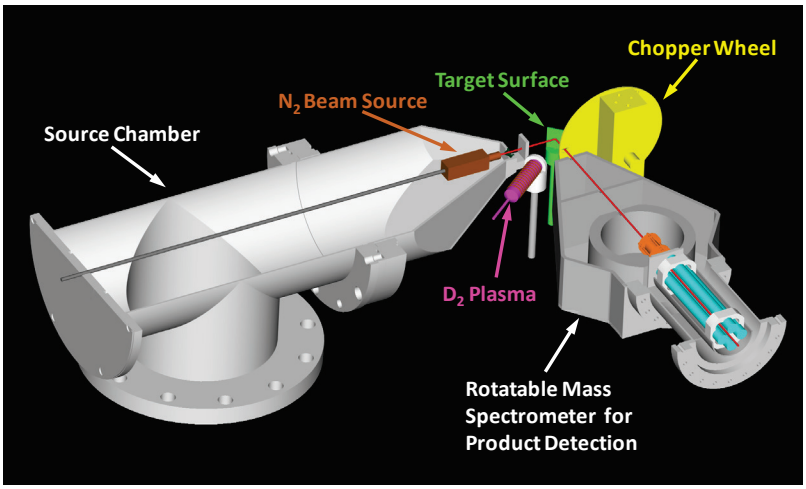

Figure 5.1. Pictorial diagram of the molecular beam apparatus from Minton's laboratory, configured for beam-surface scattering experiments

center of rotation of a rotatable mass spectrometer detector. Products that scattered from a sample surface were monitored with this detector. A spinning slotted disk ("chopper wheel") was placed in front of the detector in order to modulate the products and thus allow their velocity distributions to be determined by the time-of-flight method.

A 40 W radio-frequency (13.56 MHz) plasma was used to produce deuterium atoms from a mixture of D_2 in Ar. The addition of Ar to the D_2 gas was needed for the production of a stable plasma. The partially dissociated mixture was expanded through a 0.5 mm diameter orifice to form an effusive beam containing D atoms, D_2 molecules, and Ar atoms. Control experiments were conducted with the use of an effusive beam produced with pure Ar gas in the plasma source. A second beam was used for some of the experiments. This was a supersonic beam that was formed by expanding a mixture of 1% N_2 seeded in H_2.

The samples were cut from natural single crystal pyrite cubes (Logrono, Spain) that were purchased from Ward's Natural Science. The as-received (100) faces of the

pyrite samples were used. As the samples are naturally grown surfaces, there are macroscopic striations on the surfaces. Native oxides on the sample surfaces were removed by dipping the samples in a 1 M HCl solution for 5 min at room temperature, followed by a rinse with deoxygenated water. After this cleaning procedure, samples were immediately mounted on a sample mount in the main chamber of the molecular beam apparatus, and the chamber was evacuated to 2×10^{-7} Torr. Mounting of the sample was carried out by pressing the surface of the sample against a square stainless steel rim, with a 9×9 mm window, using a copper backing plate. With this setup, the sample was heated with the use of a cylindrical heater inserted into a hole in the copper plate, and the sample temperature was monitored with a type-K thermocouple that was screwed on the stainless steel mount. The sample temperature could be held at any temperature from room temperature to slightly above 200 °C. Samples were typically changed between exposures to the D-atom beam, as it was usually desirable to start with a pristine surface.

Time-of-flight (TOF) distributions were collected by Dr. Li Che of the Minton Lab with the use of the chopper wheel. Figure 5.3A shows a representative TOF distribution of D_2S molecules that scattered from a near pristine pyrite surface after D atoms collided with it. In this TOF distribution, the raw signal can be fit with a curve that is derived from a Maxwell-Boltzmann distribution of product translational energies at the surface temperature of 100 °C.[197] This observation indicates that D_2S products desorb in thermal equilibrium with the surface. It is thus likely that the incident D atoms adsorbed to the surface and came into thermal equilibrium before or during the reaction to produce D_2S. At the atomic level, the D atom may be trapped at an iron or a sulfur site. Reaction

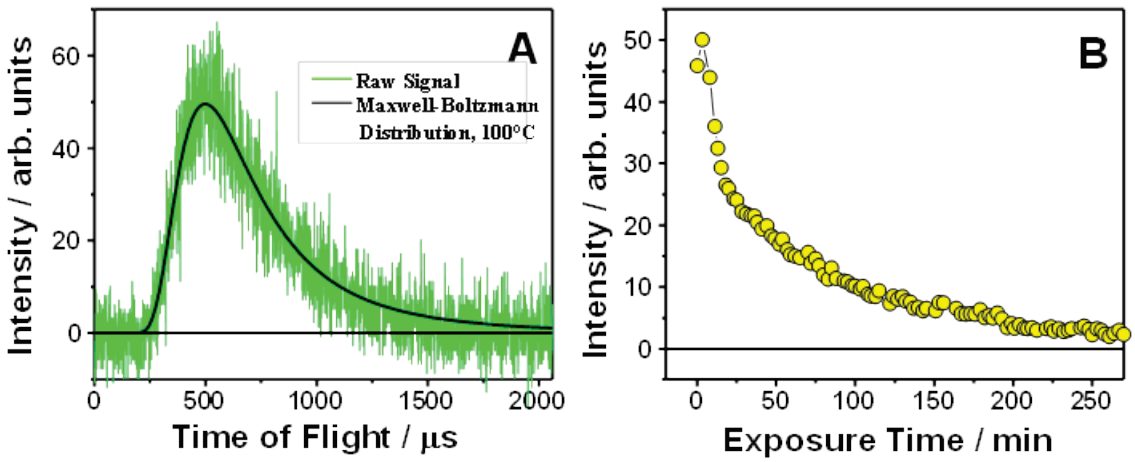

Figure 5.2. (A) Representative time-of-flight distribution of scattered D_2S product detected at a final angle, θ_f, of 45° when D-atoms bombarded a pyrite surface with an incidence angle, θ_i of 0º, with the surface temperature held at 100 °C. (B) Integrated intensity of D_2S signal as a function of exposure time to the D-atom beam, with θ_i = 0° and θ_f = 45°

of a formally Fe(II) site with a D atom can result in either formation of a formally Fe(I) site and a D^+ ion, or an Fe(III) site with a bound D^- (hydride) ligand. Given that D_2S is the observed product, the reduced Fe site is more likely as the D^+ ion needs to migrate to a nearby S atom and leave its electron behind on the Fe site. A more complete speciation map for the variety of species that can be formed is discussed in Chapter 6. As indicated from an earlier study,[62] creation of the (100) surface may cleave the persulfide bond, leaving behind a S^- radical anion. This relaxes to a terminal sulfide by oxidizing the adjacent Fe center. Reaction of a D atom with a dangling sulfide S is expected to result in a reduced Fe site coordinated by a sulfhydryl SD^- ligand. The arrival of the second D atom would provide further reduction of the formally Fe(I) site or reduction of another Fe(II) site, and consequently after D^+ migration, the complete cleavage of the S-S bond and formation of the D_2S product.

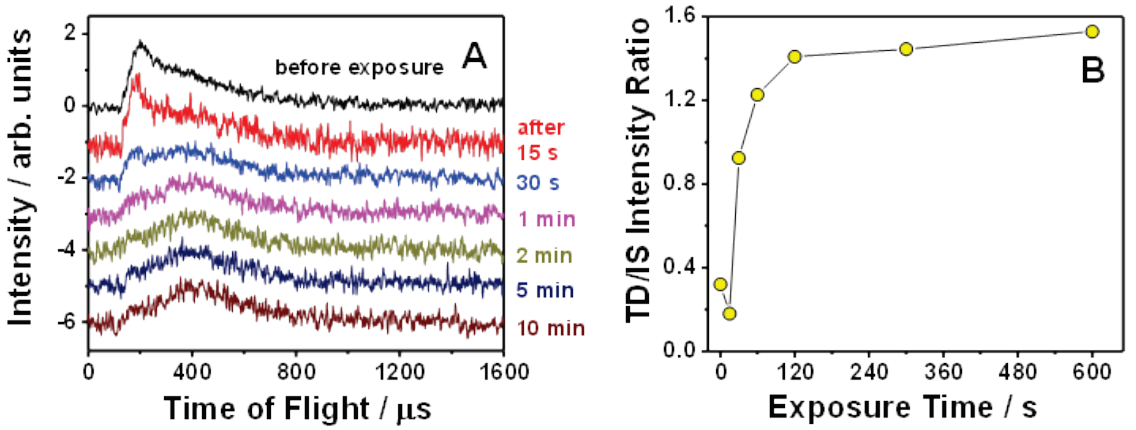

Figure 5.3. (A) Time-of-flight distributions of inelastically scattered N_2, with $\theta_i = \theta_f = 45°$, collected after the D-atom exposure durations indicated. Each exposure began with a pristine pyrite sample. (B) Intensity ratio of thermal desorption (TD) to inelastic scattering (IS) obtained from the time-of-flight distributions in (A)

The time dependence of D_2S product intensity calculated from integrating $N(t)/t$ over the flight time at $\theta_f = 45°$ is shown in Figure 5.2B.[197] Notably, in the first few minutes, the D_2S signal increases and then decreases, roughly exponentially, with exposure time. The initial increase can be attributed to sputtering of exogenous contaminants from the surface that the acid wash and deoxygenated water rinse was unable to remove. Also, a thin layer of contamination may be present, as the samples were transferred through air after cleaning and prior to their being mounted in the vacuum chamber. The *in situ* generated fresh surface reacted with the beam of D atoms and clearly shows the depletion of surface accessible S atoms in Figure 5.2B.

The inelastic scattering with a supersonic beam of N_2 molecules used to investigate the development of surface roughness as D atoms eroded the surface to produce D_2S. TOF distributions of N_2 collected after various durations of D-atom exposures are shown in Figure 5.3A. In each case, the TOF distribution of inelastically

scattered N_2 was collected after a fresh pyrite surface was exposed to the effusive D-atom beam for the indicated period of time and then the exposure was stopped. The TOF distributions for inelastically scattered N_2 typically exhibit two components, which can be described in terms of two limiting cases of thermal desorption (TD, slower component at longer flight times) and direct inelastic (IS, faster component at shorter flight times).[197, 198] In the TD process, the N_2 molecules desorb with a Maxwell-Boltzmann distribution of velocities corresponding to the surface temperature, perhaps after becoming momentarily trapped on the surface. In the IS process, the N_2 molecules scatter directly, after one or a few bounces, and only lose a fraction of their incident kinetic energy on the surface. As seen in Figure 5.3A, the IS component has a maximum at a flight time near 200 μs, and the TD component has a maximum near 400 μs. Before D-atom exposure, the IS component dominates, but as the D atoms bombard the surface for longer times, the IS component decreases and the TD component becomes dominant. The relative contributions of the IS and TD components to the scattered flux have been determined by standard means,[197, 198] and the ratio of TD to IS scattering is shown in Figure 5.3B. After a small decrease resulting from sputtering of contaminants (see above), the ratio increases rapidly. The rise in the dominance of the TD component is consistent with an increasing surface roughness, which leads to enhanced multiple-bounce scattering at the surface and drives the N_2 molecules into thermal equilibrium with the surface. The increased surface roughness with D-atom exposure has been confirmed by FE-SEM and AFM of the exposed pyrite samples record by Dr. Li Che from the Minton laboratory. FE-SEM and

AFM images for pyrite surfaces exposed to D-atoms for 0, 5, and 270 minutes are shown in Figure 5.4. These images reveal surface roughening on a nanometer-size scale.

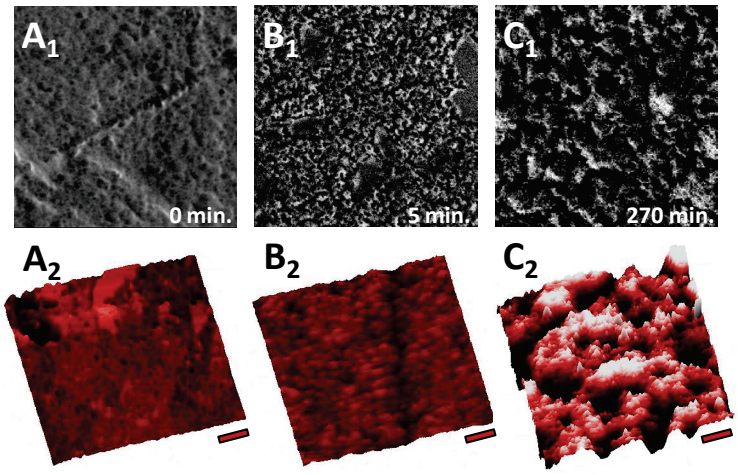

Figure 5.4. (A_1 – C_1) FE-SEM images of 2 μm × 2 μm regions of a pristine pyrite surface and pyrite surfaces exposed for 5 and 270 minutes to the D-atom beam. The surface temperature was 100 °C. (A_2 – C_2) AFM images of the same samples in A_1 – C_1. For A_2 and B_2, the image size is 5 μm × 5 μm and the z scale is 60 nm. For C_2, the image size is 20 μm × 20 μm, and the z scale is 300 nm. RMS roughnesses are 4 nm (A_2), 14 nm (B_2), and 100 nm (C_2)

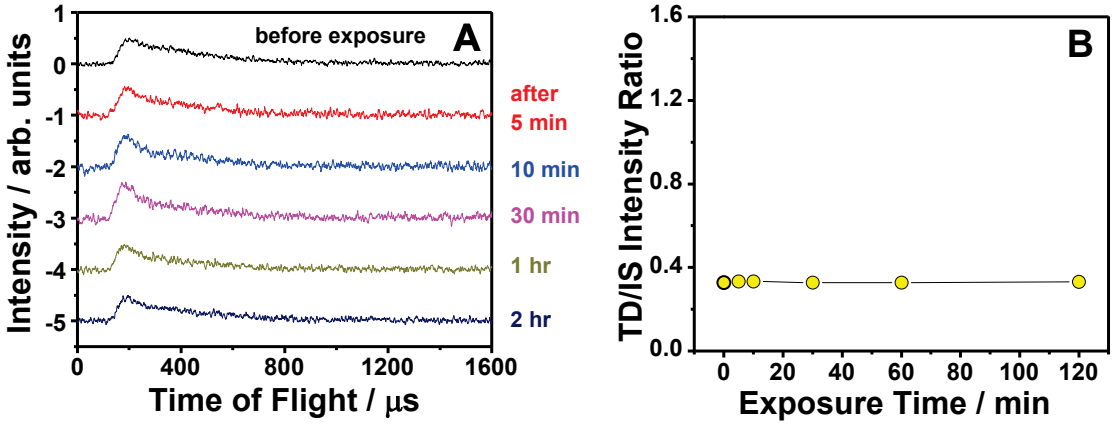

Figure 5.5. (A) Time-of-flight distributions of inelastically scattered Ar, with $\theta_i = \theta_f = 45°$, collected after the A exposure durations indicated. Each exposure began with a pristine pyrite sample. (B) Intensity ratio of thermal desorption (TD) to inelastic scattering (IS) obtained from the time-of-flight distributions in (A)

Ar. Fresh pyrite samples were exposed to the pure Ar beam for various durations, and after a given duration, the exposure was stopped and a TOF distribution of inelastically scattered N_2 was collected. The TOF distributions of inelastically scattered N_2 are presented in Figure 5.5. In contrast to the results with the D-atom beam, there is no visible change in the shape of the N_2 TOF distributions with exposure time. Therefore, the surface does not roughen when exposed to Ar alone. Thus it was concluded that Ar plays no role in the reaction at the surface or in the development of surface structure. These observations have also been confirmed by XAS measurements (see below) by showing identical spectra for the control pyrite and the Ar exposed pyrite surface samples. The surface roughness caused by exposure of pyrite to the D-atom beam, which also contained Ar, must therefore be the sole result of reactions of D atoms with the surface.

X-ray absorption spectroscopy (XAS) measurements at the Fe K-edge (energy range of 7-8 keV) were employed to evaluate changes at the atomic scale with respect to both geometric and electronic structures from Extended X-ray Absorption Fine Structure (EXAFS) and X-ray Absorption Near-Edge Structure (XANES) analyses, respectively. In order to probe various depths of the surface, we employed three detection methods. The most commonly used transmission setup was used to gain information about the structure of the bulk for powder samples. Fluorescence detection with an approximate escape path in the order of 20-50 nm provided information about the intermediate layer between the bulk and the top surface. Electron-yield detection with a shallow escape depth of a few nanometers is highly surface sensitive and provides information about the top molecular

layer of a surface.[70] The combined application of three complementary detection methods and employment of both EXAFS and XANES allowed us to uncover structural details of hydrogen-atom-modified pyrite surfaces, which showed a remarkable relevance to small molecule activation catalysis in biological systems.

Experimental Methods

X-ray Absorption Spectroscopy Measurements

X-ray absorption spectroscopic technique was used to investigate the chemical changes on the surfaces that were exposed to D and Ar atoms. XAS measurements were carried out at beamlines 7-3 and 4-3 of the Stanford Synchrotron Radiation Light Source (SSRL) under storage ring (SPEAR 3) conditions of 3 GeV energy and 200-120 mA current. BL7-3 is a 20-pole, 2 T Wiggler beamline equipped with a Si(220) downward reflecting, double-crystal monochromator. Data was collected in the energy range of 6900-8000 eV using an unfocused beam. Samples were mounted on a sample paddle at 45º relative to the incident beam and the 30-element Ge array detector and with a Soller slit and a Mn (Z-1) filter. The energy windowing of the detector was carefully adjusted to minimize the fluorescence signal due to scattering and other non-Fe Kα emission sources. The beamline parameters were optimized at 8000 eV. Transmission experiments were carried out for reference pyrite powder ground and mixed with BN in an optimal composition for transmittance measurements as determined by using the SAMPLE4 program of EXAFSPAK.[199] BL4-3 is a 20-pole, 2.0 T Wiggler beamline with a liquid nitrogen-cooled, Si(111) double-crystal monochromator. Fe K-edge spectra were

collected using an unfocused beam in a He-purged beam path with Lytle fluorescence and electron yield detectors. The incident photon energy was calibrated to the spectra of iron foil at the first inflection point of 7111.2 eV, which was estimated from the energy position of the first maximum of the first derivative along the rising edge. The data normalization including calibration and background subtraction was carried out using our Automated Data Reduction Protocol (ADRP)[136] and SixPACK[200] for XANES and EXAFS, respectively.

Results and Discussion

Fe K-edge XAS Results

In order to obtain atomic-level information about both the electronic and geometric structures of the modified pyrite surfaces, we carried out X-ray absorption spectroscopic investigations at the Fe K-edge using different detection methods that probed the pyrite surface at various depths. Figure 5.6 summarizes two sets of XANES spectra of structurally well-defined reference compounds of iron oxides and sulfides. The

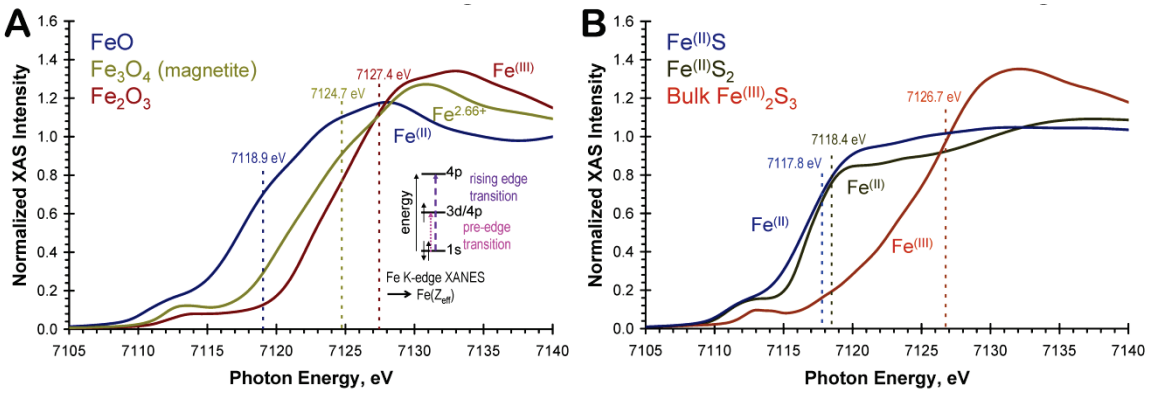

Figure 5.6. Reference Fe K-edge X-ray absorption near-edge spectra of reference iron oxides (A) and sulfides (B)

inset in Figure 5.6A illustrates the origin of spectral features as the Fe 1s core electrons are being excited into unoccupied Fe 3d and Fe 4p based states giving rise to weak electric quadrupole and strong electric dipole allowed pre-edge and rising-edge transitions, respectively. As a result of the considerable difference in the Fe effective nuclear charges, the rising-edge features of more reduced Fe(II) compounds are shifted to lower energies relative to the more oxidized Fe(III) compounds. In Figure 5.6A, the rising edge inflection point of magnetite (7124.7 eV) with a formal oxidation state of $Fe^{2.66+}$ is located proportionally in between those of the formally Fe(II)O (7118.9 eV) and $Fe(III)_2O_3$ (7127.4 eV) spectra. The analogous rising-edge inflection points of the corresponding sulfides, seen in Figure 5.6B, are located at 7117.8 eV and 7126.7 eV for freshly precipitated Fe(II)S and $Fe(III)_2S_3$ samples. The sensitivity of these XANES measurements to the effective oxidation state of the Fe centers is well demonstrated by the difference between the pyrite ($Fe(II)S_2$) and Fe(II)S spectra. Due to the presence of the S-S bond of persulfide ligand in pyrite, the S atoms can donate less electron density to the Fe sites than the dianonic sulfide in Fe(II)S, and thus the Fe sites remain effectively more oxidized as reflected by the rising-edge position at 7118.4 eV. The effective oxidation state of the Fe in pyrite is slightly higher than in ferrous sulfide precipitate. The same trend is valid for comparing the rising edge inflection points of the spectra of Fe(II)S (7117.8 eV) and Fe(II)O (7118.9 eV). Due to the higher electronegativity of the O than S in addition to the less favorable overlap of Fe 3d and O 2p vs. S 3p orbitals, the metal-ligand bonding in oxides is generally less covalent than in sulfides, and thus the Fe

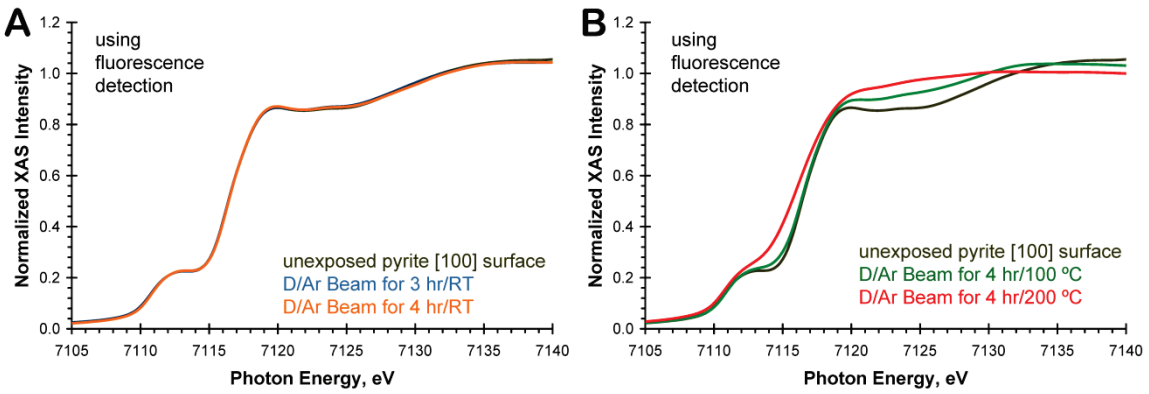

Figure 5.7. Fe K-edge X-ray absorption near-edge spectra collected in fluorescence yield mode for pyrite (100) exposed to the D-atom beam for various times at (A) room and (B) elevated temperatures at an exposure time of 4 hr

will be effectively more oxidized as reflected by the approximately +1 eV shift of the rising edge.

Figure 5.7 summarizes the XANES data collected in fluorescence detection mode for pyrite (100) surfaces as a function of exposure time (Figure 5.7A) and surface temperature (Figure 5.7B) at constant room temperature and 4 hours exposure time, respectively. Significant spectral changes were only observed on surfaces that were held at elevated temperatures when they were exposed to D atoms. For these samples, the rising edge was shifted toward lower energies, and differences were observed in the post-edge energy region (above 7120 eV). The former corresponds to the appearance of more reduced Fe sites than those in pyrite, while the latter is an indication of changes in the atomic structure of the Fe sites.

Much more dramatic changes can be observed for the spectra shown in Figure 5.8B compared to Figure 5.8A, which were collected in electron-yield detection mode. These spectra conclusively show the appearance of a highly reduced Fe phase as well as a

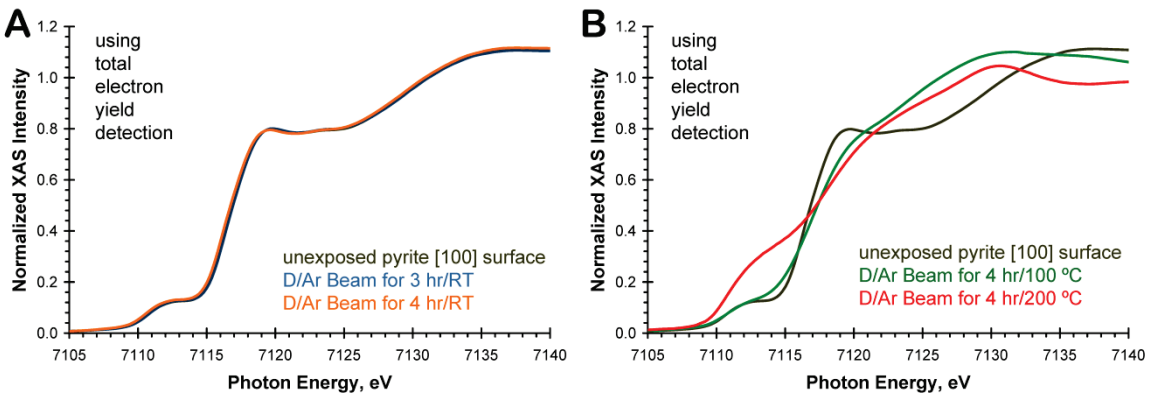

Figure 5.8. Fe K-edge X-ray absorption near-edge spectra collected in electron yield mode for pyrite (100) exposed to the D-atom beam for various times at (A) room temperature and (B) elevated temperatures at an exposure time of 4 hr

complete change in the radial distributions of atoms around the Fe absorbers. The considerable difference between the fluorescence and electron-yield data is the result of the different probe depths of these detection methods. The approximate escape depth for fluorescence radiation is about 20-50 nm, while it is only a few nm for the electron-yield.[70] Thus, Figure 5.7 and Figure 5.8 are indicative of the formation of layered Fe/S phases on the top of bulk pyrite that vary in the degree of reduced state. Based on the depletion of surface accessible S atoms observed in Figure 5.2, the top layer is expected to be fully reduced metallic iron.

The full energy range XAS spectrum in Figure 5.9A, collected in electron-yield mode, and the Fourier-transformed EXAFS region in Figure 5.9B above the ionization threshold of the Fe 1s core electrons (approximate Fe 1s core ionization energy position indicated by a dashed line in Figure 5.9A) allow for the unambiguous assignment of the surface layer, being the same layer as the outer layer of metallic iron powder. In addition to the bulk metallic iron, we anticipate a thin passivating layer of iron oxide, resulting from exposure to air upon sample removal from the vacuum chamber where the

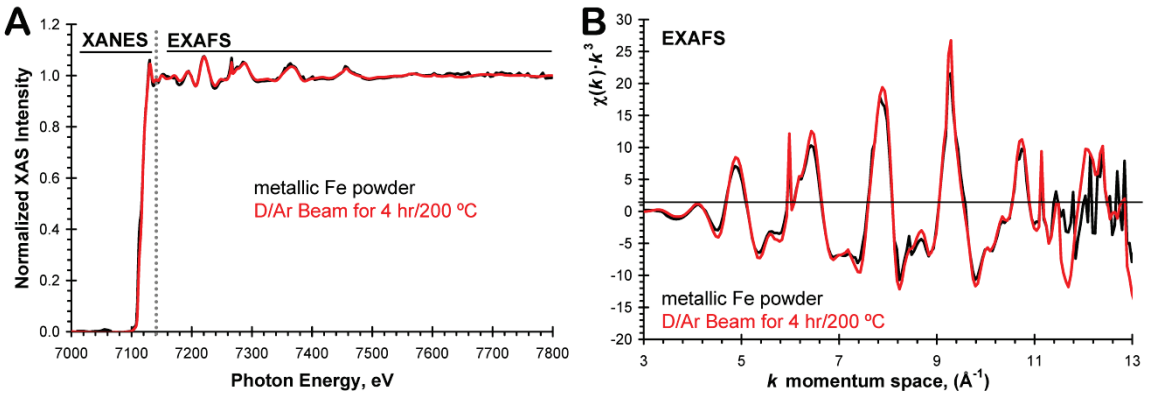

Figure 5.9. Fe K-edge extended X-ray absorption fine-structure analysis of the electron yield data of the 4 hr exposed pyrite (100) sample: (A) in energy space and (B) in momentum (k) space

were conducted, since the XAS data were collected with samples that had been exposed to air.

While this passivating layer is an artifact in our measurements, it is useful because it preserves the interfacial layer between the bulk pyrite and the top layer of metallic iron. Figure 5.10 provides a first glimpse into the electronic structure of this interfacial layer, which was probed by fluorescence detection. In comparison to the metallic Fe and the bulk pyrite, the effective iron oxidation state of this layer is in between that of Fe(II) and Fe(0). While the crossing of spectra for the metallic Fe and pyrite at 7117, 7122, and 7133 eV may be interpreted as isosbestic points, no combination of these two spectra can reproduce the XANES of the interfacial layer. We tentatively assign the formal oxidation state of this intermediate layer to Fe(I) with formal stoichiometry of Fe_2S. The findings from Fe K-edge XANES and EXAFS analysis thus reveal layered Fe-S phases of the D-atom beam surface modified pyrite surface. A pictorial summary is shown in Figure 5.11. The presence of a reduced Fe-S phase is remarkable due to its catalytic implications. The

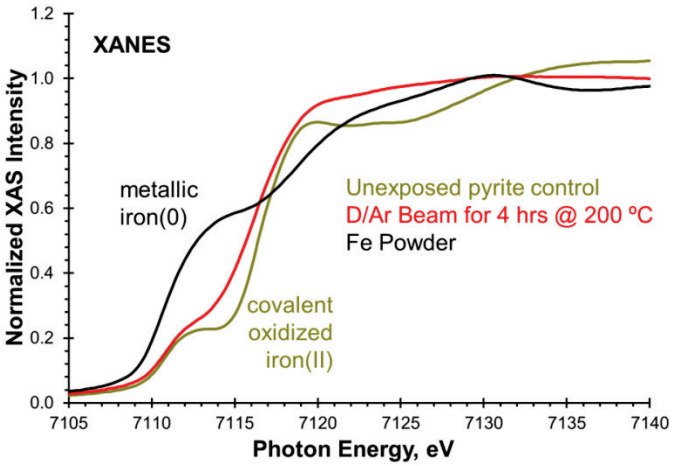

Figure 5.10. Comparison of the K-edge X-ray absorption near-edge spectra for metallic Fe and a pyrite (100) surface that was exposed to the D-atom beam for 4 hr while being held at 200 °C

catalytically active site of FeFe-hydrogenase, the H-cluster,[78] contains a remarkable Fe-S cluster that can adopt formal oxidation states that are similar to the observed reduced intermediate surface layer of pyrite. The H-cluster is one of the most active catalytic centers for the reversible evolution and uptake of H_2 at close to diffusion limited rates.[27, 201] Furthermore, the catalytically active Fe-S cluster of nitrogenase, FeMo-co, undergoes three or four electron reduction before the N_2 substrate can bind, and then it is reduced to NH_3 with concomitant H_2 formation. Although experimentally not yet shown, it is plausible from electron counting that one or perhaps more Fe sites of the FeMo-co cluster reach low valence, reduced Fe sites during the catalytic cycle. One of the inhibitors of biological nitrogen fixation and hydrogen uptake/evolution reactions is CO, which also tends to bind to reduced or metallic Fe sites. The analogy of the electronic structure of the reduced Fe-S phase to the biologically relevant and important catalytic conversion of small, inert molecules, such as N_2 and H_2, makes the reduced Fe-S phase a highly promising catalytic system.

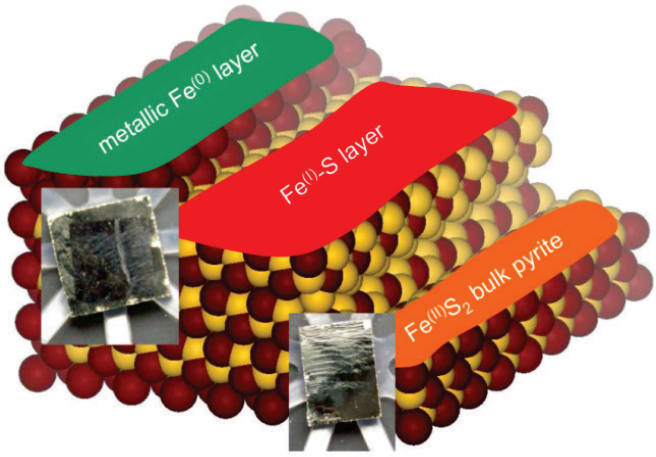

Figure 5.11. Pictorial illustration of the layered Fe-S phases of a pyrite (100) surface that has been reduced by exposure to the D-atom beam at elevated temperatures of 100 – 200 °C

In addition to possible technological implications, the discovery of a unique $Fe(I)_2S$ phase is relevant to the NASA Astrobiology Institute's Mission (Roadmap Objective 3 and 7)[202] as it relates to the interfacial processes between exposed Fe-S containing rocks of the lithosphere and activated molecules from the atmosphere. It is plausible that H_2O, CH_4, and H_2 molecules of the Hadean atmosphere could provide a considerable source of simple radicals under highly ionizing ultraviolet radiation, and hence the exposed mineral surfaces might have undergone modifications to generate reduced metal sites that were desirable for activation of other atmospheric molecules such as N_2, NO, CO/CO_2, etc. Formation of a reduced Fe-S phase and its possible role as an activated catalytic surface is a credible scenario for prebiotic amino acid formation from simple molecules, such as N_2, H_2O, and CO_2.

Conclusion

From combined X-ray absorption spectroscopic and surface-beam scattering experiments from our laboratory and Minton's, respectively, it has been demonstrated that a pyrite surface may react with deuterium (or hydrogen) atoms to produce volatile D_2S, leaving a roughened and reduced surface. We found that D atoms react with a pyrite surface at elevated temperatures (100 ºC and above) and produce D_2S product with a thermal distribution of speeds. The yield of D_2S decreases exponentially with exposure time, suggesting the depletion of surface accessible S atoms. The inelastic scattering dynamics of N_2 on modified surfaces indicated that the surface became significantly rougher during the exposure, which was also in agreement with post-exposure characterization by FE-SEM and AFM. From control experiments using an Ar beam, we unambiguously assigned the source of the increased nanometer scale surface roughness as the chemical reaction of D with S atoms and consequently the formation of a metallic iron rich surface. Notably, the rougher surface has a larger surface to volume ratio, which is an important factor in heterogeneous catalysis. Atomic scale characterization of the surfaces using Fe K-edge X-ray absorption spectroscopic measurements concluded that the top surface of the modified samples is identical to that of the metallic iron. The intermediate layer beneath this top layer and above the bulk pyrite has been determined to contain a previously unknown reduced Fe-S phase, which tentatively was assigned as amorphous $Fe(I)_2S$. This reduced Fe-S phase has recently been shown to be catalytically active in the Minton laboratory, thus suggesting further studies of its utility and providing insights into potentially important steps in the process of small molecule activation.

CHAPTER 6

INVESTIGATION OF EXPOSED PYRITE SURFACE TO ATOMIC HYDROGEN BEAM: PART 2. SULFUR K-EDGE AND IRON L-EDGE

Introduction

Iron-sulfur systems have been an intense area of study due to the importance in both biology and geology. In biology, iron-sulfur systems are the active center of metalloenzymes, and some have proven to be highly catalytic systems such as in nitrogenase and hydrogenase. This has fueled research into developing novel catalytic systems that mimic the reactivity of biological iron-sulfur clusters. In geology, iron-sulfur systems are ubiquitous in nature,[10, 11] and therefore, its surface chemistry can have a significant effect on its environment, such as pyrite in acid mine drainage.[1, 3, 203] Research of surface reactivity of iron-sulfur systems has shown that surface defects seem to be the active site of the iron-sulfur mineral surfaces.[5, 64] The non-stoichiometric sites (defects) could potentially have structural and/or functional similarities to biological iron-sulfur clusters. Although the iron in biological systems is typically more reduced in iron-sulfur minerals, the modification of the surface could create sites that mimic the biological iron-sulfur clusters.

To investigate the functionality of these surface defect sites with relation to biomimetic systems, the previous chapter discussed a Fe K-edge X-ray absorption spectroscopy study of a pyrite surface modified by a molecular beam of deuterium atoms.[204] The molecular beam experiment allowed for systematic control over the

modification of the surface. This experiment showed that the surface sulfur is depleted over time, and that overall surface becomes rough with about 100 nm indentations. The surface sulfur reacted with the deuterium atoms and produced D_2S. From Fe K-edge X-ray absorption spectroscopy, it was shown that the production of D_2S reduces the surface to metallic iron, Fe(0), at elevated temperatures, and the reduction does not stop at the surface. The intermediate layer beneath the top layer and above the bulk pyrite was reduced to a new phase of iron-sulfur, which tentatively was assigned as amorphous $Fe(I)_2S$. Figure 6.1 summarizes the modified pyrite layers formed at elevated temperatures.

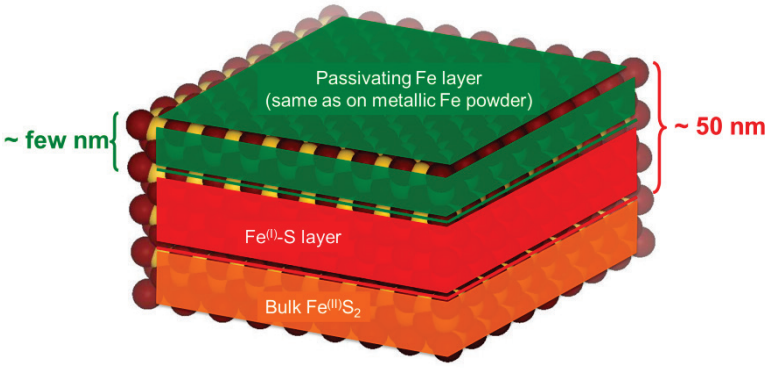

Figure 6.1 Illustration of the layered Fe-S phases of a pyrite (100) surface that has been reduced by exposure to the D-atom beam at elevated temperatures

To further investigate this remarkable chemistry, we extend the X-ray absorption measurements to include the S K-edge and Fe L-edge. Using multi-edge XAS, we obtained complementary information and extended our understanding of how the modified pyrite surface changes over exposure time. As in the previous study, we employed two detection methods, fluorescence and electron yield detection, to probe the

intermediate and surface layers, respectively. The combination of multi-edge X-ray absorption spectroscopy and complementary detection methods allows us to determine a possible mechanism of the reduction of the pyrite surface.

Experimental Methods

X-ray Absorption Spectroscopy Measurements

XAS measurements were carried out at beamlines 4-3 and 10-1 of the Stanford Synchrotron Radiation Light Source (SSRL) under storage ring (SPEAR 3) conditions of 3 GeV energy and 200-120 mA current. BL4-3 is a 20-pole, 2.0 T Wiggler beamline with a liquid nitrogen-cooled, Si(111) double-crystal monochromator. Sulfur K-edge spectra was collected in the energy range of 2450–2740 eV using an unfocused beam in a He-purged beam path at room temperature with a multi-element Lytle fluorescence and partial electron yield detectors. Samples were mounted on a sample paddle at 45º and 90º relative to the incident beam and Lytle fluorescence detector and partial electron yield detector, respectively. Partial electron yield detector was equipped with a nickel grid at a 45 V collector potential. Solid reference samples were diluted with boron nitride and ground together to minimize self-absorption and then mounted onto a sulfur-free kapton tape. Modified pyrite samples were place directly on the kapton tape. The beamline parameters were optimized at 2740 eV. The incident photon energy was calibrated to the spectra of $Na_2S_2O_3 \cdot 5H_2O$ with a maximum pre-edge feature at 2472.02 eV. BL 10-1 is a 30-pole, 1.45 T Wiggler beamline, equipped with a 6 m spherical grating monochromator set to 1000 lines/mm. Spectra were collected in the energy range of 660–800 eV using an

unfocused beam in ultrahigh vacuum (UHV). The beamline was optimized at 715 eV. Fe_2O_3 was used as a calibrant with a two point calibration on the second feature of the L_{III} edge and the first feature of the L_{II} edge of 708.5 and 720.1 eV, respectively. The data was collected in electron yield mode by using a channeltron with 1800 V high voltage and 3000 V collector potentials at about an inch from the sample paddle. The data normalization, including calibration and background subtraction, was carried out using our Automated Data Reduction Protocol (ADRP)[136] for XANES.

Results and Discussion

Fe L-edge Results

As previously shown in Chapter 5, the modified pyrite surface formed layers of Fe in different oxidation states. To gain deeper understanding of the structure from multiple edge perspectives, we carried out X-ray absorption spectroscopic investigation at the Fe L-edge. Due to low fluorescence yield[205] at the Fe L-edge, only electron yield detector was used.

The L-edge originates from the transition of 2p core orbitals. Due to spin-orbit coupling, excitations of the 2p shell electrons split into two edges, L_{II} & L_{III}, where the total electron angular momentum (including both orbital and spin contributions) is J=1/2 and 3/2, respectively. For first row transition metals, the L_{II} and L_{III} arise from the electric dipole allowed 2p → 3d transition. This transition is about an order of magnitude more intense than the Fe K pre-edge. Therefore, more electronic information can be obtained about the Fe 3d character from the L-edge *versus* the K-edge. Yet, due to the intense pre-

edge features, the rising edge position is not resolved. Thus, the effective oxidation state of the Fe is more difficult to see in the L-edge *versus* the K-edge. Furthermore, the shape of the features permits insights into the ligand field splitting when it is not masked by multiplet effects due to orbital-orbital and spin-orbital coupling effects of the Fe 3d orbitals and their interacting ligand orbitals.

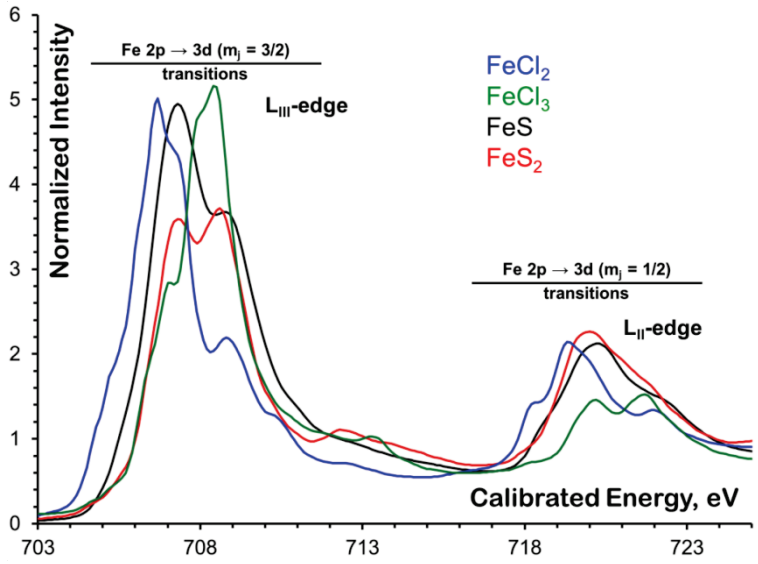

Figure 6.2. Reference Fe L-edge X-ray absorption near-edge spectra of reference iron chlorides and sulfides

Figure 6.2 summarizes two sets of structurally well-defined reference compounds of iron chlorides and sulfides. In Figure 6.2, the rising edge of the formally Fe(II) and Fe(III) iron chlorides are obscured by the pre-edge features, yet the shift in the pre-edge features can still be observed. The more reduced $FeCl_2$ L_{III} maximum is shifted down ~2 eV compared to $FeCl_3$. The shift is small compared to the Fe K-edge (about twice the L_{III} edge). The analogous shift in the iron sulfide compounds, seen in Figure 6.2, is negligible. From the Fe K-edge, we know that the Fe sites in Fe(II)S are slightly more

reduced than in Fe(II)S_2 due to the persulfide bond; therefore the shift is too small. Unlike the Fe K-edge, the intensity of the L-edge pre-edge is very sensitive to change in the electronic structure, such as increased number of holes and/or orbital character. The Fe(II)Cl_2 has a lower overall (including background) L_{III} intensity than Fe(III)Cl_3 due to the increase in the number of holes in the 3d orbitals. For Fe(II)S and Fe(II)S_2, Fe(II)S has a more intense L_{III}-edge than Fe(II)S_2, corresponding to more 3d character in the iron-sulfur bond. Also insights into ligand field splitting can be qualitatively determined. Both Fe(II)S and Fe(II)S_2 show splitting of the L_{III}-edge, indicating the loss degeneracy of the e_g orbitals. For Fe(II)S, the splitting is small and thus corresponds to the more octahedral environment.

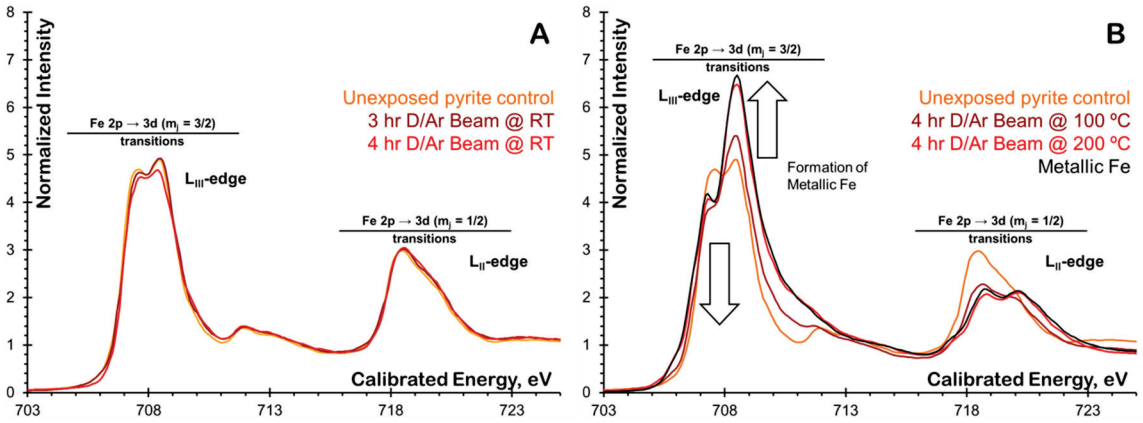

Figure 6.3. Fe L-edge X-ray absorption near-edge spectra collected in electron yield mode for pyrite (100) exposed to the D-atom beam for various times at (A) room and (B) elevated temperatures at an exposure time of 4 hr. (B) contains a reference metallic iron

Figure 6.3 summarizes the Fe L-edge data collected in electron yield detection mode for pyrite (100) surfaces as a function of exposure time (Figure 6.3A) and surface temperature (Figure 6.3B) at constant room temperature and 4 hour exposure time,

respectively. The slight variations in the peak intensity in Figure 6.3A are result of data collection, background correction, and normalization. Due to the close proximity of the edges and the sensitivity to beamline configurations, the Fe L-edge can be challenging to normalize. Regardless of the difficulties in data normalization, in Figure 6.3B, more dramatic changes are observed when the temperature is varied compared to exposure time at room temperature (Figure 6.3A). These spectra conclusively show a complete change in the splitting and shift of both edges towards a reduced iron phase (using metallic iron(0) as a reference). Because electron yield is a surface sensitive detection method (approximately a few nm escape depth[70]), this confirms the Fe K-edge analysis and shows the top layer is a reduced metallic iron(0). Since all data samples were exposed to air before XAS measurements including reference metallic iron, we anticipate a thin passivating layer of iron oxide.

S K-edge Results

To further investigate the modified pyrite surface, we carried out X-ray absorption spectroscopy at the S K-edge using fluorescence and partial electron yield detection. Figure 6.4 summarizes several structurally well-defined reference compounds of sulfides and iron sulfides. The inset in Figure 6.4 illustrates the origin of the spectral features as the electric dipole allowed transition of S 1s electrons to unoccupied S 3p and 4p based states corresponding to the pre-edge and rising-edge features, respectively. The rising-edge feature is directly related to the S effective nuclear charges seen by donor and acceptor orbitals for a given excitation, and thus, the rising-edge of more oxidized HS^- and S_2^{2-} compounds shifts to higher energies relative to the more reduced S^{2-}

compounds. Electron donation of the sulfur has a large effect on the effective oxidation state and thus rising-edge. The difference between formal and effective oxidation state of the S atoms can be demonstrated by the rising-edge position of the formally HS^- sodium hydrosulfide (2473.9 eV) and the formally S^{2-} troilite rising-edge position (2474.4 eV). Due to the presence of the metal-ligand bond in troilite, the S atoms can donate more electron density to the Fe sites compared to the hydrogen in sodium hydrosulfide, and thus, the sulfur is effectively more oxidized as seen by the higher rising-edge position of 2474.4 eV. The same trend is valid for comparing the formally S^{2-} sodium sulfide and troilite rising-edge positions with the change that sodium sulfide has only limited donation to the Na^+ ions, and thus it is the most reduced S compound in Figure 6.4.

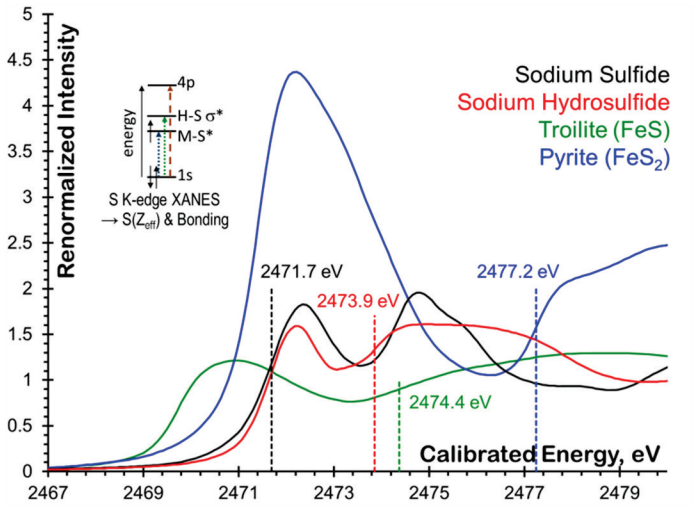

Figure 6.4. Reference S K-edge X-ray absorption near-edge spectra of reference iron sulfides

Due to the localized nature of the S 1s orbital, the intensity of the pre-edge is directly related to the amount of S 3p character in the bonding molecular orbital. The pyrite pre-edge feature is a result of the metal-ligand and the S-S bond. The troilite pre-

edge feature is a result of only the metal-ligand bond. Although it seems that the pyrite has more 3p character than the troilite, we know from the Fe K-edge that the troilite donates more to the Fe sites than pyrite. Thus, the increased pre-edge feature intensity is due to the presences of the vacant S-S antibonding orbital.

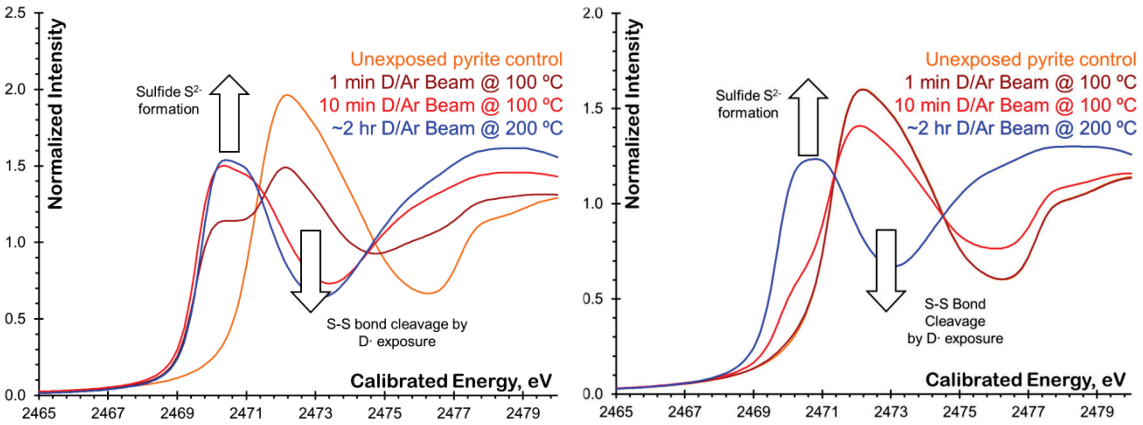

Figure 6.5. S K-edge X-ray absorption near-edge spectra collected in (A) electron yield and (B) fluorescence yield mode for pyrite (100) exposed to the D-atom beam for various times and elevated temperatures

Figure 6.5 summarizes the XANES data collected in partial electron (Figure 6.5A) and fluorescence detection (Figure 6.5B) for pyrite (100) as function of exposure time at constant temperature. Both detection methods show dramatic changes in the pre-edge intensity and rising-edge position. The shift in rising-edge position to a lower energy position suggests that the S atoms are being reduced. This corresponds to the surface sulfur depletion shown with the molecular beam experiment. The persulfide bond is broken, leaving behind a sulfide. The considerable difference between the partial electron yield and fluorescence detection is a result of probing different depths. The partial electron yield detection shows a rapid conversion of the surface sulfur from

persulfide to sulfide compared to the fluorescence detection. Comparing the spectra after 10 minute exposure, the surface is nearly completely converted to the sulfide while the interface is still gradually changing. From the Fe K- and L-edge, it was shown that the surface of the 2 hour exposure at 200°C was metallic iron that was converted to a passivating layer of iron oxide from exposure to the ambient atmosphere. Furthermore, the molecular beam experiment showed a depletion of accessible sulfur. Therefore, the surface detection technique (partial electron yield) must be detecting inaccessible surface sulfurs and/or sulfurs just below the metallic iron layer. The comparison of the ~2 hour exposure time of the partial electron yield (Figure 6.5A) and fluorescence detection (Figure 6.5A) indicates that the sulfide pre-edge feature is the result of two peaks. From the partial electron detection (Figure 6.5A), the first feature is more intense, indicating more 3p character in the iron-sulfur antibonding orbital or more sulfurs in that environment than in the second feature. The higher energy corresponds to a more oxidized iron center which results in better overlap. These features decrease at the lower layer (fluorescence detection), suggesting a decrease in oxidized iron centers. The rising-edge of the fluorescence is also shifted slightly lower in energy (~0.3 eV), further supporting the decrease in oxidized iron centers below the surface.

Conclusion

From multi-edge X-ray absorption spectroscopic measurements, we have confirmed that a pyrite surface reacts with deuterium (or hydrogen) atoms to produce a metallic iron rich surface, and the intermediate layer beneath this top layer and above the

bulk pyrite contains a previously unknown reduced Fe-S phase, which tentatively was assigned as amorphous $Fe(I)_2S$.

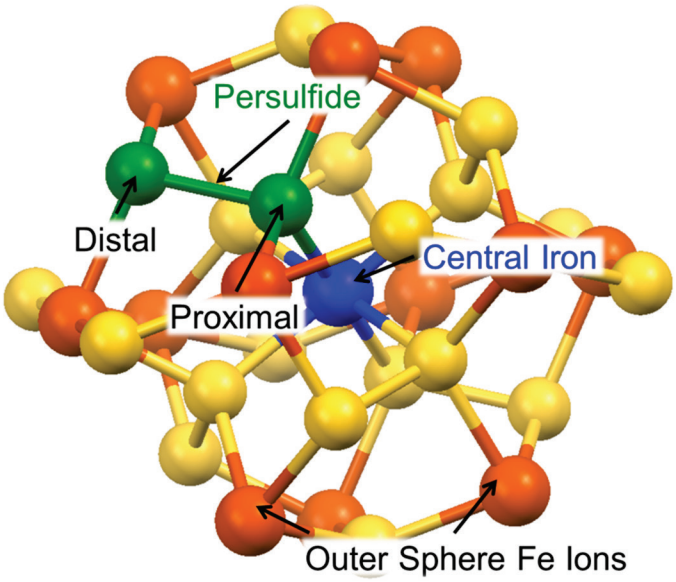

Figure 6.6. Model of the pyrite crystal centered on a single iron with the first coordinate shell

On the basis of all the previously discussed experimental results in both Chapters 5 and 6, we propose a chemical reaction scheme based upon a sequence of electron and proton transfer events that lead to the formation of sulfides (Figure 6.7) from S K-edge XAS and metallic iron (Figure 6.8) from Fe K- and L-edge XAS. The reaction scheme was constructed on the basis that the incoming deuterium (or hydrogen) atom can attack the pristine pyrite surface at either the metal or ligand, taking into account various intramolecular electron- and proton-transfer pathways. Figure 6.6 shows the surface environment of pyrite. Each surface iron atom is surrounded by 3-4 sulfur atoms depending on surface structure. Each surface sulfur atom is surrounded by 2-3 iron atoms and a sulfur atom. Thus, each distal sulfur is a proximal sulfur to another iron. Therefore,

the movement of the deuterium (or hydrogen) atom would be to an adjacent iron or sulfur atom, and not across several bonds.

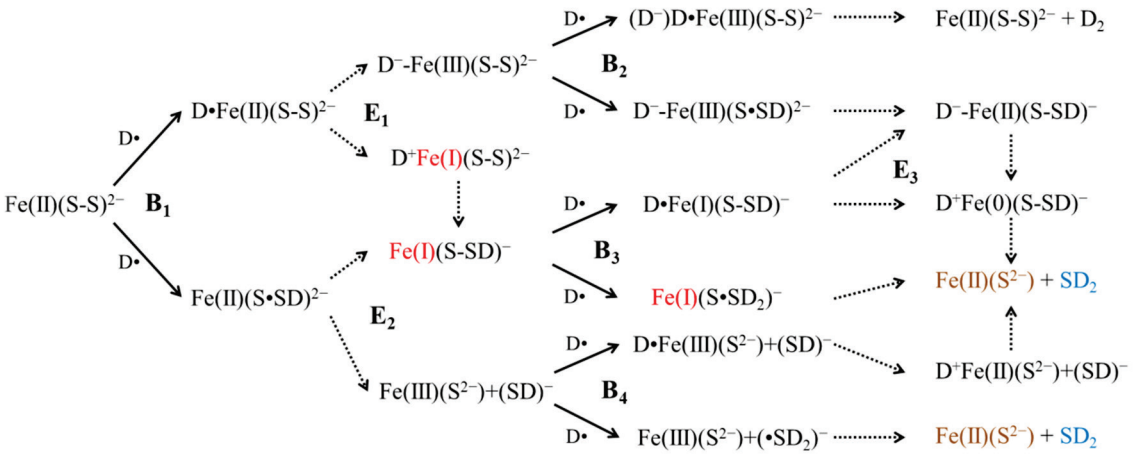

Figure 6.7. The proposed reaction scheme for the first step, breaking the persulfide bond. The branching for each incoming D atom is a result of the two possible binding modes (B) and the concomitant electron transfer processes (E). The species seen in the beam scattering experiment are colored blue, in S K-edge X-ray absorption measurements are colored brown, and in the Fe K-edge seen in red

In Figure 6.7, the first incoming D atom (B_1) could either bind to the iron or the persulfide. The reaction at a formally Fe(II) site could form (E_1) either a D^- (hydride) ligand bound to Fe(III) or D^+ ion and Fe(I). The hydride is less likely because the arrival of the second D atom (B_2) will likely form D_2 instead of the product D_2S. The D^+ ion will migrate to a nearby sulfur atom, leaving its electron behind and reducing the Fe site, forming a persulfhydryl ligand. In the case of the D atom binding to the sulfur site forming S_2D^{2-} radical anion, the relaxation (E_2) would result in either the reduction of the iron site or oxidation of the iron site, breaking the persulfide bond and forming sulfide and sulfhydryl ligands. The arrival of the second D atom could react with either the

oxidized or reduced iron species. The reaction with the iron site of the reduced iron species (B_3) could form either (E_3) a hydride ligand bound to a Fe(II) or D^+ ion and Fe(0). The hydride is unlikely due its relaxation back to the D^+ ion. The D^+ ion will migrate to a neighboring sulfur atom, and if it is a persulfhydryl, then it could form the experimentally detected D_2S and Fe(II)S. The latter Fe-S phase has been detected in S K-edge XAS. The reaction with the oxidized iron species (B_4) would result in the same outcome: D_2S seen in molecular beam experiments and Fe(II)S seen in S K-edge XAS. Furthermore, the Fe(I) species seen in the Fe K-edge XAS is stabilized at any given point in the mechanism because of the surround sulfurs (seen Figure 6.6).

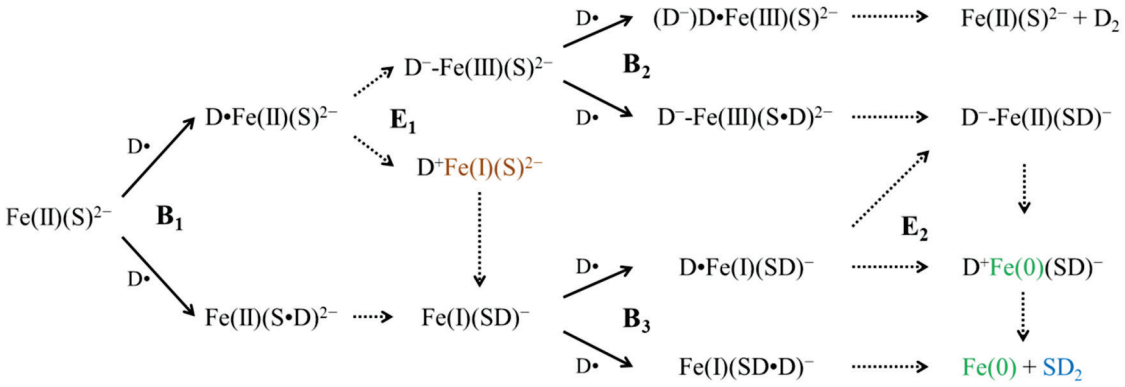

Figure 6.8. The proposed reaction scheme for the second step, formation of metallic iron. The branching for each incoming D atom is a result of the two possible binding modes (B) and the concomitant electron transfer processes (E). The species seen in the beam scattering experiment are colored blue, in Fe and S K-edge X-ray absorption measurements are colored brown, and in the Fe K and L-edge seen in green

In Figure 6.8, the first incoming D atom could either bind to the iron or the sulfide (B_1). The reaction (E_1) at the formally Fe(II) could result in the formation of a hydride ligand bond to Fe(III) or D^+ ion and Fe(I). The D^+ ion is the most likely path due to the

formation of Fe(I) that is seen in both the Fe and S K-edge XANES. The D^+ ion will migrate to a neighboring sulfur atom to form sulfhydryl. Upon arrival of the second D atom (B_3), the Fe(I) can be reduced to a formally Fe(0) through either binding site, resulting in the observed D_2S and metallic iron surface. The oxidation of the Fe(I) with the reaction with the second D atom (E_2) would likely be short lived and relax back to the Fe(0).

The above preliminary mechanistic proposal in Figure 6.7 and Figure 6.8 can be probed computationally. A computational model of the active site similar to Figure 6.6 can be built to model the pyrite (100) surfaces. Then, each proposed site in Figure 6.7 and Figure 6.8 could be modeled to determine their stability and thus determine the most likely reaction path to form the unique Fe(I) species. Initial model building has been done and already demonstrated the applicability for a nitrogen oxide binding study with collaborators Schoonen and Strongin.[206]

CHAPTER 7

CONCLUSION

Iron-sulfur systems are ubiquitous in biological and geological environments. They range from molecular scale [2Fe-2S] clusters to nanometer scale particles to micrometer scale minerals. Across the length scale, each system has a unique effect on its biological or geological environment, from simple electron transfer in proteins to the production of acid and release of heavy metals. Therefore, understanding the electronic and geometric structural properties that give a wide range of reactivity is of great interest. The goal of this work is to gain an understanding into the relationship between the system size and properties by bridging the different size scales with a single technique, X-ray absorption spectroscopy.

X-ray absorption spectroscopy is a powerful technique to probe the electronic and geometric structural information for a wide range of transition metal systems with a partially occupied d- or f-manifold. From EXAFS, geometric structural information of non-crystalline materials, such as protein iron-sulfur systems and amorphous nanometer scale iron-sulfur systems, can be determined. Multi-edge XANES analysis provides electronic structural information through complementary information from different absorption edges. Different experimental detection methods allow for probing different depths of layered systems. Thus, electronic and geometric information of different layers can be determined. From this technique, we are able to develop a comprehensive picture

of both the electronic and geometric structures of each of the different sized iron-sulfur systems from small (molecular) [4Fe-4S] clusters to large (micrometer) minerals.

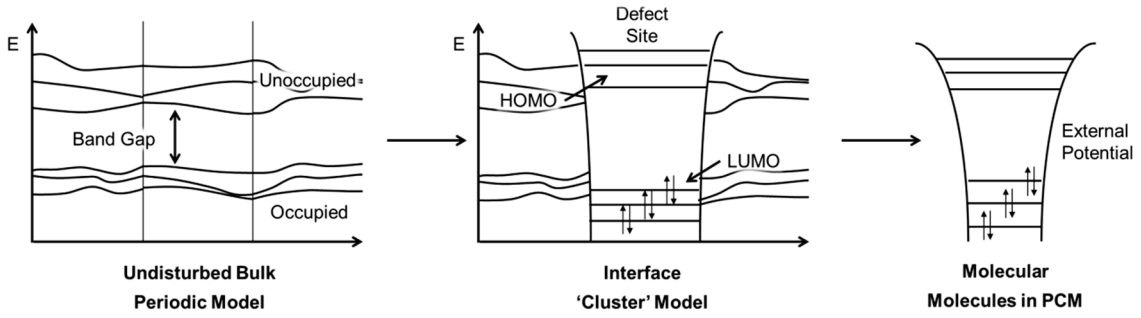

Figure 7.1. Our model for change in electronic structure as the geometry and size of the systems is change

The overarching theme investigated in this work was whether there is a distinct separation among the electronic structures across the full length scale of iron-sulfur systems. Much of our understanding of this question was developed during the study of the nanometer scale particles and micrometer scale mineral surfaces (Chapters 4-6). Figure 7.1 summarizes our thinking by presenting a model for the change in electronic structure across the full length scale. This model indicates that we consider a continuum in going from periodic bulk systems, through surfaces that are embedded into or supported by the bulk phase, to non-periodic molecular systems with well-defined composition, electronic and geometric structures. The bulk minerals can be regarded as well-order periodic materials and are modeled with band structure theory. Upon breaking this periodicity, such as considering the surface and/or defect sites, the electronic structure deviates from the band structure model and begins to appear more like a molecular orbital-based bonding model. Depending on the size and nature of the defect

size, we envision the manifestation of the localization of electronic structure in molecular geometry by changing metal-ligand bonding, forming more localized cluster of interactions than in the bulk. But as the figure illustrates, there is still some overlap between the two models. We use this image to demonstrate a gradient change in the electronic structure and consequently the geometry as seen from the presence of a stable interfacial layer for the D beam exposed pyrite surface as indicated in Chapters 5 and 6. We propose that this can be modeled as a large cluster of atoms that has inner sphere of bulk-like properties. From the Fe K-edge analysis, we showed that a reduced iron-sulfur phase was produced from the reaction with deuterium atoms. Combined with the S K-edge analysis, the proposed reaction scheme suggests a gradient change in the iron oxidation state from a formally Fe(II) through Fe(I) to Fe(0). This analysis of the gradient change in phases is supported on the nanometer scale particles (Chapter 4). The S K-edge with fluorescence detection, which probes a few tens of nanometers, suggested a mixture of the phases and likely a gradient from the core to the surface of the particles. Upon separation of the disordered structure of the surface or defect site to a signal cluster, the electronic structure can be then modeled with molecular orbital theory and the bulk environment modeled with a polarized continuum model (PCM) to represent the electrostatic perturbation with steric constraints for the boundary atoms. Thus, a comparison across the full length scale of iron-sulfur systems provides rationalization and predictions for how these iron-sulfur systems can fill in various structural and/or catalytic roles.

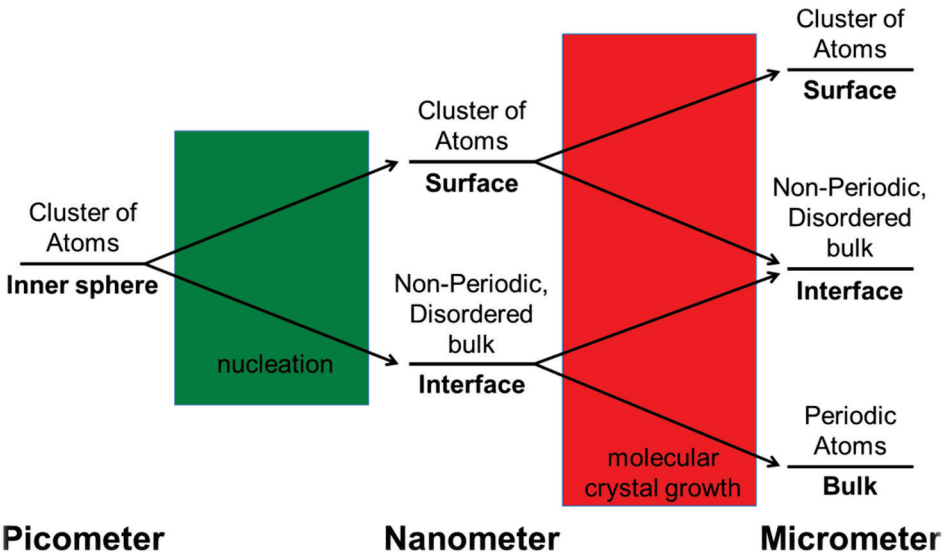

Figure 7.2. A scheme of the change in size of systems

From these insights, we can develop a scheme to describe the change across the full length scale of iron-sulfur systems studied in this work (Figure 7.2). At the molecular scale, iron-sulfur systems can be treated as clusters of atoms that are ordered according to ionic, covalent, and magnetic interactions. Depending on the size of the system, we can distinguish among inner sphere atoms that are directly coordinated or covalently bound to a central ion or cluster of ions or atoms, or second coordination sphere, or outer sphere atoms that are responsible for electrostatic polarization, steric constrains, and limited electronic tuning of the inner sphere.

The interface would be a non-periodic, distorted bulk transitioning between the surface and the bulk. The observed reduced Fe-S interfacial phase from Chapters 5 and 6 is an example of this transition between the bulk pyrite and the surface oxidized metallic iron. This remarkable reduced layer indicates that there can be somewhat of an independent reactive system under the surface of a mineral that we would best

approximate with how the core of the nanometer size particles may behave. Although we do not have the full data set yet for the particle size regime, from the discussion of spectral features so far, we anticipate spectral signatures that are characteristic to the interfacial layer of bulk pyrite. Thus, the interface's unique properties may be accessed through controlled synthesis such as the biomineralization in protein cages as seen for iron-sulfur precipitates.

The studies presented in this dissertation have provided insights into the full length scale of iron-sulfur systems. We have demonstrated the potential of X-ray absorption spectroscopy to provide new insights into the electronic and geometric structure of the full length scale of iron-sulfur systems. Furthermore, we provided a model of the full length scale of iron-sulfur systems and laid the foundation for developing a computational model that can describe the changes seen for pyrite at the atomic scale. As stated in Chapter 6, initial modeling has already been done, and the use of the models has been demonstrated for modeling nitrogen oxide binding and simulating corresponding IR signatures. These computation models have the potential to provide new directions in developing novel iron-sulfur systems that have reactivity similar to biological catalytically active sites such as the H-cluster of [FeFe]- hydrogenase[26] and FeMo-co of nitrogenase.[23]

Future Directions in Data Processing and Analysis

Data Processing (ADRP)

One of the important aspects of studying XAS is assuring that the data reduction is systematic, quantitative, and reproducible. Thus as a first step, I have programed an XAS normalization procedure named Automated Data Reduction Protocol (ADRP) implemented in Excel. This procedure is based upon established protocols for data reduction and normalization.[69] ADRP calibrates, averages, calculates background, and normalizes any number of XAS scans. Calibration is an important step due to changes in beamline, optics, monochromators, and variations in the motor steps among beamlines and beam times. Fitting the background is a crucial step in data reduction, because it corrects for data collected at different temperatures (RT, Liquid N_2, and Liquid He), beam currents, and detection methods. This step directly affects the normalization. Normalization corrects the spectra for different sample concentrations and allows for direct comparison of different spectra and quantitative fitting.

Furthermore, an important aspect of data reduction is determining the background of the XANES. The error bars in obtaining metal-ligand covalency from data reduction are generally 5-7% for ligand K-edge, which gets much worse (10-15%) for the L-edge. Thus, a further objective will be extending the functionality of ADRP in determining the background to a more robust background calculation to cover L-edges. One possible solution is using progressively improved fits to the pre-edge, rising-edge, and edge jump for both L_{III}- and L_{II}-edges to iteratively find the background. Another possible solution is using higher order polynomials to take into account the overlapping edge-jumps of L_{III}-

and L_{II}-edges. An example of the latter was recently formulated by Kennepohl and coworkers.[207] The analytical formula for fitting *n*-order has already been derived using matrix algebra, and could implement this into ADRP. Alternatively, all the above background subtraction methodologies could be implemented and allow for users take a linear combination of these methodologies and find the most appreciable option for a given problem. The current implementation with test files and stepwise tutorial is available at http://computational.chemistry.montana.edu/ADRP.

Development of Multi-Edge EXAFS Analysis

A recent development is the extension of EXAFS analysis to simultaneous analysis of multiple absorbers. The Extended X-ray Absorption Fine Structure (EXAFS) analysis is the most frequently employed method for extracting structural information from X-ray absorption spectroscopic data.[208] A serious limitation of the EXAFS method is its chemical model dependence. One needs to have a reasonable structural model for fitting the set of scattering distances, amplitudes and phases. Even with using a reasonable model, the geometric information is limited to radial distribution of atoms around a central absorber. Multi-edge X-ray absorption spectroscopic (XAS) approach for coordination compounds has an unexplored potential in obtaining complete both electronic and geometric structures. Data collection at the metal and ligand atoms K-edges in the hard (for transition metals), tender (for P, S, Cl), and soft (for C, O, N) X-ray energy ranges has the potential to give information about EXAFS scattering pathway from both ends. Thus, a simultaneous analysis of EXAFS data obtained for various absorbers fortuitously over-defines the EXAFS equation and has a potential for

eliminating structural uncertainties, as well as reducing the complexity of the fitting procedure. In addition to obtaining reduced model dependence of the interpretation of EXAFS fits, there is a possibility for determining atomic coordinates for the absorbers and surrounding atoms due to the complementary radial distances among absorbers.

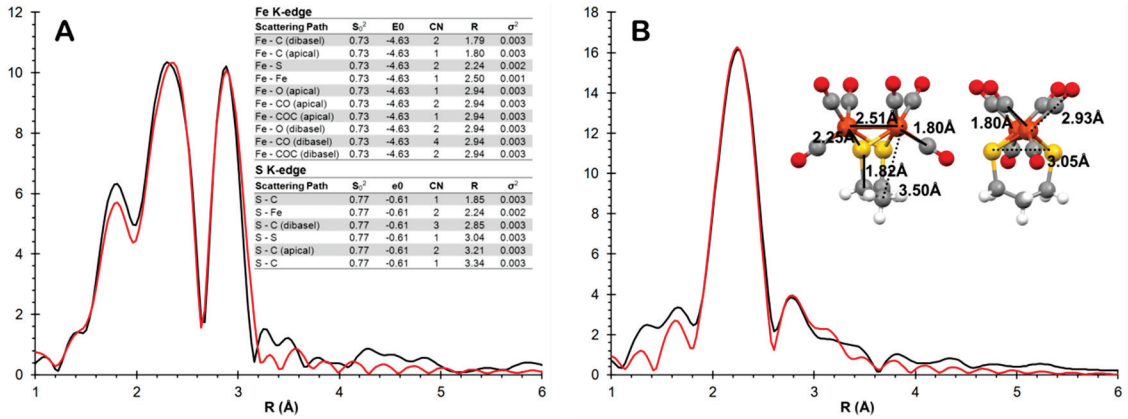

Fe K-edge

Scattering Path	S_0^2	E0	CN	R	σ^2
Fe - C (dibasel)	0.73	-4.63	2	1.79	0.003
Fe - C (apical)	0.73	-4.63	1	1.80	0.003
Fe - S	0.73	-4.63	2	2.24	0.002
Fe - Fe	0.73	-4.63	1	2.50	0.001
Fe - O (apical)	0.73	-4.63	1	2.94	0.003
Fe - CO (apical)	0.73	-4.63	2	2.94	0.003
Fe - COC (apical)	0.73	-4.63	1	2.94	0.003
Fe - O (dibasel)	0.73	-4.63	2	2.94	0.003
Fe - CO (dibasel)	0.73	-4.63	4	2.94	0.003
Fe - COC (dibasel)	0.73	-4.63	2	2.94	0.003

S K-edge

Scattering Path	S_0^2	e0	CN	R	σ^2
S - C	0.77	-0.61	1	1.85	0.003
S - Fe	0.77	-0.61	2	2.24	0.002
S - C (dibasel)	0.77	-0.61	3	2.85	0.003
S - S	0.77	-0.61	1	3.04	0.003
S - C (apical)	0.77	-0.61	2	3.21	0.003
S - C	0.77	-0.61	1	3.34	0.003

Figure 7.3. Fourier Transform of (A) Fe K- and (B) S K-edges EXAFS of $Fe_2(pdt)(CO)_6$ and representative fits from simultaneous analysis with crystal structure[30]

To validate the robustness and accuracy of the method, the multi-edge EXAFS analysis was performed on two synthetic analogues of the [2Fe]-subcluster of the FeFe-hydrogenase, $Fe_2(pdt)(CO)_6$ and $Fe_2S_2(CO)_6$. Both models have well-defined crystal structures and are well characterized by numerous spectroscopic methods; thus they are ideal for method development. The theoretical phase and amplitudes were calculated with FEFF 8.4,[97, 98] and fitting was done in IFFEFIT v1.2.11c.[95] In order to evaluate the benefit of multi-edge EXAFS analysis, both separated and combined fitting procedures were carried out. The most reasonable fitting was obtained by linking the single and multiple scattering pathways present at both Fe and S EXAFS. Figure 7.3 shows the Fourier Transform data in R-space for the simultaneous fitting of the Fe and S EXAFS

for $Fe_2(pdt)(CO)_6$. Using trigonometry, the positional coordinates of the absorbers were determined assuming a symmetrical [2Fe-2S] core (C_{2v} point group). From these preliminary results, I can envision great potential for applying this method to biomimetic organometallic catalysis and mineral and particle surfaces. Obviously, due to the large C, N, and O background the multi-edge EXAFS is not applicable for light atom coordination and would only have limited use in proteins, but could advance the field of homogeneous organic and organometallic chemistry.

REFERENCES CITED

1. Lowson, R. T., Aqueous Oxidation of Pyrite by Molecular-Oxygen. *Chemical Reviews* **1982,** 82, (5), 461-497.

2. Rickard, D.; Luther, G. W., III, Chemistry of iron sulfides. *Chemical Reviews* **2007,** 107, (2), 514-562.

3. Singer, P. C.; Stumm, W., Direct Oxidation by Adosrbed Oxygen During Acidic Mine Drainage. *Science* **1970,** 169, (3940), 98-&.

4. Smart, R.; Amarantidis, J.; Skinner, W.; Prestidge, C.; La Vanier, L.; Grano, S.; Wandelt, K.; Thurgate, S., Surface Analytical Studies of Oxidation and Collector Adsorption in Sulfide Mineral Flotation Solid—Liquid Interfaces. In Springer Berlin / Heidelberg: 2003; Vol. 85, pp 3-62.

5. Borda, M. J.; Elsetinow, A. R.; Strongin, D. R.; Schoonen, M. A., A mechanism for the production of hydroxyl radical at surface defect sites on pyrite. *Geochimica Et Cosmochimica Acta* **2003,** 67, (5), 935-939.

6. Parkman, R. H.; Charnock, J. M.; Bryan, N. D.; Livens, F. R.; Vaughan, D. J., Reactions of copper and cadmium ions in aqueous solution with goethite, lepidocrocite, mackinawite, and pyrite. *American Mineralogist* **1999,** 84, (3), 407-419.

7. Morse, J. W.; Millero, F. J.; Cornwell, J. C.; Rickard, D., The Chemistry of the Hydrogen-Sulfide and Iron Sulfide Systems in Natural-Waters. *Earth-Science Reviews* **1987,** 24, (1), 1-42.

8. Douglas, T.; Dickson, D. P. E.; Betteridge, S.; Charnock, J.; Garner, C. D.; Mann, S., Synthesis and Structure of an Iron(III) Sulfide-Ferritin Bioinorganic Nanocomposite. *Science* **1995,** 269, (5220), 54-57.

9. Rao, P. V.; Holm, R. H., Synthetic analogues of the active sites of iron-sulfur proteins. *Chemical Reviews* **2004,** 104, (2), 527-559.

10. Beinert, H.; Holm, R. H.; Munck, E., Iron-sulfur clusters: Nature's modular, multipurpose structures. *Science* **1997,** 277, (5326), 653-659.

11. Holm, R. H.; Kennepohl, P.; Solomon, E. I., Structural and functional aspects of metal sites in biology. *Chemical Reviews* **1996,** 96, (7), 2239-2314.

12. Binda, C.; Coda, A.; Aliverti, A.; Zanetti, G.; Mattevi, A., Structure of the mutant E92K of [2Fe-2S] ferredoxin I from *Spinacia oleracea* at 1.7 angstrom resolution.

Acta Crystallographica Section D-Biological Crystallography **1998,** 54, 1353-1358.

13. Jang, S. B.; Seefeldt, L. C.; Peters, J. W., Insights into nucleotide signal transduction in nitrogenase: Protein with MgADP bound. *Biochemistry* **2000,** 39, (48), 14745-14752.

14. Stout, G. H.; Turley, S.; Sieker, L. C.; Jensen, L. H., Structure of Ferredoxin-I from *Azotobacter-Vinelandii*. *Proceedings of the National Academy of Sciences of the United States of America* **1988,** 85, (4), 1020-1022.

15. Doukov, T. I.; Iverson, T. M.; Seravalli, J.; Ragsdale, S. W.; Drennan, C. L., A Ni-Fe-Cu center in a bifunctional carbon monoxide dehydrogenase/acetyl-CoA synthase. *Science* **2002,** 298, (5593), 567-572.

16. Einsle, O.; Tezcan, F. A.; Andrade, S. L. A.; Schmid, B.; Yoshida, M.; Howard, J. B.; Rees, D. C., Nitrogenase MoFe-protein at 1.16 angstrom resolution: A central ligand in the FeMo-cofactor. *Science* **2002,** 297, (5587), 1696-1700.

17. Nicolet, Y.; Piras, C.; Legrand, P.; Hatchikian, C. E.; Fontecilla-Camps, J. C., *Desulfovibrio desulfuricans* iron hydrogenase: the structure shows unusual coordination to an active site Fe binuclear center. *Structure with Folding & Design* **1999,** 7, (1), 13-23.

18. Peters, J. W.; Lanzilotta, W. N.; Lemon, B. J.; Seefeldt, L. C., X-ray crystal structure of the Fe-only hydrogenase (Cpl) from *Clostridium pasteurianum* to 1.8 angstrom resolution. *Science* **1998,** 282, (5395), 1853-1858.

19. Berkovitch, F.; Nicolet, Y.; Wan, J. T.; Jarrett, J. T.; Drennan, C. L., Crystal structure of biotin synthase, an S-adenosylmethionine dependent radical enzyme. *Science* **2004,** 303, 76-79.

20. Lukianova, O. A.; David, S. S., A role for iron-sulfur clusters in DNA repair. *Current Opinion in Chemical Biology* **2005,** 9, (2), 145-151.

21. Kiley, P. J.; Beinert, H., The role of Fe-S proteins in sensing and regulation in bacteria. *Current Opinion in Microbiology* **2003,** 6, (2), 181-185.

22. Sticht, H.; Rosch, P., The structure of iron-sulfur proteins. *Progress in Biophysics & Molecular Biology* **1998,** 70, (2), 95-136.

23. Igarashi, R. Y.; Seefeldt, L. C., Nitrogen fixation: The mechanism of the Mo-dependent nitrogenase. *Critical Reviews in Biochemistry and Molecular Biology* **2003,** 38, (4), 351-384.

24. Moura, J. J. G.; Moura, I.; Kent, T. A.; Lipscomb, J. D.; Huynh, B. H.; Legall, J.; Xavier, A. V.; Munck, E., Interconversions of [3Fe-3S] and [4Fe-4S] Clusters - Mössbauer and Electron-Paramagnetic Resonance Studies of Desulfovibrio-Gigas Ferredoxin-II. *Journal of Biological Chemistry* **1982,** 257, (11), 6259-6267.

25. Frey, P. A.; Hegeman, A. D.; Ruzicka, F. J., The radical SAM superfamily. *Critical Reviews in Biochemistry and Molecular Biology* **2008,** 43, (1), 63-88.

26. Vignais, P. M.; Billoud, B.; Meyer, J., Classification and phylogeny of hydrogenases. *Fems Microbiology Reviews* **2001,** 25, (4), 455-501.

27. Hatchikian, E. C.; Forget, N.; Fernandez, V. M.; Williams, R.; Cammack, R., Further Characterization of the [Fe]-Hydrogenase from *Desulfovibrio-Desulfuricans* Atcc-7757. *European Journal of Biochemistry* **1992,** 209, (1), 357-365.

28. Mulder, D. W.; Shepard, E. M.; Meuser, J. E.; Joshi, N.; King, P. W.; Posewitz, M. C.; Broderick, J. B.; Peters, J. W., Insights into [FeFe]-Hydrogenase Structure, Mechanism, and Maturation. *Structure* **2011,** 19, (8), 1038-1052.

29. Shepard, E. M.; Boyd, E. S.; Broderick, J. B.; Peters, J. W., Biosynthesis of complex iron-sulfur enzymes. *Current Opinion in Chemical Biology* **2011,** 15, (2), 319-327.

30. Lyon, E. J.; Georgakaki, I. P.; Reibenspies, J. H.; Darensbourg, M. Y., Carbon monoxide and cyanide ligands in a classical organometallic complex model for Fe-only hydrogenase. *Angewandte Chemie-International Edition* **1999,** 38, (21), 3178-3180.

31. Averill, B. A.; Herskovi.T; Holm, R. H.; Ibers, J. A., Synthetic Analogs of Active-Sites of Iron-Sulfur Proteins .2. Synthesis and Structure of Tetra[Mercapto-Mu3-Sulfido-Iron] Clusters, $[Fe_4S_4(SR)_4]^{2-}$. *Journal of the American Chemical Society* **1973,** 95, (11), 3523-3534.

32. Zhou, J.; Hu, Z. G.; Munck, E.; Holm, R. H., The cuboidal Fe3S4 cluster: Synthesis, stability, and geometric and electronic structures in a non-protein environment. *Journal of the American Chemical Society* **1996,** 118, (8), 1966-1980.

33. Han, J.; Koutmos, M.; Al Ahmad, S.; Coucouvanis, D., Rational synthesis of high nuclearity Mo/Fe/S clusters: The reductive coupling approach in the convenient synthesis of $(Cl_4\text{-cat})_2Mo_2Fe_6S_8(PR_3)_6$ [R = Et, ^{n}Pr, ^{n}Bu] and the new $[(Cl_4\text{-cat})_2Mo_2Fe_2S_3O(PEt_3)_3Cl]$ $1/2(Fe(PEt_3)_2(MeCN)_4)$ and $(Cl_4\text{-cat})_2Mo_2Fe_3S_5(PEt_3)_5$ Clusters. *Inorganic Chemistry* **2001,** 40, (23), 5985-5999.

34. Coldren, C. D.; Hellinga, H. W.; Caradonna, J. P., The rational design and construction of a cuboidal iron-sulfur protein. *Proceedings of the National Academy of Sciences of the United States of America* **1997,** 94, (13), 6635-6640.

35. Stephens, P. J.; Jollie, D. R.; Warshel, A., Protein control of redox potentials of iron-sulfur proteins. *Chemical Reviews* **1996,** 96, (7), 2491-2513.

36. Swartz, P. D.; Beck, B. W.; Ichiye, T., Structural origins of redox potentials in Fe-S proteins: Electrostatic potentials of crystal structures. *Biophysical Journal* **1996,** 71, (6), 2958-2969.

37. Depamphi.Bv; Averill, B. A.; Herskovi.T; Que, L.; Holm, R. H., Synthetic Analogs of Active-Sites of Iron-Sulfur Proteins .6. Spectral and Redox Characteristics of Tetranuclear Clusters $[Fe_4S_4(SR)_4]^{2-}$. *Journal of the American Chemical Society* **1974,** 96, (13), 4159-4167.

38. Beinert, H., Iron-sulfur proteins: ancient structures, still full of surprises. *Journal of Biological Inorganic Chemistry* **2000,** 5, (1), 2-15.

39. Adman, E.; Watenpaugh, K. D.; Jensen, L. H., Nh...S Hydrogen-Bonds in *Peptococcus Aerogenes* Ferredoxin, *Clostridium Pasteurianum* Rubredoxin, and Chromatium High Potential Iron Protein. *Proceedings of the National Academy of Sciences of the United States of America* **1975,** 72, (12), 4854-4858.

40. Backes, G.; Mino, Y.; Loehr, T. M.; Meyer, T. E.; Cusanovich, M. A.; Sweeney, W. V.; Adman, E. T.; Sandersloehr, J., The Environment of Fe4s4 Clusters in Ferredoxins and High-Potential Iron Proteins - New Information from X-Ray Crystallography and Resonance Raman-Spectroscopy. *Journal of the American Chemical Society* **1991,** 113, (6), 2055-2064.

41. Banci, L.; Bertini, I.; Savellini, G. G.; Luchinat, C., Individual reduction potentials of the iron ions in Fe_2S_2 and high-potential Fe_4S_4 ferredoxins. *Inorganic Chemistry* **1996,** 35, (14), 4248-4253.

42. Chen, K. S.; Tilley, G. J.; Sridhar, V.; Prasad, G. S.; Stout, C. D.; Armstrong, F. A.; Burgess, B. K., Alteration of the reduction potential of the $[4Fe\text{-}4S]^{2+/+}$ cluster of Azotobacter vinelandii ferredoxin I. *Journal of Biological Chemistry* **1999,** 274, (51), 36479-36487.

43. Eidsness, M. K.; Burden, A. E.; Richie, K. A.; Kurtz, D. M.; Scott, R. A.; Smith, E. T.; Ichiye, T.; Beard, B.; Min, T. P.; Kang, C. H., Modulation of the redox potential of the $[Fe(SCys)_4]$ site in rubredoxin by the orientation of a peptide dipole. *Biochemistry* **1999,** 38, (45), 14803-14809.

44. Niu, S.; Ichiye, T., Insight into Environmental Effects on Bonding and Redox Properties of [4Fe-4S] Clusters in Proteins. *Journal of the American Chemical Society* **2009,** 131, (16), 5724-+.

45. Beinert, H.; Kennedy, M. C.; Stout, C. D., Aconitase as iron-sulfur protein, enzyme, and iron-regulatory protein. *Chemical Reviews* **1996,** 96, (7), 2335-2373.

46. Yücel, M.; Gartman, A.; Chan, C. S.; Luther, G. W., III, Hydrothermal vents as a kinetically stable source of iron-sulphide-bearing nanoparticles to the ocean. *Nature Geoscience* **2011,** 4, (6), 367-371.

47. Kim, E.-J.; Kim, J.-H.; Azad, A.-M.; Chang, Y.-S., Facile Synthesis and Characterization of Fe/FeS Nanoparticles for Environmental Applications. *Acs Applied Materials & Interfaces* **2011,** 3, (5), 1457-1462.

48. Chang, Y.-S.; Savitha, S.; Sadhasivam, S.; Hsu, C.-K.; Lin, F.-H., Fabrication, characterization, and application of greigite nanoparticles for cancer hyperthermia. *Journal of Colloid and Interface Science* **2011,** 363, (1), 314-319.

49. Butler, E. C.; Hayes, K. F., Factors influencing rates and products in the transformation of trichloroethylene by iron sulfide and iron metal. *Environmental Science & Technology* **2001,** 35, (19), 3884-3891.

50. Butler, E. C.; Hayes, K. F., Kinetics of the transformation of trichloroethylene and tetrachloroethylene by iron sulfide. *Environmental Science & Technology* **1999,** 33, (12), 2021-2027.

51. Watson, J. H. P.; Cressey, B. A.; Roberts, A. P.; Ellwood, D. C.; Charnock, J. M.; Soper, A. K., Structural and magnetic studies on heavy-metal-adsorbing iron sulphide nanoparticles produced by sulphate-reducing bacteria. *Journal of Magnetism and Magnetic Materials* **2000,** 214, (1-2), 13-30.

52. Bi, X. X.; Ganguly, B.; Huffman, G. P.; Huggins, F. E.; Endo, M.; Eklund, P. C., Nanocrystalline Alpha-Fe, Fe3c, and Fe7c3 Produced by Co2-Laser Pyrolysis. *Journal of Materials Research* **1993,** 8, (7), 1666-1674.

53. Shi, X.; Sun, K.; Balogh, L. P.; Baker, J. R., Jr., Synthesis, characterization, and manipulation of dendrimer-stabilized iron sulfide nanoparticles. *Nanotechnology* **2006,** 17, (18), 4554-4560.

54. Douglas, T.; Young, M., Host-guest encapsulation of materials by assembled virus protein cages. *Nature* **1998,** 393, (6681), 152-155.

55. Douglas, T.; Young, M., Viruses: Making friends with old foes. *Science* **2006,** 312, (5775), 873-875.

56. Uchida, M.; Kang, S.; Reichhardt, C.; Harlen, K.; Douglas, T., The ferritin superfamily: Supramolecular templates for materials synthesis. *Biochimica Et Biophysica Acta-General Subjects* **2010,** 1800, (8), 834-845.

57. Kang, S.; Lucon, J.; Varpness, Z. B.; Liepold, L.; Uchida, M.; Willits, D.; Young, M.; Douglas, T., Monitoring biomimetic platinum nanocluster formation using mass spectrometry and cluster-dependent H_2 production. *Angewandte Chemie-International Edition* **2008,** 47, (41), 7845-7848.

58. Devey, A. J.; Grau-Crespo, R.; de Leeuw, N. H., Electronic and magnetic structure of Fe_3S_4: GGA+U investigation. *Physical Review B* **2009,** 79, (19).

59. Jolley, C. C.; Uchida, M.; Reichhardt, C.; Harrington, R.; Kang, S.; Klem, M. T.; Parise, J. B.; Douglas, T., Size and Crystallinity in Protein-Templated Inorganic Nanoparticles. *Chemistry of Materials* **2010,** 22, (16), 4612-4618.

60. Okuda, M.; Suzumoto, Y.; Iwahori, K.; Kang, S.; Uchida, M.; Douglas, T.; Yamashita, I., Bio-templated CdSe nanoparticle synthesis in a cage shaped protein, Listeria-Dps, and their two dimensional ordered array self-assembly. *Chemical Communications* **2010,** 46, (46), 8797-8799.

61. Uchida, M.; Klem, M. T.; Allen, M.; Suci, P.; Flenniken, M.; Gillitzer, E.; Varpness, Z.; Liepold, L. O.; Young, M.; Douglas, T., Biological containers: Protein cages as multifunctional nanoplatforms. *Advanced Materials* **2007,** 19, (8), 1025-1042.

62. Murphy, R.; Strongin, D. R., Surface reactivity of pyrite and related sulfides. *Surface Science Reports* **2009,** 64, (1), 1-45.

63. Andersson, K.; Nyberg, M.; Ogasawara, H.; Nordlund, D.; Kendelewicz, T.; Doyle, C. S.; Brown, G. E.; Pettersson, L. G. M.; Nilsson, A., Experimental and theoretical characterization of the structure of defects at the pyrite FeS_2(100) surface. *Physical Review B* **2004,** 70, (19).

64. Guevremont, J. M.; Strongin, D. R.; Schoonen, M. A. A., Thermal chemistry of H_2S and H_2O on the (100) plane of pyrite: Unique reactivity of defect sites. *American Mineralogist* **1998,** 83, (11-12), 1246-1255.

65. Nesbitt, H. W.; Bancroft, G. M.; Pratt, A. R.; Scaini, M. J., Sulfur and iron surface states on fractured pyrite surfaces. *American Mineralogist* **1998,** 83, (9-10), 1067-1076.

66. Teo, B. K., *EXAFS: Basic Principles and Data Analysis*. Springer-Verlag: Berlin, 1986.

67. Koningsberger, D. C. P., R., *X-Ray Absorption: Principles, Applications, Techniques of EXAFS, SEXAFS, and XANES*. Wiley: New York, 1988.

68. Hedman, B.; Hodgson, K. O.; Solomon, E. I., X-Ray Absorption-edge Spectroscopy of Ligands Bound to Open-shell Metal-ions - Chlorine K-edge Studies of Covalency in $[CuCl4]^{2+}$. *Journal of the American Chemical Society* **1990,** 112, (4), 1643-1645.

69. Solomon, E. I.; Hedman, B.; Hodgson, K. O.; Dey, A.; Szilagyi, R. K., Ligand K-edge X-ray absorption spectroscopy: covalency of ligand-metal bonds. *Coordination Chemistry Reviews* **2005,** 249, (1-2), 97-129.

70. Stöhr, J., Principles, Techniques, and Instrumentation of NEXAFS. In *NEXAFS Spectroscopy*, Springer-Verlag: Berlin, 1992; pp Chapter 5, p. 118-133.

71. de Groot, F., High resolution X-ray emission and X-ray absorption spectroscopy. *Chemical Reviews* **2001,** 101, (6), 1779-1808.

72. de Groot, F., Multiplet effects in X-ray spectroscopy. *Coordination Chemistry Reviews* **2005,** 249, (1-2), 31-63.

73. Hocking, R. K.; Wasinger, E. C.; de Groot, F. M. F.; Hodgson, K. O.; Hedman, B.; Solomon, E. I., Fe L-edge XAS studies of $K_4[Fe(CN)_6]$ and $K_3[Fe(CN)_6]$: A direct probe of back-bonding. *Journal of the American Chemical Society* **2006,** 128, (32), 10442-10451.

74. Wasinger, E. C.; de Groot, F. M. F.; Hedman, B.; Hodgson, K. O.; Solomon, E. I., L-edge X-ray absorption spectroscopy of non-heme iron sites: Experimental determination of differential orbital covalency. *Journal of the American Chemical Society* **2003,** 125, (42), 12894-12906.

75. Rehr, J. J.; Albers, R. C., Theoretical approaches to x-ray absorption fine structure. *Reviews of Modern Physics* **2000,** 72, (3), 621-654.

76. Adams, M. W. W., The Structure and Mechanism of Iron-Hydrogenases. *Biochimica Et Biophysica Acta* **1990,** 1020, (2), 115-145.

77. Volbeda, A.; Charon, M. H.; Piras, C.; Hatchikian, E. C.; Frey, M.; Fontecillacamps, J. C., Crystal-Structure of the Nickel-Iron Hydrogenase from Desulfovibrio-Gigas. *Nature* **1995,** 373, (6515), 580-587.

78. Pandey, A. S.; Harris, T. V.; Giles, L. J.; Peters, J. W.; Szilagyi, R. K., Dithiomethylether as a ligand in the hydrogenase H-cluster. *Journal of the American Chemical Society* **2008,** 130, (13), 4533-4540.

79. Nicolet, Y.; de Lacey, A. L.; Vernede, X.; Fernandez, V. M.; Hatchikian, E. C.; Fontecilla-Camps, J. C., Crystallographic and FTIR spectroscopic evidence of changes in Fe coordination upon reduction of the active site of the Fe-only hydrogenase from *Desulfovibrio desulfuricans*. *Journal of the American Chemical Society* **2001,** 123, (8), 1596-1601.

80. Boeck, A.; King, P. W.; Blokesch, M.; Posewitz, M. C., Maturation of hydrogenases. In *Advances in Microbial Physiology, Vol 51*, 2006; Vol. 51, pp 1-71.

81. Posewitz, M. C.; King, P. W.; Smolinski, S. L.; Zhang, L. P.; Seibert, M.; Ghirardi, M. L., Discovery of two novel radical S-adenosylmethionine proteins required for the assembly of an active [Fe] hydrogenase. *Journal of Biological Chemistry* **2004,** 279, (24), 25711-25720.

82. King, P. W.; Posewitz, M. C.; Ghirardi, M. L.; Seibert, M., Functional studies of [FeFe] hydrogenase maturation in an Escherichia coli biosynthetic system. *Journal of Bacteriology* **2006,** 188, (6), 2163-2172.

83. Rubach, J. K.; Brazzolotto, X.; Gaillard, J.; Fontecave, M., Biochemical characterization of the HydE and HydG iron-only hydrogenase maturation enzymes from Thermatoga maritima. *Febs Letters* **2005,** 579, (22), 5055-5060.

84. Brazzolotto, X.; Rubach, J. K.; Gaillard, J.; Gambarelli, S.; Atta, M.; Fontecave, M., The [Fe-Fe]-hydrogenase maturation protein HydF from Thermotoga maritima is a GTPase with an iron-sulfur cluster. *Journal of Biological Chemistry* **2006,** 281, (2), 769-774.

85. McGlynn, S. E.; Ruebush, S. S.; Naumov, A.; Nagy, L. E.; Dubini, A.; King, P. W.; Broderick, J. B.; Posewitz, M. C.; Peters, J. W., In vitro activation of [FeFe] hydrogenase: new insights into hydrogenase maturation. *Journal of Biological Inorganic Chemistry* **2007,** 12, (4), 443-447.

86. McGlynn, S. E.; Shepard, E. M.; Winslow, M. A.; Naumov, A. V.; Duschene, K. S.; Posewitz, M. C.; Broderick, W. E.; Broderick, J. B.; Peters, J. W., HydF as a scaffold protein in [FeFe] hydrogenase H-cluster biosynthesis. *Febs Letters* **2008,** 582, (15), 2183-2187.

87. Fish, W. W., Rapid Colorimetric Micromethod for the Quantitation of Complexed Iron in Biological Samples. *Methods in Enzymology* **1988,** 158, 357-364.

88. Happe, T.; Kaminski, A., Differential regulation of the Fe-hydrogenase during anaerobic adaptation in the green alga Chlamydomonas reinhardtii. *European Journal of Biochemistry* **2002,** 269, (3), 1022-1032.

89. Winkler, M.; Heil, B.; Heil, B.; Happe, T., Isolation and molecular characterization of the [Fe]-hydrogenase from the unicellular green alga Chlorella fusca. *Biochimica Et Biophysica Acta-Gene Structure and Expression* **2002,** 1576, (3), 330-334.

90. Johnson, M. K., Iron-sulfur Proteins. In *Encyclopedia of inorganic chemistry*, King, R. B., Ed. John Wiley & Sons Ltd.: West Sussex, England, 1994; pp 1896-1914.

91. Middleton, P.; Dickson, D. P. E.; Johnson, C. E.; Rush, J. D., Interpretation of the Mössbauer spectra of the four-iron ferredoxin from *Bacillus stearothermophilus*. *Eur. J. Biochem.* **1978,** 88, (1), 135-41.

92. Pereira, A. S.; Tavares, P.; Moura, I.; Moura, J. J. G.; Huynh, B. H., Mössbauer characterization of the iron-sulfur clusters in Desulfovibrio vulgaris hydrogenase. *Journal of the American Chemical Society* **2001,** 123, (12), 2771-2782.

93. Mulder, D. W.; Ortillo, D. O.; Gardenghi, D. J.; Naumov, A. V.; Ruebush, S. S.; Szilagyi, R. K.; Huynh, B.; Broderick, J. B.; Peters, J. W., Activation of HydA(Delta EFG) Requires a Preformed [4Fe-4S] Cluster. *Biochemistry* **2009,** 48, (26), 6240-6248.

94. Ravel, B.; Newville, M., ATHENA, ARTEMIS, HEPHAESTUS: data analysis for X-ray absorption spectroscopy using IFEFFIT. *Journal of Synchrotron Radiation* **2005,** 12, 537-541.

95. Newville, M., IFEFFIT: interactive XAFS analysis and FEFF fitting. *J Synchrotron Radiat* **2001,** 8, 322-324.

96. Newville, M.; Livins, P.; Yacoby, Y.; Rehr, J.; Stern, E., Near-edge X-ray-absorption fine structure of Pb: A comparison of theory and experiment. *Phys Rev B* **1993,** 47, (21), 14126-14131.

97. Ankudinov, A.; Ravel, B.; Rehr, J.; Conradson, S., Real-space multiple-scattering calculation and interpretation of x-ray-absorption near-edge structure. *Phys Rev B* **1998,** 58, (12), 7565-7576.

98. Ankudinov, A. L.; Nesvizhskii, A. I.; Rehr, J. J., Dynamic screening effects in x-ray absorption spectra. *Physical Review B* **2003,** 67, (11).

99. Berg, J. M.; Hodgson, K. O.; Holm, R. H., Crystal-Structure of $[(C_2H_5)_4N]_3[Fe_4S_4(SCH_2Ph)_4]$, a Reduced Ferredoxin Site Analog with a Nontetragonal Fe4S4 Core Structure in the Solid-State. *Journal of the American Chemical Society* **1979,** 101, (16), 4586-4593.

100. Barclay, J. E.; Davies, S. C.; Evans, D. J.; Hughes, D. L.; Longhurst, S., Lattice effects in the Mossbauer spectra of salts of $[Fe_4S_4\{S(CH_2)_nOHI\}_4]^{2-}$. Crystal structures of $[PPh_4]_2[Fe_4S_4\{S(CH_2)_nOH\}_4]$ (n=2, 3 and 4). *Inorganica Chimica Acta* **1999,** 291, (1-2), 101-108.

101. Beinert, H.; Emptage, M. H.; Dreyer, J. L.; Scott, R. A.; Hahn, J. E.; Hodgson, K. O.; Thomson, A. J., Iron-Sulfur Stoichiometry and Structure of Iron-Sulfur Clusters in 3-Iron Proteins - Evidence for [3Fe-4S] Clusters. *Proceedings of the National Academy of Sciences of the United States of America-Biological Sciences* **1983,** 80, (2), 393-396.

102. Musgrave, K.; Angove, H.; Burgess, B.; Hedman, B.; Hodgson, K. O., All-ferrous titanium(III) citrate reduced Fe protein of nitrogenase: An XAS study of electronic and metrical structure. *J Am Chem Soc* **1998,** 120, (21), 5325-5326.

103. Teo, B. K.; Shulman, R. G.; Brown, G. S.; Meixner, A. E., Exafs Studies of Proteins and Model Compounds Containing Dimeric and Tetrameric Iron-Sulfur Clusters. *Journal of the American Chemical Society* **1979,** 101, (19), 5624-5631.

104. Sofia, H. J.; Chen, G.; Hetzler, B. G.; Reyes-Spindola, J. F.; Miller, N. E., Radical SAM, a novel protein superfamily linking unresolved steps in familiar biosynthetic pathways with radical mechanisms: functional characterization using new analysis and information visualization methods. *Nucleic Acids Res.* **2001,** 29, (5), 1097-1106.

105. Shepard, E. M.; Broderick, J. B., S-Adenosylmethionine and iron-sulfur clusters in biological radical reactions: The radical SAM superfamily. In *Comprehensive Natural Products II: Chemistry and Biochemistry*, Mander, L. N.; Liu, H. W., Eds. Elsevier Press: Oxford U.K., 2010; Vol. 8, pp 625-662.

106. Walsby, C. J.; Hong, W.; Broderick, W. E.; Cheek, J.; Ortillo, D.; Broderick, J. B.; Hoffman, B. M., Electron-nuclear double resonance spectroscopic evidence that S-adenosylmethionine binds in contact with the catalytically active $[4Fe\text{-}4S]^{+}$ cluster of pyruvate formate-lyase activating enzyme. *J. Am. Chem. Soc.* **2002,** 124, (12), 3143-3151.

107. Walsby, C. J.; Ortillo, D.; Broderick, W. E.; Broderick, J. B.; Hoffman, B. M., An anchoring role for FeS Clusters: Chelation of the amino acid moiety of S-adenosylmethionine to the unique iron site of the [4Fe-4S] cluster of pyruvate formate-lyase activating enzyme. *J. Am. Chem. Soc.* **2002,** 124, (38), 11270-11271.

108. Walsby, C. J.; Ortillo, D.; Yang, J.; Nnyepi, M.; Broderick, W. E.; Hoffman, B. M.; Broderick, J. B., Spectroscopic approaches to elucidating novel iron-sulfur chemistry in the "Radical SAM" protein superfamily. *Inorg. Chem.* **2005,** 44, (4), 727-741.

109. Layer, G.; Moser, J.; Heinz, D. W.; Jahn, D.; Schubert, W.-D., Crystal structure of coproporphyrinogen III oxidase reveals cofactor geometry of Radical SAM enzymes. *EMBO Journal* **2003,** 22, (23), 6214-6224.

110. Chen, D.; Walsby, C.; Hoffman, B. M.; Frey, P. A., Coordination and mechanism of reversible cleavage of S-adenosylmethionine by the [4Fe-4S] center in lysine 2,3-aminomutase. *J. Am. Chem. Soc.* **2003,** 125, 11788-11789.

111. Hänzelmann, P.; Schindelin, H., Crystal structure of the S-adenosylmethionine-dependent enzyme MoaA and its implications for molybdenum cofactor deficiency in humans. *Proc. Natl. Acad. Sci. U.S.A.* **2004,** 101, (35), 12870-12875.

112. Hänzelmann, P.; Schindelin, H., Binding of 5'-GTP to the C-terminal FeS cluster of the radical S-adenosylmethionine enzyme MoaA provides insights into its mechanism. *Proc. Natl. Acad. Sci. U.S.A.* **2006,** 103, (18), 6829-6834.

113. Lepore, B. W.; Ruzicka, F. J.; Frey, P. A.; Ringe, D., The x-ray crystal structure of lysine-2,3-aminomutase from Clostridium subterminale. *Proc. Natl. Acad. Sci. U.S.A.* **2005,** 102, (39), 13819-13824.

114. Nicolet, Y.; Rubach, J. K.; Posewitz, M. C.; Amara, P.; Mathevon, C.; Atta, M.; Fontecave, M.; Fontecilla-Camps, J. C., X-ray structure of the [FeFe]-hydrogenase maturase HydE from *Thermotoga maritima*. *J. Biol. Chem.* **2008,** 283, (27), 18861-72.

115. Vey, J. L.; Yang, J.; Li, M.; Broderick, W. E.; Broderick, J. B.; Drennan, C. L., Structural basis for glycyl radical formation by pyruvate formate-lyase activating enzyme. *Proc. Natl. Acad. Sci. U.S.A.* **2008,** 105, (42), 16137-16141.

116. Henshaw, T. F.; Cheek, J.; Broderick, J. B., The $[4Fe\text{-}4S]^{+}$ cluster of pyruvate formate-lyase activating enzyme generates the glycyl radical on pyruvate formate-lyase: EPR-detected single turnover. *J. Am. Chem. Soc.* **2000,** 122, 8331-8332.

117. Nicolet, Y.; Amara, P.; Mouesca, J.-M.; Fontecilla-Camps, J. C., Unexpected electron transfer mechanism upon AdoMet cleavage in radical SAM proteins. *Proc. Natl. Acad. Sci. U.S.A.* **2009,** 106, (35), 14867-14871.

118. Rebeil, R.; Nicholson, W. L., The subunit structure and catalytic mechanism of the *Bacillus subtilis* DNA repair enzyme spore photoproduct lyase. *Proc. Natl. Acad. Sci. U.S.A.* **2001,** 98, (16), 9038-9043.

119. Munakata, N.; Rupert, C. S., Genetically controlled removal of "spore photoproduct" from deoxyribonucleic acid of ultraviolet-irradiated *Bacillus subtilis* spores. *J. Bacteriol.* **1972,** 111, 192-198.

120. Munakata, N.; Rupert, C. S., Dark repair of DNA containing "spore photoproduct" in *Bacillus subtilis*. *Mol. Gen. Genet.* **1974,** 130, 239-250.

121. Cheek, J.; Broderick, J. B., Direct H atom abstraction from spore photoproduct C-6 initiates DNA repair in the reaction catalyzed by spore photoproduct lyase: Evidence for a reversibly generated adenosyl radical intermediate. *J. Am. Chem. Soc.* **2002,** 124, (12), 2860-2861.

122. Varghese, A. J., 5-Thyminyl-5,6-dihydrothymine from DNA irradiated with ultraviolet light. *Biochem. Biophys. Res. Commun.* **1970,** 38, 484-490.

123. Donnellan, J. E., Jr.; Setlow, R. B., Thymine photoproducts but not thymine dimers found in ultraviolet-irradiated bacterial spores. *Science* **1965,** 149, 308-310.

124. Buis, J. M.; Cheek, J.; Kalliri, E.; Broderick, J. B., Characterization of an active spore photoproduct lyase, a DNA repair enzyme in the radical S-adenosylmethionine superfamily. *J. Biol. Chem.* **2006,** 281, (36), 25994-26003.

125. Mehl, R. A.; Begley, T. P., Mechanistic studies on the repair of a novel DNA photolesion: The spore photoproduct. *Org. Lett.* **1999,** 1, (7), 1065-1066.

126. Chandra, T.; Silver, S. C.; Zilinskas, E.; Shepard, E. M.; Broderick, W. E.; Broderick, J. B., Spore photoproduct lyase catalyzes specific repair of the 5*R* but not the 5*S* spore photoproduct *J. Am. Chem. Soc.* **2009,** 131, (7), 2420-2421.

127. Silver, S. C.; Chandra, T.; Zilinskas, E.; Ghose, S.; Broderick, W. E.; Broderick, J. B., Complete Stereospecific Repair of a Synthetic Dinucleotide Spore Photoproduct by Spore Photoproduct Lyase. *J. Biol. Inorg. Chem.* **2010,** 15, (6), 943-955.

128. Mantel, C.; Chandor, A.; Gasparutto, D.; Douki, T.; Atta, M.; Fontecave, M.; Bayle, P.-A.; Mouesca, J.-M.; Bardet, M., Combined NMR and DFT studies for the absolute configuration elucidation of the spore photoproduct, a UV-induced DNA lesion. *J. Am. Chem. Soc.* **2008,** 130, (50), 16978-16984.

129. Friedel, M. G.; Berteau, O.; Pieck, J. C.; Atta, M.; Ollagnier-de-Choudens, S.; Fontecave, M.; Carell, T., The spore photoproduct lyase repairs the 5S- and not the 5R-configured spore photoproduct DNA lesion. *Chem. Commun.*. **2006**, 445-447.

130. Chandor, A.; Berteau, O.; Douki, T.; Gasparutto, D.; Sanakis, Y.; Ollagnier-de-Choudens, S.; Atta, M.; Fontecave, M., Dinucleotide spore photoproduct, a minimal substrate of the DNA repair spore photoproduct lyase enzyme from Bacillus subtilis. *J. Biol. Chem.* **2006,** 281, (37), 26922-26931.

131. Chandor, A.; Douki, T.; Gasparutto, D.; Gambarelli, S.; Sanakis, Y.; Nicolet, Y.; Ollagnier-de-Choudens, S.; Atta, M.; Fontecave, M., Characterization of the DNA repair spore photoproduct lyase enzyme from Clostridium acetobutylicum: A radical-SAM enzyme. *C. R. Chimie* **2007,** 10, 756-765.

132. Broderick, J. B.; Henshaw, T. F.; Cheek, J.; Wojtuszewski, K.; Smith, S. R.; Trojan, M. R.; McGhan, R. M.; Kopf, A.; Kibbey, M.; Broderick, W. E., Pyruvate formate-lyase activating enzyme: strictly anaerobic isolation yields active enzyme containing a $[3Fe\text{-}4S]^{+}$ cluster. *Biochem. Biophys. Res. Comm.* **2000,** 269, 451-456.

133. Miller, J. R.; Busby, R. W.; Jordan, S. W.; Cheek, J.; Henshaw, T. F.; Ashley, G. W.; Broderick, J. B.; Cronan, J. E., Jr.; Marletta, M. A., *Escherichia coli*LipA is a Lipoyl Synthase: *In vitro* Biosynthesis of Lipoylated Pyruvate Dehydrogenase Complex from Octanoyl-Acyl Carrier Protein. *Biochemistry* **2000,** 39, 15166-15178.

134. Ugulava, N. B.; Sacanell, C. J.; Jarrett, J. T., Spectroscopic changes during a single turnover of biotin synthase: Destruction of a [2Fe-2S] cluster accompanies sulfur insertion. *Biochemistry* **2001,** 40, (28), 8352-8358.

135. Huynh, B. H.; Kent, T. A., Mössbauer studies of iron proteins. In *Advances in Inorganic Biochemistry*, Eichhorn, G. L.; Marzilli, L. G., Eds. Elsevier Scientific 1984; Vol. 6, pp 164-223.

136. Gardenghi, D.; Szilagyi, R. K. *Automated Data Reduction Protocol - an Excel-based Data Normalization Program*, Available at http://computational.chemistry.montana.edu/ADRP; Montana State University: Bozeman, MT, 2011.

137. Newville, M.; Ravel, B.; Haskel, D.; Rehr, J. J.; Stern, E. A.; Yacoby, Y., Analysis of multiple-scattering XAFS data using theoretical standards. *Physica B: Condensed Matter* **1995,** 208, (1-4), 154-156.

138. Szilagyi, R. K.; Winslow, M. A., On the accuracy of density functional theory for iron-sulfur clusters. *J. Comput. Chem.* **2006,** 27, 1385-1397.

139. Becke, A. D., Density-functional exchange-energy approximation with correct asymptotic behavior. *Phys. Rev. A* **1988,** 38, (6), 3098 - 3100.

140. Perdew, J. P., Density-functional approximation for the correlation-energy of the inhomogeneous electron-gas. *Phys. Rev. B* **1986,** 33, (12), 8822-8824.

141. Schaefer, A.; Huber, C.; Ahlrichs, R., Fully optimized contracted Gaussian basis sets of triple zeta valence quality for atoms Li to Kr. *Chem. Phys.* **1994,** 100, (8), 5829-5835.

142. Tomasi, J.; Persico, M., Molecular interactions in solution: An overview of methods based on continuous distributions of the solvent. *Chem. Rev.* **1994,** 94, (7), 2027-2094.

143. Cossi, M.; Barone, V.; Cammi, R.; Tomasi, J., Ab initio study of solvated molecules: a new implementation of the polarizable continuum model. *Chem. Phys. Lett.* **1996,** 255, (4-6), 327-335.

144. Barone, V.; Cossi, M.; Tomasi, J., A new definition of cavities for the computation of solvation free energies by the polarizable continuum model. *J. Chem. Phys.* **1997,** 107, (8), 3210-3221.

145. Westre, T. E.; Kennepohl, P.; DeWitt, J. G.; Hedman, B.; Hodgson, K. O.; Solomon, E. I., A multiplet analysis of Fe K-edge 1s - 3d pre-edge features of iron complexes. *J. Am. Chem. Soc.* **1997,** 119, 6297-6314.

146. Shulman, R. G.; Yafet, Y.; Eisenberger, P.; Blumberg, W. E., Observations and interpretation of x-ray absorption edges in iron compounds and proteins. *Proc. Natl. Acad. Sci. U.S.A.* **1976,** 73, (5), 1384-1388.

147. Shadle, S.; Hedman, B.; Hodgson, K. O.; Solomon, E. I., Ligand K-edge X-ray Absorption Spectroscopic Studies: Metal-Ligand Covalency in a Series of Transition Metal Tetrachlorides. *J Am Chem Soc* **1995,** 117, (8), 2259-2272.

148. Dey, A.; Glaser, T.; Couture, M. M.-J.; Eltis, L. D.; Holm, R. H.; Hedman, B.; Hodgson, K. O.; Solomon, E. I., Ligand K-edge X-ray absorption spectroscopy of $[Fe_4S_4]^{1+,2+,3+}$ clusters: Changes in bonding and electronic relaxation upon redox. *J. Am. Chem. Soc.* **2004,** 126, 8320-8328.

149. Glaser, T.; Hedman, B.; Hodgson, K. O.; Solomon, E. I., Ligand K-edge X-ray absorption spectroscopy: A direct probe of ligand-metal covalency. *Acc. Chem. Res.* **2000,** 33, 859-868.

150. Zhang, L.; Kong, Y.; Wu, D.; Zhang, H.; Wu, J.; Chen, J.; Ding, J.; Hu, L.; Jiang, H.; Shen, X., Three flavonoids targeting the β-hydroxyacyl-acyl carrier protein dehydratase from *Helicobacter pylori*: Crystal structure characterization with enzymatic inhibition assay. *Protein Science* **2008,** 17, (11), 1971-1978.

151. Ugulava, N. B.; Gibney, B. R.; Jarrett, J. T., Iron-Sulfur Cluster Interconversions in Biotin Synthase: Dissociation and Reassociation of Iron during Conversion of [2Fe-2S] to [4Fe-4S] Clusters. *Biochemistry* **2000,** 39, 5206-5214.

152. Duin, E. C.; Lafferty, M. E.; Crouse, B. R.; Allen, R. M.; Sanyal, I.; Flint, D. H.; Johnson, M. K., [2Fe-2S] to [4Fe-4S] cluster conversion in *Escherichia coli* biotin synthase. *Biochemistry* **1997,** 36, 11811-11820.

153. Tse Sum Bui, B.; Florentin, D.; Marquet, A.; Benda, R.; Trautwein, A. X., Mössbauer studies of *Escherichia coli* biotin synthase: evidence for reversible interconversion between $[2Fe\text{-}2S]^{2+}$ and $[4Fe\text{-}4S]^{2+}$ clusters. *FEBS Lett.* **1999,** 459, 411-414.

154. Busby, R. W.; Schelvis, J. P. M.; Yu, D. S.; Babcock, G. T.; Marletta, M. A., Lipoic Acid Biosynthesis: LipA is an iron-sulfur protein. *J. Am. Chem. Soc.* **1999,** 121, 4706-4707.

155. Ollagnier-de Choudens, S.; Fontecave, M., The lipoate synthase from *Escherichia coli* is an iron-sulfur protein. *FEBS Lett.* **1999,** 453, 25-28.

156. Lieder, K.; Booker, S.; Ruzicka, F. J.; Beinert, H.; Reed, G. H.; Frey, P. A., *S*-Adenosylmethionine-dependent reduction of lysine 2,3-aminomutase and observation of the catalytically functional iron-sulfur centers by electron paramagnetic resonance. *Biochemistry* **1998,** 37, 2578-2585.

157. Petrovich, R. M.; Ruzicka, F. J.; Reed, G. H.; Frey, P. A., Characterization of iron-sulfur clusters in lysine 2,3-aminomutase by electron paramagnetic resonance spectroscopy. *Biochemistry* **1992,** 31, 10774-10781.

158. Broderick, J.; Duderstadt, R.; Fernandez, D.; Wojtuszewski, K.; Henshaw, T.; Johnson, M., Pyruvate formate-lyase activating enzyme is an iron-sulfur protein. *J. Am. Chem. Soc.* **1997,** 119, 7396-7397.

159. Krebs, C.; Broderick, W. E.; Henshaw, T. F.; Broderick, J. B.; Huynh, B. H., Coordination of adenosylmethionine to a unique iron site of the [4Fe-4S] of pyruvate formate-lyase activating enzyme: A Mössbauer spectroscopic study. *J. Am. Chem. Soc.* **2002,** 124, (6), 912-913.

160. Yang, J.; Naik, S. G.; Ortillo, D. O.; Garcia-Serres, R.; Li, M.; Broderick, W. E.; Huynh, B. H.; Broderick, J. B., The iron-sulfur cluster of pyruvate formate-lyase activating enzyme in whole cells: cluster interconversion and a valence-localized $[4Fe\text{-}4S]^{2+}$ state. *Biochemistry* **2009,** 48, (39), 9234-41.

161. Krebs, C.; Henshaw, T. F.; Cheek, J.; Huynh, B.-H.; Broderick, J. B., Conversion of 3Fe-4S to 4Fe-4S clusters in native pyruvate formate lyase activating enzyme: Mössbauer characterization and implications for mechanism. *J. Am. Chem. Soc.* **2000,** 122, 12497-12506.

162. Ollagnier, S.; Meier, C.; Mulliez, E.; Gaillard, J.; Schuenemann, V.; Trautwein, A.; Mattioli, T.; Lutz, M.; Fontecave, M., Assembly of 2Fe-2S and 4Fe-4S clusters in the anaerobic ribonucleotide reductase from *Escherichia coli*. *J. Am. Chem. Soc.* **1999,** 121, 6344-6350.

163. Cosper, M. M.; Jameson, G. N. L.; Davydov, R.; Eidsness, M. K.; Hoffman, B. M.; Huynh, B. H.; Johnson, M. K., The $[4Fe\text{-}4S]^{2+}$ cluster in reconstituted biotin synthase binds *S*-adenosyl-L-methionine. *J. Am. Chem. Soc.* **2002,** 124, (47), 14006-7.

164. Cosper, N. J.; Booker, S. J.; Ruzicka, F.; Frey, P. A.; Scott, R. A., Direct FeS Cluster Involvement in Generation of a Radical in Lysine 2,3 Aminomutase. *Biochemistry* **2000,** 39, 15668-15673.

165. Cosper, M. M.; Cosper, N. J.; Hong, W.; Shokes, J. E.; Broderick, W. E.; Broderick, J. B.; Johnson, M. K.; Scott, R. A., Structural studies of the interaction of *S*-adenosylmethionine with the [4Fe-4S] clusters in biotin synthase and pyruvate formate-lyase activating enzyme. *Protein Sci.* **2003,** 12, (7), 1573-7.

166. Lloyd, S. J.; Lauble, H.; Prasad, G. S.; Stout, C. D., The mechanism of aconitase: 1.8 A resolution crystal structure of the S642a:citrate complex. *Protein Sci.* **1999,** 8, (12), 2655-62.

167. Robbins, A. H.; Stout, C. D., Structure of activated aconitase: formation of the [4Fe-4S] cluster in the crystal. *Proc. Natl. Acad. Sci. U.S.A.* **1989,** 86, 3639-3643.

168. Yu, C.; Irudayaraj, J., Multiplex biosensor using gold nanorods. *Analytical Chemistry* **2007,** 79, (2), 572-579.

169. Huang, X.; El-Sayed, I. H.; Qian, W.; El-Sayed, M. A., Cancer cells assemble and align gold nanorods conjugated to antibodies to produce highly enhanced, sharp, and polarized surface Raman spectra: A potential cancer diagnostic marker. *Nano Letters* **2007,** 7, (6), 1591-1597.

170. Schrinner, M.; Ballauff, M.; Talmon, Y.; Kauffmann, Y.; Thun, J.; Moeller, M.; Breu, J., Single Nanocrystals of Platinum Prepared by Partial Dissolution of Au-Pt Nanoalloys. *Science* **2009,** 323, (5914), 617-620.

171. Stamenkovic, V. R.; Fowler, B.; Mun, B. S.; Wang, G.; Ross, P. N.; Lucas, C. A.; Markovic, N. M., Improved oxygen reduction activity on Pt3Ni(111) via increased surface site availability. *Science* **2007,** 315, (5811), 493-497.

172. Hosein, H. A.; Strongin, D. R.; Allen, M.; Douglas, T., Iron and Cobalt oxide and metallic nanoparticles prepared from ferritin. *Langmuir* **2004,** 20, (23), 10283-10287.

173. Jolley, C.; Pool, V.; Idzerda, Y.; Douglas, T., All in the Packaging: Structural and Electronic Effects of Nanoconfinement on Metal Oxide Nanoparticles. *Chemistry of Materials* **2011,** 23, (17), 3921-3929.

174. Klem, M. T.; Young, M.; Douglas, T., Biomimetic magnetic nanoparticles. *Materials Today* **2005,** 8, (9), 28-37.

175. Onufrienok, V. V., Metastable iron sulfides. *Inorganic Materials* **2005,** 41, (6), 650-653.

176. Stiller, A. H.; McCormick, B. J.; Russell, P.; Montano, P. A., Existence and Stability of a Simple Sulfide of Iron(III). *Journal of the American Chemical Society* **1978,** 100, (8), 2553-2554.

177. Ward, J. C., Structure and Properties of Some Iron Sulphides. *Reviews of Pure and Applied Chemistry* **1970,** 20, (DEC), 175-&.

178. Johnson, D. C.; Dean, D. R.; Smith, A. D.; Johnson, M. K., Structure, function, and formation of biological iron-sulfur clusters. *Annual Review of Biochemistry* **2005,** 74, 247-281.

179. Hoffman, B. M.; Dean, D. R.; Seefeldt, L. C., Climbing Nitrogenase: Toward a Mechanism of Enzymatic Nitrogen Fixation. *Accounts of Chemical Research* **2009,** 42, (5), 609-619.

180. Peters, J. W.; Szilagyi, R. K., Exploring new frontiers of nitrogenase structure and mechanism. *Current Opinion in Chemical Biology* **2006,** 10, (2), 101-108.

181. Burgess, B. K.; Lowe, D. J., Mechanism of molybdenum nitrogenase. *Chemical Reviews* **1996,** 96, (7), 2983-3011.

182. Nicolet, Y.; Cavazza, C.; Fontecilla-Camps, J. C., Fe-only hydrogenases: structure, function and evolution. *Journal of Inorganic Biochemistry* **2002,** 91, (1), 1-8.

183. Adams, M. W. W.; Stiefel, E. I., Organometallic iron: the key to biological hydrogen metabolism. *Current Opinion in Chemical Biology* **2000,** 4, (2), 214-220.

184. Peters, J. W., Structure and mechanism of iron-only hydrogenases. *Current Opinion in Structural Biology* **1999,** 9, (6), 670-676.

185. Lee, S. C.; Holm, R. H., The clusters of nitrogenase: Synthetic methodology in the construction of weak-field clusters. *Chemical Reviews* **2004,** 104, (2), 1135-1157.

186. Drennan, C. L.; Peters, J. W., Surprising cofactors in metalloenzymes. *Current Opinion in Structural Biology* **2003,** 13, (2), 220-226.

187. Rod, T. H.; Logadottir, A.; Norskov, J. K., Ammonia synthesis at low temperatures. *Journal of Chemical Physics* **2000,** 112, (12), 5343-5347.

188. Ghirardi, M. L.; Posewitz, M. C.; Maness, P. C.; Dubini, A.; Yu, J. P.; Seibert, M., Hydrogenases and hydrogen photoproduction in oxygenic photosynthetic organisms. *Annual Review of Plant Biology* **2007,** 58, 71-91.

189. Evans, D. J., Metal-sulfur chemistry relevant to modelling the active sites of some enzymes of environmental importance. *Journal of Chemical Research-S* **2001**, (8), 297-303.

190. Nitschke, W.; Russell, M. J., Hydrothermal Focusing of Chemical and Chemiosmotic Energy, Supported by Delivery of Catalytic Fe, Ni, Mo/W, Co, S and Se, Forced Life to Emerge. *Journal of Molecular Evolution* **2009,** 69, (5), 481-496.

191. Cody, G. D., Transition metal sulfides and the origins of metabolism. *Annual Review of Earth and Planetary Sciences* **2004,** 32, 569-599.

192. Huber, C.; Wachtershauser, G., Peptides by activation of amino acids with CO on (Ni,Fe)S surfaces: Implications for the origin of life. *Science* **1998,** 281, (5377), 670-672.

193. Bebie, J.; Schoonen, M. A. A., Pyrite and phosphate in anoxia and an origin-of-life hypothesis. *Earth and Planetary Science Letters* **1999,** 171, (1), 1-5.

194. Rieder, M.; Crelling, J. C.; Sustai, O.; Draabek, M.; Weiss, Z.; Klementovaa, M., Arsenic in iron disulfides in a brown coal from the North Bohemian Basin, Czech Republic. *International Journal of Coal Geology* **2007,** 71, (2-3), 115-121.

195. Nicolet, Y.; Lemon, B. J.; Fontecilla-Camps, J. C.; Peters, J. W., A novel FeS cluster in Fe-only hydrogenases. *Trends in Biochemical Sciences* **2000,** 25, (3), 138-143.

196. Brunsvold, A. L.; Zhang, J.; Upadhyaya, H. P.; Minton, T. K., Beam-Surface Scattering Studies of the Individual and Combined Effects of VUV Radiation and Hyperthermal O, O_2, or Ar on FEP Teflon Surfaces. *Acs Applied Materials & Interfaces* **2009,** 1, (1), 187-196.

197. Minton, T. K.; Giapis, K. P.; Moore, T., Inelastic scattering dynamics of hyperthermal fluorine atoms on a fluorinated silicon surface. *Journal of Physical Chemistry A* **1997,** 101, (36), 6549-6555.

198. Wu, B.; Zhang, J.; Minton, T. K.; McKendrick, K. G.; Slattery, J. M.; Yockel, S.; Schatz, G. C., Scattering Dynamics of Hyperthermal Oxygen Atoms on Ionic

Liquid Surfaces: [emim][NTf(2)] and [C(12)mim][NTf(2)]. *Journal of Physical Chemistry C* **2010,** 114, (9), 4015-4027.

199. George, G. N.; George, S. J.; Pickering, I. J. *EXAFSPAK: A Suite of Computer Programs for Analysis of X-ray Absorption Spectra*, Available at: http://ssrl.slac.stanford.edu/exafspak.html; Stanford Synchrotron Radiation Lightsource: Menlo Park, CA, 2000.

200. Webb, S. *Sam's Interface for XAS Package (SiPACK)*, Available at http://sixpack.sams-xrays.com/; Menlo Park, CA, 2010.

201. Pierik, A. J.; Hagen, W. R.; Redeker, J. S.; Wolbert, R. B. G.; Boersma, M.; Verhagen, M.; Grande, H. J.; Veeger, C.; Mutsaers, P. H. A.; Sands, R. H.; Dunham, W. R., Redox Properties of the Iron-Sulfur Clusters in Activated Fe-Hydrogenase from Desulfovibrio-Vulgaris (Hildenborough). *European Journal of Biochemistry* **1992,** 209, (1), 63-72.

202. Marais, D. J. D.; Nuth, J. A.; Allamandola, L. J.; Boss, A. P.; Farmer, J. D.; Hoehler, T. M.; Jakosky, B. M.; Meadows, V. S.; Pohorille, A.; Runnegar, B.; Spormann, A. M., The NASA Astrobiology Roadmap. *Astrobiology* **2008,** 8, (4), 715-730.

203. Evangelou, V. P.; Zhang, Y. L., A Review - Pyrite Oxidation Mechanisms and Acid-Mine Drainage Prevention. *Critical Reviews in Environmental Science and Technology* **1995,** 25, (2), 141-199.

204. Che, L.; Gardenghi, D. J.; Szilagyi, R. K.; Minton, T. K., Production of a Biomimetic $Fe^{(I)}$-S Phase on Pyrite by Atomic Hydrogen Beam Surface Reactive Scattering. *Langmuir* **2011,** 27, (11), 6814-6821.

205. Krause, M. O., Atomic Radiative and Radiationless Yields for K-Shells and L-Shells. *Journal of Physical and Chemical Reference Data* **1979,** 8, (2), 307-327.

206. Singireddy, S.; Gorden, A. D.; Smirnov, A.; Vance, M. A.; Schoonen, M. A.; Strongin, D. R., Reduction of Nitrite and Nitrate to Ammonium on Pyrite Origins of Life and Evolution of Biospheres. **2012**, *In Review*.

207. Delgado-Jaime, M. U.; Conrad, J. C.; Fogg, D. E.; Kennepohl, P., X-ray absorption methods for the determination of Ru-Cl bond covalency in olefin metathesis catalysts: On the normalization of chlorine K-edges in ruthenium complexes. *Inorganica Chimica Acta* **2006,** 359, (9), 3042-3047.

208. Bordiga, S.; Bonino, F.; Lillerud, K. P.; Lamberti, C., X-ray absorption spectroscopies: useful tools to understand metallorganic frameworks structure and reactivity. *Chemical Society Reviews* **2010,** 39, (12), 4885-4927.